

AERODYNAMIC OPTIMIZATION OF HORIZONTAL AXIS WIND TURBINE  
BLADES BY USING CST METHOD, BEM THEORY AND GENETIC  
ALGORITHM

A THESIS SUBMITTED TO  
THE GRADUATE SCHOOL OF NATURAL AND APPLIED SCIENCES  
OF  
MIDDLE EAST TECHNICAL UNIVERSITY

BY

KERİMAN OĞUZ

IN PARTIAL FULFILLMENT OF THE REQUIREMENTS  
FOR  
THE DEGREE OF MASTER OF SCIENCE  
IN  
AEROSPACE ENGINEERING

SEPTEMBER 2019



Approval of the thesis:

**AERODYNAMIC OPTIMIZATION OF HORIZONTAL AXIS WIND  
TURBINE BLADES BY USING CST METHOD, BEM THEORY AND  
GENETIC ALGORITHM**

submitted by **KERİMAN OĞUZ** in partial fulfillment of the requirements for the degree of **Master of Science in Aerospace Engineering Department, Middle East Technical University** by,

Prof. Dr. Halil Kalıpçılar  
Dean, Graduate School of **Natural and Applied Sciences**

\_\_\_\_\_

Prof. Dr. İsmail Hakkı Tuncer  
Head of Department, **Aerospace Engineering**

\_\_\_\_\_

Assoc. Prof. Dr. Nilay Sezer Uzol  
Supervisor, **Aerospace Engineering, METU**

\_\_\_\_\_

**Examining Committee Members:**

Assist. Prof. Dr. Mustafa Perçin  
Aerospace Engineering, METU

\_\_\_\_\_

Assoc. Prof. Dr. Nilay Sezer Uzol  
Aerospace Engineering, METU

\_\_\_\_\_

Assist. Prof. Dr. Munir Elfarra  
Aerospace Engineering, Ankara Yıldırım Beyazıt University

\_\_\_\_\_

Assist. Prof. Dr. Ozan Keysan  
Electrical and Electronics Engineering, METU

\_\_\_\_\_

Assist. Prof. Dr. Elif Oğuz  
Civil Engineering, METU

\_\_\_\_\_

Date: 13.09.2019

**I hereby declare that all information in this document has been obtained and presented in accordance with academic rules and ethical conduct. I also declare that, as required by these rules and conduct, I have fully cited and referenced all material and results that are not original to this work.**

Name, Surname: Keriman Oğuz

Signature:

## **ABSTRACT**

### **AERODYNAMIC OPTIMIZATION OF HORIZONTAL AXIS WIND TURBINE BLADES BY USING CST METHOD, BEM THEORY AND GENETIC ALGORITHM**

Oğuz, Keriman

Master of Science, Aerospace Engineering  
Supervisor: Assoc. Prof. Dr. Nilay Sezer Uzol

September 2019, 104 pages

In this thesis, an aerodynamic design and optimization study for rotor airfoils and blades of Horizontal Axis Wind Turbines (HAWTs) is performed by using different airfoil representations and genetic algorithm. Two airfoil representations, the Class-Shape Transformation (CST) method and the Parametric Section (PARSEC) method, are used for the airfoil geometry designs. Their aerodynamic data is obtained by a potential flow solver software, XFOIL. The Blade Element Momentum (BEM) theory is used to calculate the rotor power production. Genetic Algorithm (GA) is used to optimize the airfoils, chord length and twist angle along the blade span for maximum rotor power production objective. For selected rotors, the validation cases are performed. The design and optimization studies and the calculations of the aerodynamic performance characteristics are compared with the selected test wind turbine data available in the literature. By using the optimized airfoil profiles, new blades are designed, analyzed and their aerodynamic performance enhancements are examined.

Keywords: Class-Shape Transformation (CST), Parametric Section (PARSEC), Blade Element Momentum (BEM) Theory, Horizontal Axis Wind Turbine, Genetic Algorithm

## ÖZ

# **YATAY EKSENLİ RÜZGAR TÜRBİNİ KANATLARININ SINIF-ŞEKİL TRANSFORMASYONU METODU, PALA ELEMANI MOMENTUM TEORİSİ VE GENETİK ALGORİTMA KULLANILARAK AERODİNAMİK OPTİMİZASYONU**

Oğuz, Keriman  
Yüksek Lisans, Havacılık ve Uzay Mühendisliği  
Tez Danışmanı: Doç. Dr. Nilay Sezer Uzol

Eylül 2019, 104 sayfa

Bu tezde, yatay eksenli rüzgar türbini rotor kanat kesiti ve pala geometrilerinin aerodinamik tasarım ve optimizasyon çalışması farklı kanat kesiti gösterimleri ve genetik algoritma kullanılarak yapılmıştır. Kanat kesiti geometrisi tasarımında iki farklı kanat kesiti gösterimi, Sınıf-Şekil Transformasyonu (CST) metodu ve Parametrik Kesit (PARSEC) metodu, kullanılmıştır. Aerodinamik veriler, bir potansiyel akış çözücüsü olan XFOIL yazılımı ile elde edilmiştir. Rotor güç hesaplamaları için Pala Elemanı Momentum (BEM) teorisi kullanılmıştır. Genetik Algoritma (GA), rotor maksimum güç üretimi amacıyla, pala boyunca kanat kesitleri, veter uzunluğu ve burkulma açısı optimizasyonunda kullanılmıştır. Seçilen rotorlar için doğrulama çalışmaları yapılmıştır. Yapılan tasarım ve optimizasyon çalışmaları ve aerodinamik performans karakteristikleri hesaplamaları literatürdeki mevcut test rüzgar türbin verileri ile karşılaştırılmıştır. Optimize edilmiş kanat kesiti geometrilerini de kullanarak yeni rotor palaları tasarlanmış, analizleri yapılmış ve aerodinamik performans artırımları incelenmiştir.

Anahtar Kelimeler: Sınıf-Şekil Transformasyonu Metodu, Parametrik Kesit Metodu, Pala Elemanı Momentum Teorisi, Yatay Eksenli Rüzgar Türbini, Genetik Algoritma

O Bir'e doğru...

## **ACKNOWLEDGEMENTS**

Very special thanks to my husband, Özkan, for showing the courage to share life with me.

Very special thanks to my big family. This work is the result of your support.

Very special thanks to Dr. Nilay Sezer Uzol for being more than an advisor.

Thank you the all people who had been and will be contributed to any scientific study.

Thank you the ones who strive for self-awareness and self-realization.

Thank you the ones who stands for justice, equality, freedom, peace.

Thank you the ones who seek for truth at any cost.

Thank you the ones who serve for the benefit of humanity.

Thank you the mother nature that feeds, grows and protects us.

Thank you the unknown and undone that make us alive, curious and motivated.

## TABLE OF CONTENTS

ABSTRACT .....	v
ÖZ .....	vii
ACKNOWLEDGEMENTS .....	x
TABLE OF CONTENTS .....	xi
LIST OF TABLES .....	xiv
LIST OF FIGURES .....	xvi
LIST OF ABBREVIATIONS .....	xx
LIST OF SYMBOLS .....	xxi
1. INTRODUCTION .....	1
1.1. Literature Review .....	5
1.2. Objectives of the Present Work .....	9
1.3. The Scope of the Thesis .....	10
2. METHODOLOGY .....	13
2.1. Airfoil Basics .....	13
2.1.1. Overview .....	13
2.1.2. Airfoil Representation Methods .....	14
2.1.3. Class-Shape Transformation (CST) Method .....	17
2.1.3.1. Shape Function Definition .....	17
2.1.3.2. Class Function Definition .....	18
2.1.3.3. Shape Function Representation of an Airfoil .....	18
2.1.3.4. Shape Function Decomposition to Basis Functions .....	19
2.1.3.5. CST Airfoil Representation .....	19

2.1.4. Parametric Section (PARSEC) Method .....	21
2.2. Rotor Aerodynamics .....	24
2.2.1. Momentum Theory .....	24
2.2.1.1. One Dimensional Axial Momentum Theory .....	24
2.2.1.2. Glauert Optimum Rotor .....	28
2.2.2. Blade Element Theory .....	29
2.2.3. Blade Element Momentum (BEM) Theory .....	32
2.2.4. Modifications to BEM .....	33
2.2.4.1. Hub and Tip Losses .....	33
2.2.4.2. Highly Loaded Rotor Correction .....	35
2.2.5. Convergence Issues .....	36
2.3. Potential Flow Solver, XFOIL .....	41
2.4. Genetic Algorithm (GA) .....	42
3. AIRFOIL DESIGN .....	45
3.1. Validation Studies .....	45
3.1.1. CST Method Fitting Validation .....	45
3.1.1.1. Investigation of the CST Parameterization Order Effect .....	46
3.1.1.2. Investigation of CST Weighting Coefficients and Airfoil Geometry Relations .....	49
3.1.2. PARSEC Method Fitting Validation .....	53
3.2. Airfoil Optimization Studies .....	55
3.2.1. CST Optimization Results .....	56
3.2.1.1. S809 Airfoil Geometry Optimizations with CST Parameterization ..	57
3.2.1.2. Case I - Optimization of Thinner Baseline Airfoil with CST .....	59

3.2.1.3. Case II - Optimization of Thicker Baseline Airfoil with CST .....	64
3.2.2. PARSEC Optimization Results .....	67
3.2.2.1. S809 Airfoil Geometry Optimizations with PARSEC Parameterization .....	67
3.2.2.2. Case III - Optimization of Thinner Baseline Airfoil with PARSEC..	69
3.2.2.3. Case IV - Optimization of Thicker Baseline Airfoil with PARSEC..	73
3.3. Evaluations on Airfoil Optimization Results .....	76
4. BLADE DESIGN .....	79
4.1. Airfoil Aerodynamic Coefficients Calculation .....	79
4.2. BEM Analysis Validation .....	80
4.2.1. NREL Phase III Wind Turbine Validation .....	82
4.2.2. NREL Phase VI Wind Turbine Validation .....	85
4.3. Blade Optimization Studies .....	88
5. CONCLUSION.....	95
5.1. Concluding Remarks .....	95
5.2. Future Work .....	96
REFERENCES.....	99

## LIST OF TABLES

### TABLES

Table 2.1 PARSEC Parameter Definitions [54] .....	22
Table 3.1. CST Weighting Coefficients of RAE 2822 Airfoil Varying Leading Edge Nose Radius .....	50
Table 3.2. CST Weighting Coefficients of RAE 2822 Airfoil Varying Boattail Angle .....	51
Table 3.3. CST Weighting Coefficients of RAE 2822 Airfoil Varying Thickness Distribution .....	53
Table 3.4 PARSEC Geometric Coefficients for S809 Airfoil .....	54
Table 3.5 CST Weighing Coefficients for S809 Airfoil Baselines .....	57
Table 3.6. The Initial Genetic Algorithm Optimization Parameters for Case I.....	59
Table 3.7. The Revised Genetic Algorithm Optimization Parameters for Case I .....	60
Table 3.8. The Objective Function Results for Case I.....	62
Table 3.9. CST Weighing Coefficients for Thinner Optimized Baseline Airfoil.....	63
Table 3.10. The Genetic Algorithm Optimization Parameters for Case II .....	64
Table 3.11. The Objective Function Results for Case II .....	65
Table 3.12. CST Weighing Coefficients for Thicker Optimized Baseline Airfoil ....	67
Table 3.13 PARSEC Geometric Parameters for S809 Airfoil Baselines .....	68
Table 3.14. The Objective Function Results for Case III .....	71
Table 3.15. PARSEC Geometric Coefficients for Thinner Optimized Baseline Airfoil .....	73
Table 3.16. The Objective Function Results for Case IV .....	74
Table 3.17. PARSEC Geometric Coefficients for Thicker Optimized Baseline Airfoil .....	76

Table 3.18. Aerodynamic Performance Comparison of CST vs PARSEC Parameterized Airfoils – Thinner Baseline Results (upper) and Thicker Baseline Results (lower) .....	77
Table 4.1. The Rotor Geometric Parameters of the NREL Phase III and VI Rotors.	80
Table 4.2. Airfoil Distribution of Reference and Optimized Rotors.....	89
Table 4.3. Chord Length and Twist Angle Optimization Bounds .....	90
Table 4.4. The Genetic Algorithm Optimization Parameters for Blade Optimization .....	90
Table 4.5. Power Comparison for Airfoil, Chord and Twist Optimized Rotor .....	91

## LIST OF FIGURES

### FIGURES

Figure 1.1. Historical Development of LCOE of Wind Energy [40] .....	2
Figure 1.2. Historical Development of New Installations in GW [39].....	2
Figure 1.3. Historical Development of Total Installations in GW [39].....	3
Figure 1.4. Historical Development of Annual Installations in Turkey in MW [41] ..	3
Figure 1.5. Historical Development of Total Installations in Turkey in MW [41] .....	4
Figure 1.6. Flowchart of HAWT Rotor Design Methodology .....	10
Figure 2.1. Typical Airfoil Nomenclature [46] .....	14
Figure 2.2. Modern Airfoil Nomenclature [46] .....	14
Figure 2.3. PARSEC Geometric Airfoil Parameters [16].....	21
Figure 2.4. Actuator Disc Model with Pressure and Axial Velocity Diagrams [29].	25
Figure 2.5. A Circular Control Volume around a Wind Turbine [29].....	26
Figure 2.6. The Induced Velocities for Glauert Optimum Rotor [29].....	28
Figure 2.7. The Velocity Triangle of Blade Element [29].....	29
Figure 2.8. Lift and Drag Forces Acting on an Airfoil [29] .....	30
Figure 2.9. The Forces on Blade Element [29].....	30
Figure 2.10. The Vortex Sheet Formation behind the Wind Turbine Blade [51].....	34
Figure 2.11. Comparison of Different $C_T$ Values – Empirical, Glauert Correction and BEM Calculation without Any Correction Results [33].....	35
Figure 2.12. Solution Regions for Ning’s Method [22].....	39
Figure 2.13. BEM Algorithm with Ning’s Guaranteed Convergence Method.....	40
Figure 3.1. 5 <sup>th</sup> Order CST Fitting with AirfoilCST for RAE 2822 Airfoil.....	45
Figure 3.2. 5 <sup>th</sup> Order CST Fitting with AirfoilCST for S809 Airfoil .....	47
Figure 3.3. Upper and Lower Curve Residuals for 5 <sup>th</sup> Order AirfoilCST S809 Airfoil Fitting Results .....	47
Figure 3.4. 9 <sup>th</sup> Order CST Fitting with AirfoilCST for S809 Airfoil .....	48

Figure 3.5. Upper and Lower Curve Residuals for 9 <sup>th</sup> Order AirfoilCST S809 Airfoil Fitting Results .....	48
Figure 3.6. Leading Edge Nose Radius CST Term Effect on RAE 2822 Airfoil Geometry.....	50
Figure 3.7. Boattail Angle CST Term Effect on RAE 2822 Airfoil Geometry .....	51
Figure 3.8. Thickness Distribution CST Term Effect on RAE 2822 Airfoil Geometry .....	52
Figure 3.9. PARSEC Fitting with AirfoilPARSEC for S809 Airfoil.....	54
Figure 3.10. Upper and Lower Curve Residuals for AirfoilPARSEC S809 Airfoil Fitting Results .....	55
Figure 3.11. Airfoil Geometry Optimization Flowchart .....	56
Figure 3.12. The Comparison of Thinner and Thicker Baseline Airfoil Geometries Generated with CST Parameterization to S809 Profile.....	58
Figure 3.13. The Upper and Lower Bounds of Thinner (upper) and Thicker (lower) Optimization Baseline Geometries .....	59
Figure 3.14. The Fitness Value vs Generation Number Graph for Case I with Initial GA Optimization Parameters .....	60
Figure 3.15. The Best and Mean Fitness Values vs Generation Graph for Case I.....	61
Figure 3.16. The Average Distance between Individuals vs Generation Number Graph for Case I.....	61
Figure 3.17. The $C_l/C_d$ Ratio Comparisons for Case I.....	62
Figure 3.18. The Airfoil Geometry Comparisons for Case I .....	63
Figure 3.19. The Best and Mean Fitness Values vs Generation Graph for Case II ...	64
Figure 3.20. The Average Distance between Individuals vs Generation Number Graph for Case II.....	65
Figure 3.21. The $C_l/C_d$ Ratio Comparisons for Case II.....	66
Figure 3.22. The Airfoil Geometry Comparisons for Case II .....	66
Figure 3.23. The Comparison of Thinner and Thicker Baseline Airfoil Geometries Generated with PARSEC Parameterization to S809 Profile.....	68

Figure 3.24. The Upper and Lower Bounds of Thinner (upper) and Thicker (lower) Optimization Baseline Geometries .....	69
Figure 3.25. The Best and Mean Fitness Values vs Generation Graph for Case III .	70
Figure 3.26. The Average Distance between Individuals vs Generation Number Graph for Case III.....	71
Figure 3.27. The $C_l/C_d$ Ratio Comparisons for Case III.....	72
Figure 3.28. The Airfoil Geometry Comparisons for Case III .....	72
Figure 3.29. The Fitness Value vs Generation Number Graph for Case IV.....	73
Figure 3.30. The Average Distance between Individuals vs Generation Number Graph for Case IV.....	74
Figure 3.31. The $C_l/C_d$ Ratio Comparisons for Case IV.....	75
Figure 3.32. The Airfoil Geometry Comparisons for Case IV .....	75
Figure 4.1. $C_d$ vs AoA Graph for S809 Airfoil ( $Re=0.75 \times 10^6$ ).....	79
Figure 4.2. $C_l$ vs AoA Graph for S809 Airfoil ( $Re=0.75 \times 10^6$ ).....	80
Figure 4.3. Chord Length Distribution of NREL Phase III and NREL Phase VI Turbines .....	81
Figure 4.4. Twist Angle Distribution of NREL Phase III and NREL Phase VI Turbines .....	81
Figure 4.5. NREL Phase III Rotor Validation Case - Power Curve Results .....	82
Figure 4.6. NREL Phase III Rotor Validation Case - Thrust Curve Results .....	83
Figure 4.7. $F_{hub}$ vs Dimensionless Rotor Radius Graph.....	83
Figure 4.8. $F_{tip}$ vs Dimensionless Rotor Radius Graph.....	84
Figure 4.9. $F$ vs Dimensionless Rotor Radius Graph.....	84
Figure 4.10. NREL Phase VI Rotor Validation Case - Power Curve Results .....	85
Figure 4.11. NREL Phase VI Rotor Validation Case - Thrust Curve Results.....	86
Figure 4.12. $CT$ vs Axial Induction Factor Curves at Different Wind Speeds –.....	87
Figure 4.13. Airfoil Distribution Illustration for Optimized Rotor .....	89
Figure 4.14. The Best and Mean Fitness Values vs Generation Graph for Blade Optimization Study.....	91

Figure 4.15. Power Curve Comparison for Airfoil, Chord and Twist Optimized Rotor  
.....92

Figure 4.16. Chord Distribution of Airfoil, Chord and Twist Optimized Rotor.....92

Figure 4.17. Twist Distribution of Airfoil, Chord and Twist Optimized Rotor.....93

## LIST OF ABBREVIATIONS

AEP	Annual Energy Production
AoA	Angle of Attack
BEM	Blade Element Momentum
CAGR	Compound Annual Growth Rate
CFD	Computational Fluid Dynamics
CoE	Cost of Energy
CST	Class-Shape Transformation
DHDR	Declaration of Human Duties and Responsibilities
EAWA	The European Academy of Wind Energy
GA	Genetic Algorithm
GWEC	Global Wind Energy Council
HAWT	Horizontal Axis Wind Turbine
IEA	International Energy Agency
LCOE	Levelized Cost of Energy
LE	Leading Edge
NREL	National Renewable Energy Laboratory
NURBS	Non-Uniform Rational B-Spline
PARSEC	Parametric Sectioning
TE	Trailing Edge
TWEA	Turkish Wind Energy Association

## LIST OF SYMBOLS

$A = \pi R^2$	Actuator disk area
$AR$	Aspect ratio
$a$	Axial induction factor
$a'$	Tangential induction factor
$B$	Number of blades
$c$	Blade chord
$C_d$	Drag coefficient (sectional or local)
$C_l$	Lift coefficient (sectional or local)
$C_M$	Torque coefficient
$C_P$	Power coefficient
$C_r$	The radial component of the absolute velocity
$C_T$	Thrust coefficient
$C_\alpha$	The axial component of the absolute velocity
$C_\theta$	The azimuthal component of the absolute velocity
$D$	Drag force (2-D)
$F$	Total loss correction factor
$F_{hub}$	Hub loss correction factor
$F_{tip}$	Tip loss correction factor
$L$	Lift force (2-D)
$\dot{m}$	Mass flow rate

$M$	Torque
$Ma$	Mach number
$N$	Number of blade elements
$r$	Local blade radius
$R$	Rotor radius
$Re$	Reynold's number
$R_{hub}$	Rotor hub radius
$p$	Pressure
$P$	Power
$t$	Time
$T$	Thrust
$U$	Freestream velocity
$u$	x-component of the velocity vector
$v$	y-component of the velocity vector
$w$	z-component of the velocity vector
$V_{rel}$	Relative wind velocity
$W$	The total induced velocity
$\alpha$	Angle of attack
$\beta$	Twist of blade
$\varphi$	Flow angle
$\mu$	Dynamic viscosity

$\lambda$	Tip to speed ratio
$\lambda_r$	Local speed ratio
$\theta$	Local pitch angle
$\theta_p$	Pitch angle
$\sigma$	Solidity
$\rho$	Density
$\omega$	Rotor rotational speed



## CHAPTER 1

### INTRODUCTION

Native American proverb says that “We don't inherit the earth from our ancestors; we borrow it from our children.” Declaration of Human Duties and Responsibilities (DHDR) aka Valencia Declaration, adopted in 1998, is aimed to fortify the fulfillment of human rights [26]. It manifests our duties and responsibilities as human beings within the current century's intricate and interdependent lives. DHDR Chapter 2, Article 3 clearly states that the protection and survival of both present and future generations is our duty [26]. Therefore, it is undisputable that caring for The Earth and making it a sustainable home should be a top priority for both governments and individuals. Kyoto Protocol and Paris Climate Agreement, effective since 2005 and 2016 respectively, aim for their signatory countries to reduce greenhouse gas emissions as these gases, which are mostly excrements from fossil fuels for energy, are deadly harmful to our mother earth [27, 28]. Renewable technology appears as the best alternative to create maintainable and environmental friendly energy resources. Among different kinds, wind power is one the substantial renewable energy resource serving a wide range of needs from small scale, off-grid, one or two kilowatt domestic single turbine utilization to gigantic, off-shore, multi-gigawatt wind farms.

Global Wind Energy Council (GWEC) has distributed 14<sup>th</sup> annual global status report on wind energy in 2019 [39]. The study claims that wind has become one of the cheapest energy resources when Levelized Cost of Energy (LCOE) values are compared. In Figure 1.1, BloombergNEF data [40] of LCOE change of wind energy is given as taken place in GWEC report. It reveals that there has been a strong, gradual drop on LCOE levels both onshore and off-shore markets. Especially, offshore turbine costs are dramatically decreased enabling to flourish this previously niche market.

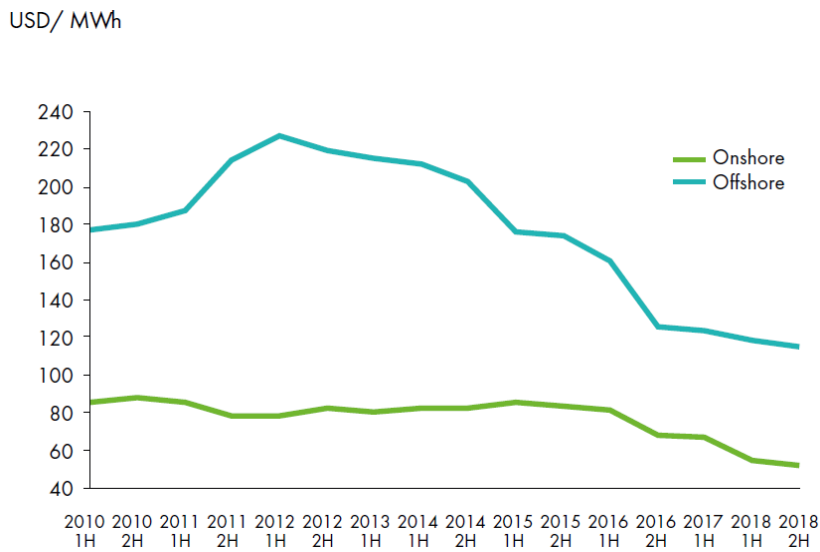


Figure 1.1. Historical Development of LCOE of Wind Energy [40]

The same report has been expected more than 55 GW total annual installations of wind power plants for both markets till 2023. As it can be clearly seen in Figure 1.2, over the last five years, annual new installations have managed to stay above 50 GW, increasing compound annual growth rate as 7%. Additionally, it stands out that in Figure 1.3, total installations of wind power plants reached nearly 5 times for the last decade.

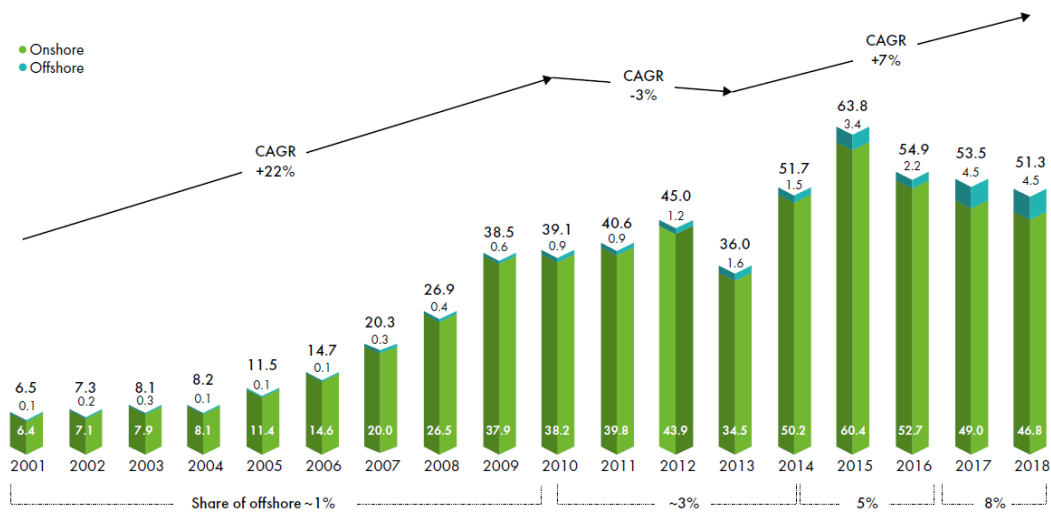


Figure 1.2. Historical Development of New Installations in GW [39]

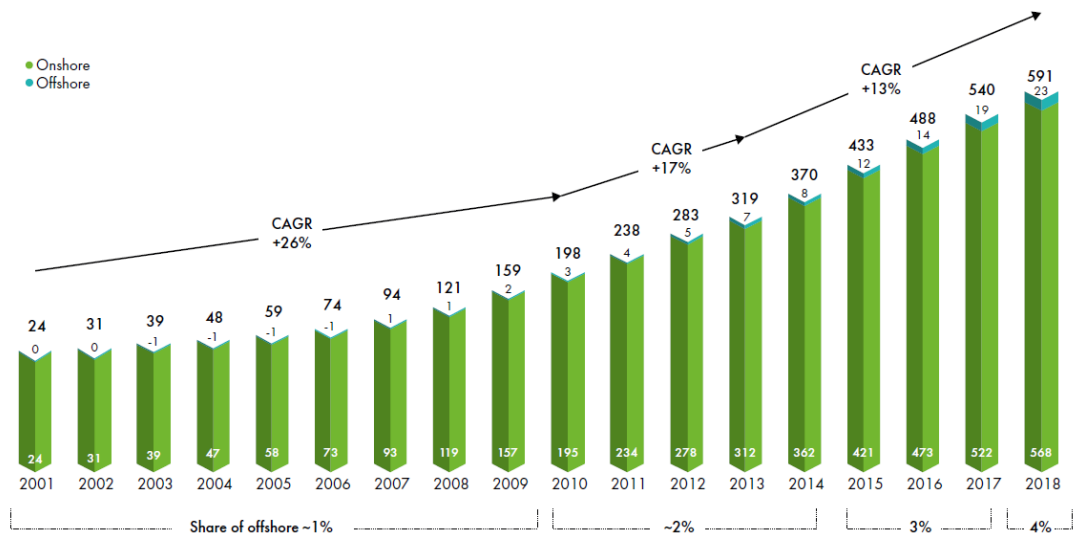


Figure 1.3. Historical Development of Total Installations in GW [39]

Turkish Wind Energy Association (TWEA) has published updated version of Turkish Wind Energy Statistics Report on January 2019 [41]. The share of wind energy in electric generation in Turkey is declared as 6.78% of annual average. In Figure 1.4 annual new installations in Turkey are given while total installation amounts are shown in Figure 1.5.

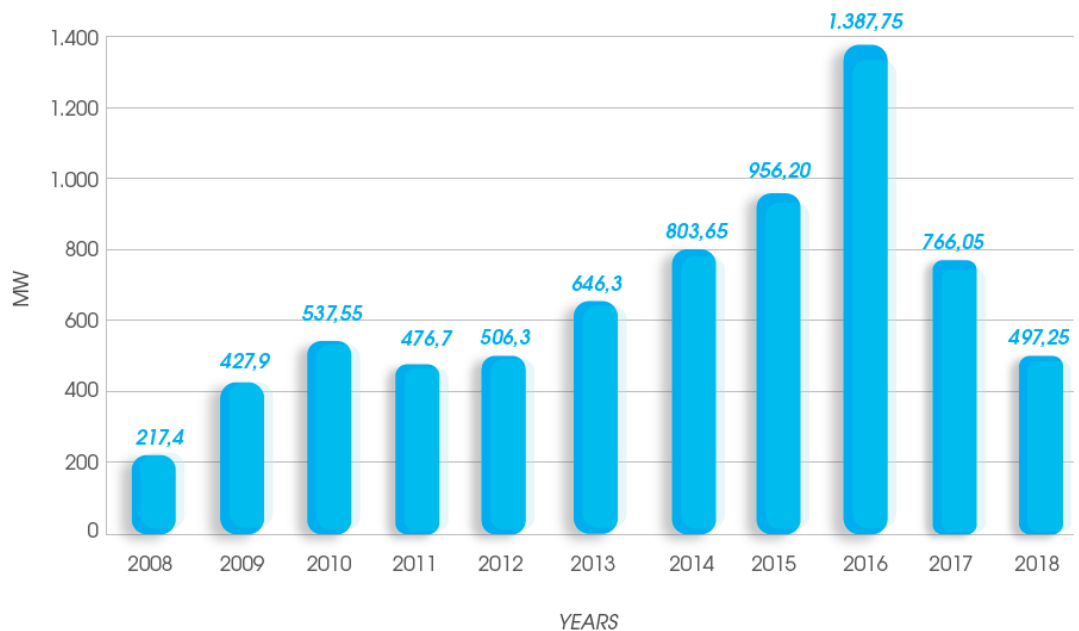


Figure 1.4. Historical Development of Annual Installations in Turkey in MW [41]

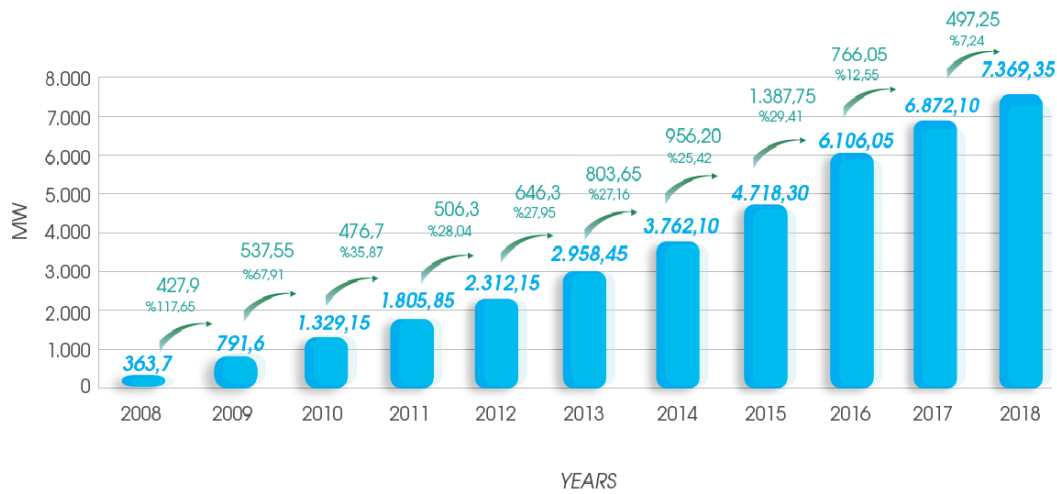


Figure 1.5. Historical Development of Total Installations in Turkey in MW [41]

This year, International Energy Agency (IEA) Wind Technology Collaboration Programme has published a technical report on “Grand Vision Wind Energy”, formed at the international wind energy technology workshop held in 2017 and portraying an optimistic prospective electricity system in which more than half of worldwide electricity production will be gathered from wind [38]. Reducing LCOE and increasing electricity distribution system value are two main objective scenarios to perform serious innovations to be able to achieve this “Grand Vision” goal. At the turbine technology and design section of the report, larger wind turbines, having higher capacity factor rotors and higher Re airfoils are some of the innovations suggested for decreasing LCOE scenario. At the same time, for improving grid system value objective, certain innovation fields are mentioned as again longer rotor blades with higher capacity factors and low wind speed turbines.

In the light of global market trends, technology roadmaps and aerodynamic research interests, the content of this study is shaped. In this thesis, it is aimed to develop a design tool for HAWT blades and an optimization tool airfoil sections. Class-Shape Transformation (CST) and Parametric Section (PARSEC) methods have selected as airfoil representation methods. Parameterized airfoil profiles have optimized by using GA. Then, HAWT blade designs are performed by utilizing BEM theory based aerodynamic design tool.

In this first introducing chapter, literature review is given in Section 1.1. Then the objective of the study is explained in Section 1.2. Finally, the scope of the thesis is pointed out in Section 1.3.

### **1.1. Literature Review**

According to “Grand Vision Wind Energy” report, 2019, nearly each turbine in market as well as the largest ones is developed on BEM method based aeroelastic tools despite the restrictions of the theory when modeling elevated deflections of highly flexible blades, floating turbine dynamics or 3D flow solutions near the hub region [38].

Van Kuik et al., from The European Academy of Wind Energy (EAWA), have been published a long-term research agenda about 11 basic research fields of wind energy in 2016 [37]. In aerodynamics section of this paper, it is stated that the validity of Blade Element Momentum (BEM) Theory is confirmed by Computational Fluid Dynamics (CFD) and experimental results whereas additional studies are continued on simplified, low fidelity models. For complicated wind turbine flow conditions, vortex lifting line and panel methods are being investigated, verified and described as supportives to developments of BEM method progressively. Moreover, the research have emphasized that due to the contamination, 3D blade aerodynamics is still insufficiently explored concerning roughness and turbulence effects on transition region and separation behaviors.

There are numerous considerable researches have conducted in METU about wind turbine blade design and optimization. Firstly, Ceyhan et al. [1, 2], 2008-2009, has developed a design and optimization tool for HAWT blades by using BEM and GA. The optimization objective is designated to harvest maximum power where the optimization variables are selected as airfoil sections, chord and twist distributions. Two different wind turbines, having 100 kW and 1 MW rated power, have optimized in these studies. Then, Sağol et al. [3,4], 2009-2010, has designed and optimized HAWT blades by utilizing BEM and GA, subject to minimum CoE objective for a site specific design consideration. Three different scenarios have studied to reduce CoE.

After that, Polat et al. [5-8], 2011-2013, has studied aerodynamic geometry optimization methodology for HAWT blades in order to get maximum power with BEM and GA by defining new airfoil profiles with Bezier curves at three different sections of the blade. Nordtank and Risø wind turbines are optimized by using this procedure. Moreover, Polat et al. [9], 2014, investigated design of HAWT blades and airfoils as well as helicopters' comparatively. Elfarra et al. [10-15], 2010-2015, has examined blade tip geometry, twist angle distribution and pitch angle optimization for a HAWT blade by using CFD, GA and artificial neural networks. NREL II and NREL VI turbines are selected as validation cases.

Ning [22], 2013, has builded up a solution to the convergence problem occurring when calculating axial and tangential factors at some blade regions. In this approach, BEM equations are parameterized by only a function of local inflow angle providing robust and efficient solution. The study offers a convenient residual function by reducing to problem from 2D fixed-point algorithm to 1D root finding algorithm ensuring guaranteed convergence. The solution algorithm divides the function into well behaved parts by bounding them into appropriate brackets. Then, the algorithm solves each part separately inside corresponding bounds.

When commercial applications of wind turbine blade optimization are searched, Engfer et al.'s study, 2015, on Alstom Wind Company comes forward. The purpose of the study is to introduce a blade design method having low CoE as optimization target with high annual energy production (AEP) considering both aerodynamic and structural performances. Design variables are determined as number of blade sections, sectional radius, chord distribution, twist distribution, relative thickness distribution, master airfoils (geometry and characteristics), mass and stiffness. In order to attain the target airfoil polar characteristics, new airfoil geometries are created and easily parameterized by Class-Shape Transformation (CST) Method. Bernstein polynomials and Bezier curves are used to represent different airfoil geometries and related Bernstein coefficients and Bezier control points become optimization parameters. Flatback airfoil geometries are utilized for their structural benefits. Airfoil

characteristics are obtained by RFOIL, a modified version of XFOIL considering rotational effects, which is coupled with evolutionary optimization solver. After master airfoils are defined, blade geometry is optimized by minimizing CoE function. Firstly, chord, twist and relative thickness distributions of blade are interpreted as a function of blade radius in the form of B-splines. After that, control point coordinates of B-splines are optimized. Cost function is composed of some target values such as power coefficient, optimum tip to speed ratio, AEP, tower loads and blade weight. In every optimization loop, these target values are computed by an aero-elastic code. Results have shown that this approach creates smooth blade surfaces automatically in a time efficient way by performing evolutionary and commonly used general algorithms.

Eke and Onyewudiala, 2010, have conducted a research on optimization wind turbine blades using GA. The optimization target is to minimize CoE which is the ratio of the rotor cost to AEP [24]. The design variables are the chord, the twist and the relative thickness distributions of the blade. BEM is used to determine power curve and Weibull distribution of wind is used to calculate AEP. 25 kW Mexico experimental rotor and Tjaereborg 2 MW Wind Turbine rotor are examined as case studies. In both cases, the results obtained after optimization are found coherent with existing studies and the cost of optimized rotor is successfully reduced.

Méndez and Greiner, 2009, have published a detailed paper in which they performed wind blade chord length and twist angle optimization using GA [25]. Optimization target is to maximize mean expected annual power, depending on the Weibull wind distribution at a specific site. Due to its low computational effort requirements, BEM is used for torque and power calculations. MATLAB genetic toolbox coupled with BEM code is used as the optimization solver. While airfoil geometry optimization is out of the scope of this research, same airfoil characteristics of the case study turbine blade are used as geometry related inputs. The allowable interval of both chord and twist distributions are also provided as inputs. For a specific site having certain wind distribution parameters, the Risø test turbine blades are chosen as optimization

application case. Unsurprisingly, the results have indicated that the optimized blade has relatively better performance.

A large number of existing studies in the broader literature have examined airfoil optimization. Okrent, 2017, has studied on optimization of airfoil geometry for a HALE type UAV with GA [42]. Airfoil design space is defined with three different independent parametric airfoil families, namely the NACA 4 series, CST family, and the PARSEC family. Aerodynamic performance evaluation is done with XFOIL. In order to maximize desired mission profile, a weighed objective function is defined using a combination of  $L/D$  and  $L^{3/2}/D$  ratios. Optimization for each airfoil family is performed in MATLAB. Optimized geometries from different airfoil families are compared and the airfoil generated from CST family is found to be best choice.

Mauclere, 2009, has performed airfoil design and optimization by using B-Splines representation [43]. XFOIL is used to obtain aerodynamic coefficients and algorithms have been implemented in MATLAB. Baseline airfoil is selected as MH43. For particular Ma and Re,  $L/D$  ratios are calculated for two different AoA values,  $2^\circ$  and  $5^\circ$  respectively. Furthermore, spar geometry and leading edge roughness effects are implemented in optimization objective function and results are discussed comparatively. Consequently, it is observed that optimized airfoil geometries have higher performance for specific design conditions.

Grasso, 2012, has conducted a very detailed research on a thick airfoil optimization methodology by using a combined GA and gradient based optimization algorithm [44]. Cubic Bezier representation is selected as parameterization method. RFOIL is used to calculate aerodynamic performance coefficients and DU00-W2-350 flatback airfoil is selected as baseline geometry. A weighed linear objective function is defined as a combination of aerodynamic performance ( $L/D$  ratio) and structural requirements (the sectional moment of resistance). For specific flow conditions, the optimization is done for free and in fixed transition conditions. It is found that the new designed airfoil family has better performance than the baseline geometry.

Van Bussel, 2012, has reviewed airfoil and blade design basics in wind energy [49]. It summarizes the airfoil design progress in a way that thicker airfoils having higher design  $l/d$  values and resettled stall behavior. At the same time, it is expected to have thicker blades with slender tips designed for lower induction factors in blade design studies.

Bortolotti et al., 2019, have published a detailed technical report on reference wind turbines expressing current wind turbine technology [45]. This study concentrates on two reference turbines; one is an onshore turbine operating on moderate wind sites and the latter is an off-shore latest technology wind turbine. First one has 3.4 MW rated power having oversized rotor diameter for high capacity factor where design wind regime is class III. Second reference turbine, designed for class I wind regimes, has 10 MW rated power. FFA-W3 the airfoil family is used in that rotor.

Liu et al., 2018, have focused on improvement on morbidity of high order CST parameterization and proposed the pivot element weighting iterative (PEWI) method that can enhance the ill-conditioned CST coefficient matrix [55]. By using PEWI method, the S1223 airfoil is parameterized and then optimized by using GA to obtain the maximum  $L/D$  ratio objective. It is observed that the optimum airfoil is highly cambered by comparison to the initial airfoil and the  $L/D$  ratio is increased by 2.3% whereas the  $C_d$  value is decreased by 1.4%.

## **1.2. Objectives of the Present Work**

The objectives of this study are listed as follows;

- Development of
  - CST airfoil fitting code, named as AirfoilCST, that can be fit for a known airfoil geometry with CST parameterization of any order
  - PARSEC airfoil fitting code, named as AirfoilPARSEC, that can be fit for a known airfoil geometry with PARSEC parameterization
  - CST code that provides airfoil geometry optimization
  - PARSEC code that provides airfoil geometry optimization

- BEM tool, named as AeroBEM, that calculates power and thrust of the given wind turbine rotor robustly
- Extrapolation tool to get  $360^0$  polars for high AoA values after stall
- Optimization of
  - Selected individual airfoil geometries with both CST and PARSEC methods
  - Wind turbine blades for sectional airfoil profiles, chord length and twist angle distributions along blade span.

A brief flowchart of HAWT rotor design tools developed in this study is given in Figure 1.6.

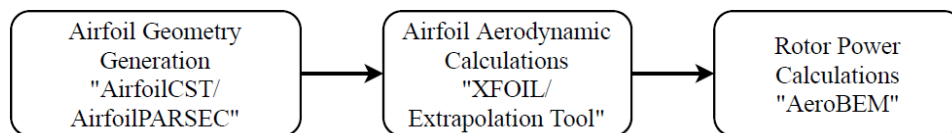


Figure 1.6. Flowchart of HAWT Rotor Design Methodology

### 1.3. The Scope of the Thesis

In Chapter 1, a brief introduction, literature review, objectives of the work and the scope of the study are stated. In Chapter 2, complete methodology is reviewed. Firstly, airfoil representation methods are described in detail. Secondly, CST and PARSEC methods are explained. After that, BEM theory is introduced with its modifications and convergence issues. At the end, GA is presented briefly. In Chapter 3, airfoil optimization studies are presented. At the beginning, CST fitting validation results and the relations between airfoil geometry and the CST weighing coefficients are investigated. Later, PARSEC fitting validation is done. Then, airfoil geometry optimizations for different sections of blade using CST are performed and results are discussed. Lastly, different airfoil optimizations using PARSEC are performed. In Chapter 4, the blade optimization work is explained. Primarily, validation studies for two test turbines, NREL Phase III and NREL Phase VI are shown. Afterwards, chord length and twist angle optimizations of a wind turbine blade is carried out for CST

optimized airfoil profiles obtained in previous chapter. Finally, the performance of newly designed blade is examined elaborately. In Chapter 5, summary, conclusions and recommendations for future work are presented.



## CHAPTER 2

### METHODOLOGY

#### 2.1. Airfoil Basics

In this section, an overview of airfoil basics has stated and airfoil representation methods have briefly summarized. Then the theoretic background on CST and PARSEC methods that are used in this thesis have given in the following parts.

##### 2.1.1. Overview

An airfoil is the term used to describe the cross-sectional shape of an aerodynamic body. The aerodynamic forces inducing on an airfoil arises due to the pressure difference between the suction and pressure surfaces. Airfoil geometry can be often characterized by maximum thickness, maximum camber, maximum thickness location, maximum camber location, and leading edge nose radius. Specific purpose airfoils can be designed basically by changing abovementioned properties. In Figure 2.1, a typical airfoil shape is given. This airfoil has a moderate leading edge nose radius, maximum camber near the leading edge, maximum thickness near the leading edge, sharp trailing edge. At the same time, in Figure 2.2, an example of modern design airfoil is shown. It has high leading edge nose radius, blunt trailing edge, thicker distribution and a cusp near the trailing edge. Maximum camber and maximum thickness locations are shifted to the aft end of the airfoil.

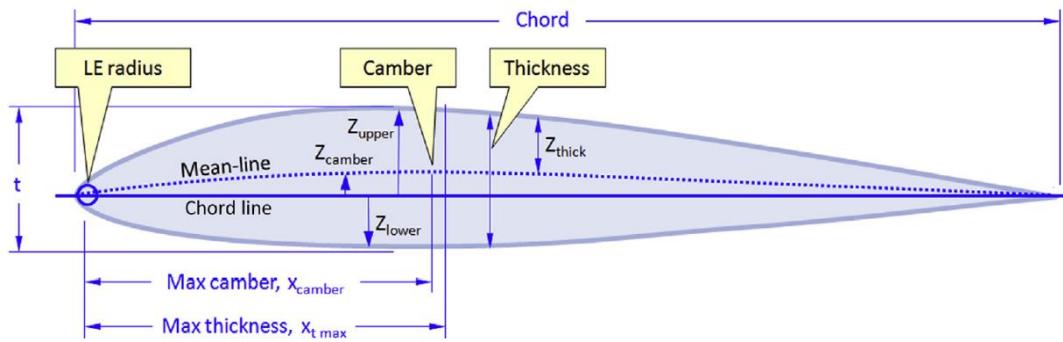


Figure 2.1. Typical Airfoil Nomenclature [46]

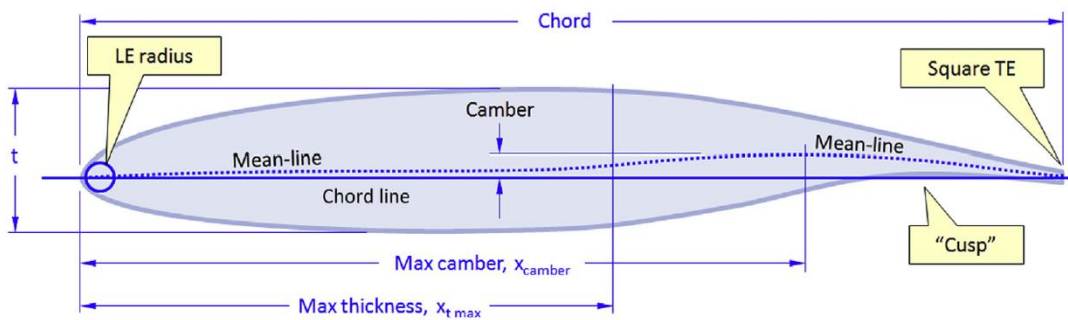


Figure 2.2. Modern Airfoil Nomenclature [46]

When airfoil design approaches have investigated, two basic approaches are obtained: direct and inverse design methodologies. In direct design approach, firstly airfoil geometry is formed and then its aerodynamic performance is investigated deeply. By modifying the baseline geometry, the aerodynamic performance is aimed to be improved. On the other hand, in inverse design methodology, the desired velocity distribution profile over the airfoil is designated beforehand. The design effort is concentrated on finding the specific airfoil geometry that generates input velocity profile. In this thesis study, direct design approach is followed.

### 2.1.2. Airfoil Representation Methods

In this section, a review of airfoil geometry representation methods that can be used for aerodynamic shape optimization has briefly summarized [18], [56]. They can be divided into two as constructive or deformative methods. Constructive methods have represented the airfoil geometry based on a series of parameters. Polynomial and

spline representations, PDE methods, PARSEC and CST are the examples of this method. On the other hand, deformative methods has split the basis airfoil and deform it to form the new geometry. Discrete, analytical, basis vector approaches and free-form deformation (FFD) methods are the examples of deformative methods.

1) Discrete set of airfoil coordinates: A discrete set of airfoil coordinates, so called ordinate tables, is used directly as design variables. Although this method is easy to implement, it has a lot of drawbacks namely need of high number of design variables (especially at the nose region), usage in optimization problems is expensive and difficult to compute, lack of a smooth geometry assurance, difficulty in defining and controlling geometry near the airfoil nose.

2) Bezier Curve, B-Spline Curve and Non-Uniform Rational B-Spline (NURBS): The Bezier curve representation is a powerful method for shape optimization of simple curves. On the other hand, for complex curves, using a single high order Bezier curve is prone to round-off errors and it is highly costly in computational point of view. Therefore, one step beyond B-spline curve representation is developed by defining a composite string of low order Bezier curves. Unfortunately, the airfoil nose representation is weak in both methods. It is needed to segment the airfoil for accurate representation. Non-Uniform Rational B-Spline (NURBS) is a particular type of B-Spline curves used in airfoil design. This is a vector-valued, piecewise, polynomial function. It has all advantages of B-Splines. Additionally, this representation ensures local modifications to airfoil geometry.

3) “Free-form”: In this representation, the geometry is defined as a linear combination of general basis functions. It utilizes a set of control points as parameters.

4) Orthogonal basis functions: A set of orthogonal basis functions numerically derived from existing airfoil families is used to represent airfoil geometry. Since derived basis functions are dependent on particular airfoil families, there are some hesitations about the validity of this method for all airfoil shapes.

5) Polynomial and Spline Control Points: In these methods, airfoil geometry is parameterized by the use of polynomial and spline representations. The number of design variables are decreased with respect to discrete airfoil coordinate representation. On the other hand, it is susceptible to round-off errors and the nose and trailing edge geometry is kept constant during shape optimization applications due to singularity and closure concerns. It is needed to segment the airfoil for accurate representation.

6) Function of Important Physical Parameters: This geometrical approach aims to represent airfoil geometry as a function of its physical parameters. A well-known example of geometric approach is Sobieczky's study, 2000, Parametric Section (PARSEC) method defines the airfoil by using 12 basic design parameters [16]. The biggest handicap in this method is limited freedom, as a result of translation of the geometry changes to related physical design parameters.

7) Perturbations to a Reference Airfoil: In this analytical approach, a set of shape functions is added the reference airfoil geometry to perturb initial geometry smoothly. Hicks Henne functions, Chebyshev polynomials and Legendre polynomials can be given as perturbation function examples. This method is flexible and allows to work on a local region of airfoil. From another point of view, this method is not easily understood or grasped by intuition most of the time, due to the changing the airfoil shape by changing perturbation function variables.

In design and optimization of studies, the expected properties of a favorable airfoil geometric representation method are listed as:

- Continuous, smooth and reasonable geometry
- Flexible structure
- Permitting local sectional control and editing
- Systematic and consistent
- Robustness
- Low number of design variables

In this thesis study, CST and PARSEC methods are chosen as airfoil representation methods and investigated in detail.

### 2.1.3. Class-Shape Transformation (CST) Method

CST Method is a special transformation method characterized by Kulfan [18], mostly used to represent aerodynamic curves and surfaces. It composes of the combination of two basic functions; class and shape functions. The class function does a main categorization of the geometry whereas the shape function defines the special shape.

In this study, the main concentration is on the round nose airfoil geometry. The generalized formulization of this geometry scaled to the chord length can be interpreted as;

$$y(x) = \underbrace{\sqrt{x}}_I \cdot \underbrace{(1-x)}_{II} \cdot \underbrace{\sum_{i=0}^N A_i \cdot x^i}_{III} + \underbrace{x \cdot y_{TE}}_{IV} \quad (2.1.1)$$

- I: Round nose radius related term;
- II: Sharp trailing edge related term;
- III: Unique geometry between nose and end related term;
- IV: Trailing edge thickness related term.

#### 2.1.3.1. Shape Function Definition

Due to the round nose radius geometry at the leading edge, equation 2.1.1 shows non-analytical behavior. To get rid of this behavior, CST offers a the shape function,  $S(x)$ , which is defined as;

$$S(x) = \frac{y(x) - x \cdot y_{TE}}{\sqrt{x} \cdot [1 - x]} \quad (2.1.2)$$

$S(x)$  can be redefined as a weighted summation as follows;

$$S(x) = \sum_{i=0}^N [A_i \cdot x^i] \quad (2.1.3)$$

For the specific limiting values of the  $S(x)$ ; a direct relation between the leading edge radius, the trailing edge thickness and the boat-tail angle can be correlated. In equation 2.1.4, the shape function formulation of the leading edge nose radius is given. In equation 2.1.5, the shape function formulation of the trailing edge thickness and the boat-tail angle is shown. Thus, making shape function transformation and limiting it as mentioned, bring a useful approach to control decisive characteristics of airfoil geometry.

$$x = 0; \quad S(0) = \sqrt{2R_{LE}} \quad (2.1.4)$$

$$x = 1; \quad S(1) = \tan \beta + y_{TE} \quad (2.1.5)$$

### 2.1.3.2. Class Function Definition

The class function,  $C(x)$ , defines the primary class of the geometries.  $C(x)$  is described as;

$$C_{N2}^{N1}(x) = (x)^{N1}[1 - x]^{N2} \quad (2.1.6)$$

where  $N1$  and  $N2$  are the class function coefficients. These coefficients specify the geometry class. For the round nose and pointed aft end airfoil geometry, by turning back to the equation 2.1.1 and combining first and second terms,  $N1=0.5$  and  $N2=1.0$ . Consequently, the class function,  $C(x)$  for this type of airfoils becomes;

$$C_1^{0.5}(x) = (x)^{0.5}[1 - x] \quad (2.1.7)$$

### 2.1.3.3. Shape Function Representation of an Airfoil

The fundamental baseline airfoil is defined as the unit shape function. The unit shape function is the elementary of the entire shape functions and valued as unity.

$$S(x) = 1 \quad (2.1.8)$$

The leading edge radius, the boat-tail angle, the maximum thickness value and the location of maximum thickness are the crucial variables in airfoil geometry design. Making parametric variations to unit shape function results altering the fundamental airfoil geometry by providing a controlled design space for these significant variables.

#### 2.1.3.4. Shape Function Decomposition to Basis Functions

By taking the advantage of “partition of unity” property of the Bernstein polynomials, the unit shape function can be interpreted as on the basis of Bernstein polynomials. This kind of description assures a systematic, well-known and simple approach to represent the airfoil shape function. By taking these polynomials as basis functions of shape functions, the unit shape function can be redefined as;

$$S_i(x) = K_i x^i (1 - x)^{n-1} \quad (2.1.9)$$

$$K_i \equiv \binom{n}{i} = \frac{n!}{i! (n - i)!} \quad (2.1.10)$$

#### 2.1.3.5. CST Airfoil Representation

CST formulization of an airfoil can be summarized as:

$$y(x) = C_{N2}^{N1}(x) \cdot S(x) + x \cdot y_{TE} \quad (2.1.11)$$

The equation 2.1.11 can be separated and written one by one for upper and lower airfoil curves;

$$y(x)_{upper} = C_1^{0.5}(x) \cdot S_{upper}(x) + x \cdot y_{TE,upper} \quad (2.1.12)$$

$$y(x)_{lower} = C_1^{0.5}(x) \cdot S_{lower}(x) + x \cdot y_{TE,lower} \quad (2.1.13)$$

where

$$S_{upper}(x) = \sum_{i=0}^n [A_{upper\ i} \cdot S_i(x)] \quad (2.1.14)$$

$$S_{lower}(x) = \sum_{i=0}^n [A_{lower\ i} \cdot S_i(x)] \quad (2.1.15)$$

Consequently, in CST method the weight coefficients  $A_{upper\ i}$  and  $A_{lower\ i}$ , can be called as the decisive parameters. When designing new airfoil geometries subject to specific performance targets, they become design variables in the optimization process. On the other hand, when a prespecified airfoil geometry is desired to be represented by the CST method, these coefficients are found by means of curve fitting techniques.

A generic, i.e. very general, parametric definition method for the airfoil, Bezier curves, can also be used as examined in Polat et al.'s studies [5-8]. Similar to CST representation, Bezier curve method uses Bernstein polynomials as basis functions. However, for overall geometry definition, constant weighted coefficients are directly multiplied to Bernstein polynomials. This creates a distributed design space containing improper geometries such as intersecting upper and lower airfoil surfaces. On the other hand, by introducing the class function, CST method guarantees to have airfoil fundamental geometry in every circumstances. Additionally, due to tangency constraints in Bezier curve parameterization method, it is very hard to locally control the geometry with low number of control points. To illustrate, Bezier curve method needs more than 20 control points to define an airfoil properly in most cases. However, CST method is stronger in local geometry control ability with relatively a small number of parameters. Based on Kulfan et al.'s analyses, in CST representation method, high order representations greater than 6<sup>th</sup> order are assumed to be statistically identical. Depending on the complexity of the airfoil geometry, lower order parameterizations can be assigned easily. Considering these strengths, it is deduced that CST method is more powerful than Bezier curve representation.

### 2.1.4. Parametric Section (PARSEC) Method

PARSEC method, defined by Sobieczky in 2000, is a linear combination of explicit mathematical functions derived from specifically basic airfoil characteristic to define airfoil geometry [16]. It uses totally 12 parameters, 6<sup>th</sup> order polynomials are used to represent upper and lower surfaces.

General formulation of PARSEC method is turned to be such that:

$$y_{upper} = \sum_{n=1}^6 A_{upper\ n} x^{n-\frac{1}{2}} \quad (2.4.1)$$

$$y_{lower} = \sum_{n=1}^6 A_{lower\ n} x^{n-\frac{1}{2}} \quad (2.4.2)$$

Similar to CST parameterization,  $A_{upper\ n}$  and  $A_{lower\ n}$  are the weight coefficients of PARSEC formulation. In order to define PARSEC polynomials given in equations 2.4.1 and 2.4.2., these coefficients are needed to be calculated by the help of 12 airfoil geometric parameters. The airfoil geometric parameters are shown in Figure 2.3. and tabulated in Table 2.1.

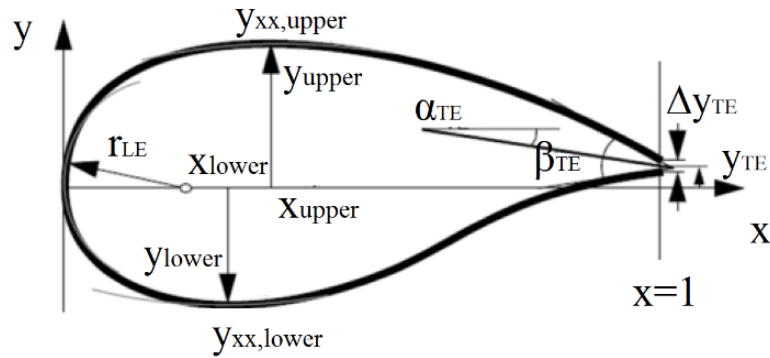


Figure 2.3. PARSEC Geometric Airfoil Parameters [16]

Table 2.1 PARSEC Parameter Definitions [54]

<b>PARSEC Parameter</b>	<b>Parameter Definition</b>	<b>Airfoil Geometric Parameter</b>
p1	The Leading Edge Radius for Upper Curve	$r_{LE,upper}$
p2	The Maximum Thickness x Location for Upper Curve	$x_{upper}$
p3	The Maximum Thickness y Location for Upper Curve	$y_{upper}$
p4	The Upper Crest Curvature	$y_{xx,upper}$
p5	The Maximum Thickness x Location for Lower Curve	$x_{lower}$
p6	The Maximum Thickness y Location for Lower Curve	$y_{lower}$
p7	The Lower Crest Curvature	$y_{xx,lower}$
p8	The Trailing Edge Position	$y_{TE}$
p9	The Trailing Edge Thickness	$\Delta y_{TE}$
p10	The Trailing Edge Angle	$\alpha_{TE}$
p11	The Trailing Edge Wedge Angle	$\beta_{TE}$
p12	The Leading Edge Radius for Lower Curve	$r_{LE,lower}$

Two linear systems of equations are set up as follows relating airfoil geometric parameters and PARSEC general polynomial formulation to find PARSEC weight coefficients of upper and lower surfaces;

$$C_{upper} \times A_{upper} = B_{upper} \quad (2.4.3)$$

$$C_{lower} \times A_{lower} = B_{lower} \quad (2.4.4)$$

$$C_{upper} = \begin{bmatrix} 1 & 0 & 0 & 0 & 0 & 0 \\ \frac{1}{p_2^2} & \frac{3}{p_2^2} & \frac{5}{p_2^2} & \frac{7}{p_2^2} & \frac{9}{p_2^2} & \frac{11}{p_2^2} \\ \frac{1}{2} & \frac{3}{2} & \frac{5}{2} & \frac{7}{2} & \frac{9}{2} & \frac{11}{2} \\ \frac{1}{2} p_2^{-1} & \frac{3}{2} p_2^{-1} & \frac{5}{2} p_2^{-1} & \frac{7}{2} p_2^{-1} & \frac{9}{2} p_2^{-1} & \frac{11}{2} p_2^{-1} \\ -\frac{1}{4} p_2^{-3} & \frac{3}{4} p_2^{-1} & \frac{15}{4} p_2^{-1} & \frac{35}{4} p_2^{-1} & \frac{53}{4} p_2^{-1} & \frac{99}{4} p_2^{-1} \\ 1 & 1 & 1 & 1 & 1 & 1 \end{bmatrix} \quad (2.4.5)$$

$$B_{upper} = \begin{bmatrix} \sqrt{2p_1} \\ p_3 \\ \tan(p_{10} - \frac{p_{11}}{2}) \\ 0 \\ p_4 \\ p_8 + p_9/2 \end{bmatrix} \quad (2.4.6)$$

$$C_{lower} = \begin{bmatrix} 1 & 0 & 0 & 0 & 0 & 0 \\ \frac{1}{p_5^2} & \frac{3}{p_5^2} & \frac{5}{p_5^2} & \frac{7}{p_5^2} & \frac{9}{p_5^2} & \frac{11}{p_5^2} \\ \frac{1}{2} & \frac{3}{2} & \frac{5}{2} & \frac{7}{2} & \frac{9}{2} & \frac{11}{2} \\ \frac{1}{2} p_5^{-1} & \frac{3}{2} p_5^{-1} & \frac{5}{2} p_5^{-1} & \frac{7}{2} p_5^{-1} & \frac{9}{2} p_5^{-1} & \frac{11}{2} p_5^{-1} \\ -\frac{1}{4} p_5^{-3} & \frac{3}{4} p_5^{-1} & \frac{15}{4} p_5^{-1} & \frac{35}{4} p_5^{-1} & \frac{53}{4} p_5^{-1} & \frac{99}{4} p_5^{-1} \\ 1 & 1 & 1 & 1 & 1 & 1 \end{bmatrix} \quad (2.4.7)$$

$$B_{lower} = \begin{bmatrix} -\sqrt{2p_{12}} \\ p_6 \\ \tan(p_{10} + \frac{p_{11}}{2}) \\ 0 \\ p_4 \\ p_8 - p_9/2 \end{bmatrix} \quad (2.4.8)$$

Since the system is completely defined, the PARSEC coefficient matrices  $A_{upper}$  and  $A_{lower}$  can be solved as follows;

$$A_{upper} = C_{upper}^{-1} \times B_{upper} \quad (2.4.9)$$

$$A_{lower} = C_{lower}^{-1} \times B_{lower} \quad (2.4.10)$$

## **2.2. Rotor Aerodynamics**

In this part, fundamentals of wind turbine rotor aerodynamics are introduced. Starting from Momentum Theory, Blade Element Theory, and BEM Theory are covered. Furthermore, corrections to BEM and converge issues are dealt with as separate sections.

### **2.2.1. Momentum Theory**

#### **2.2.1.1. One Dimensional Axial Momentum Theory**

One Dimensional Axial Momentum Theory for an ideal turbine is explained in this section. The basic assumptions of the theory is given as;

- The static pressure at far incoming stream and far downstream is equal to the uninterrupted ambient static pressure.
- The flow is homogenous, incompressible and steady state.
- The actuator disc is considered as having infinite number of blades.
- The actuator disc is ideal with no frictional drag hence the system is conservative.
- The wake is not rotating.
- Thrust is uniform over the actuator disc area.

The rotor is modeled as an actuator disc which slows the wind speed and causes a pressure drop as shown in Figure 2.4.

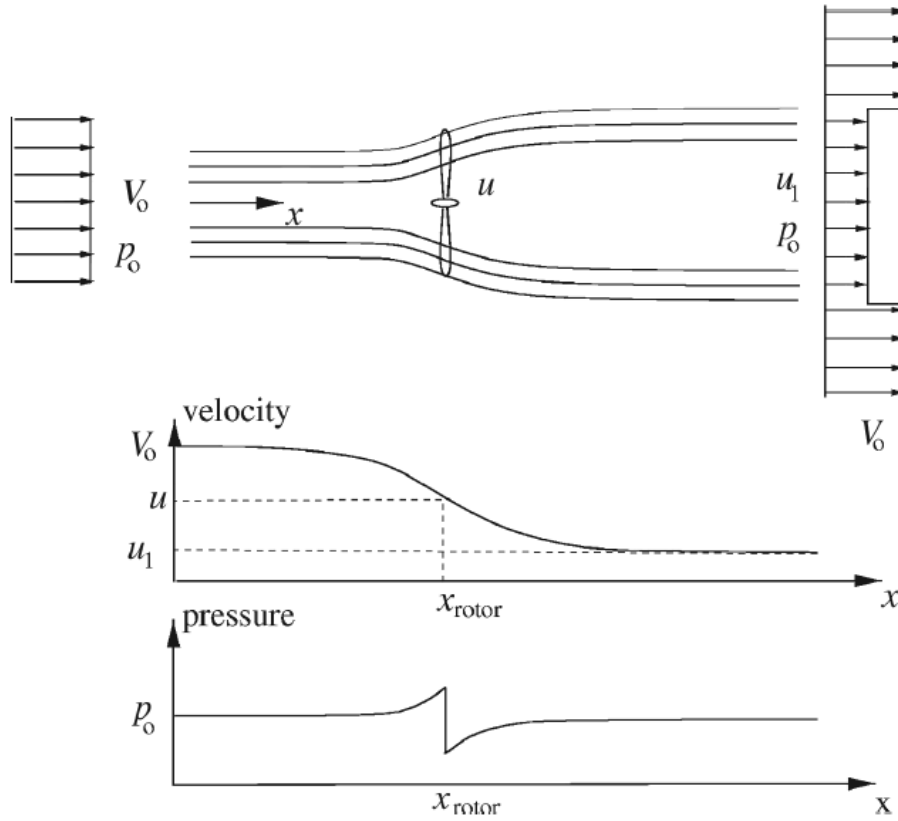


Figure 2.4. Actuator Disc Model with Pressure and Axial Velocity Diagrams [29]

This pressure drop is used to calculate thrust force.

$$T = \Delta p A \quad (2.2.1)$$

Bernoulli equations are written for upstream in equation 2.2.2 and for downstream in equation 2.2.3 as follows;

$$P_0 + \frac{1}{2} \rho V_0^2 = p + \frac{1}{2} \rho u^2 \quad (2.2.2)$$

$$p - \Delta p + \frac{1}{2} \rho u^2 = P_0 + \frac{1}{2} \rho u_1^2 \quad (2.2.3)$$

$\Delta p$  is found from equation 2.2.2 and equation 2.2.3 as;

$$\Delta p = \frac{1}{2} \rho (V_0^2 - u_1^2) \quad (2.2.4)$$

A circular control volume around a wind turbine is shown in Figure 2.5.

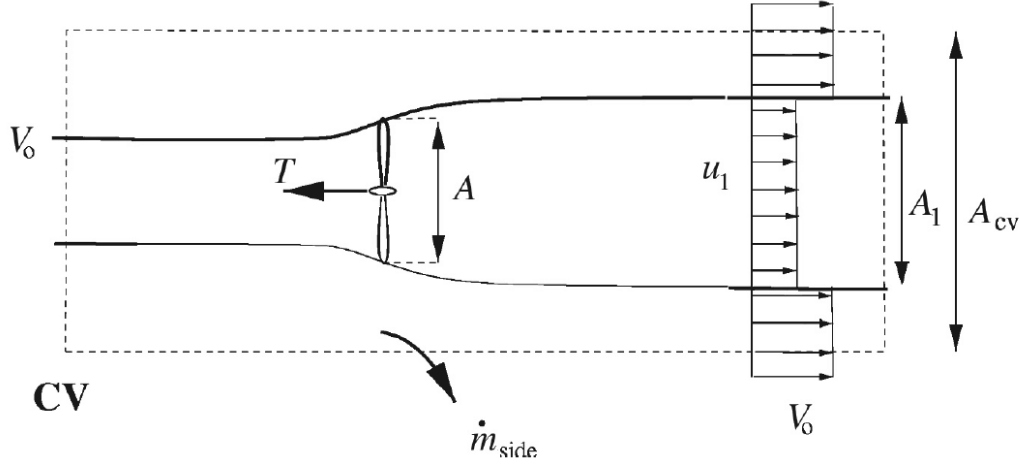


Figure 2.5. A Circular Control Volume around a Wind Turbine [29]

The axial momentum equation can be written as

$$-T = \rho u_1^2 A_1 + \rho V_0^2 (A_{cv} - A_1) + \dot{m}_{side} V_0 - \rho V_0^2 A_{cv} \quad (2.2.5)$$

where  $\dot{m}_{side}$  is calculated from conservation of mass as;

$$\rho A_{cv} V_0 = \rho A_1 u_1 + \rho (A_{cv} - A_1) V_0 + \dot{m}_{side} \quad (2.2.6)$$

$$\dot{m}_{side} = \rho A_1 (V_0 - u_1) \quad (2.2.7)$$

From the conservation of mass equations, mass flow rate is found as;

$$\dot{m} = \rho u A = \rho u_1 A_1 \quad (2.2.8)$$

By using equation 2.2.5, equation 2.2.7, and equation 2.2.8, thrust can be written as;

$$T = \rho u A (V_0 - u_1) = \dot{m} (V_0 - u_1) \quad (2.2.9)$$

By combining equation 2.2.1, equation 2.2.4, and equation 2.2.9, the velocity at the rotor plane can be found as;

$$u = \frac{1}{2}(V_0 + u_1) \quad (2.2.10)$$

The axial induction factor,  $a$ , is defined as;

$$a = \frac{V_0 - u}{V_0} \quad (2.2.11)$$

By using equation 2.2.11, the velocity at the rotor plane can be rewritten in the form of equation 2.2.12.

$$u = (1 - \alpha)V_0 \quad (2.2.12)$$

By using equation 2.2.10 and equation 2.2.11, the downstream velocity can be rewritten in the form of equation 2.2.13.

$$u_1 = (1 - 2\alpha)V_0 \quad (2.2.13)$$

Power can be calculated as;

$$P = \dot{m} \left( \frac{1}{2}V_0^2 + \frac{P_0}{\rho} - \frac{1}{2}u_1^2 - \frac{P_0}{\rho} \right) \quad (2.2.14)$$

By combining equation 2.2.8 and equation 2.2.14, power equation is simplified as;

$$P = \frac{1}{2}\rho u A (V_0^2 - u_1^2) \quad (2.2.15)$$

By combining equation 2.2.13 and equation 2.2.15, power equation can be written as a function of axial induction factor such that;

$$P = 2\rho V_0^3 (1 - \alpha)^2 A \quad (2.2.16)$$

Similarly, thrust relation in the equation 2.2.9 can be rewritten as a function of axial induction factor such that;

$$T = 2\rho V_0^2 (1 - \alpha) A \quad (2.2.17)$$

### 2.2.1.2. Glauert Optimum Rotor

In One Dimensional Axial Momentum Theory, the rotational effects in the flow are ignored. Glauert defined an optimum rotor having a rotational wake having tangential induction factor,  $a'$ . Figure 2.6, velocity triangles given for Glauert optimum rotor where  $C_a$  is the axial velocity component, and  $C_\theta$  is the tangential velocity component.

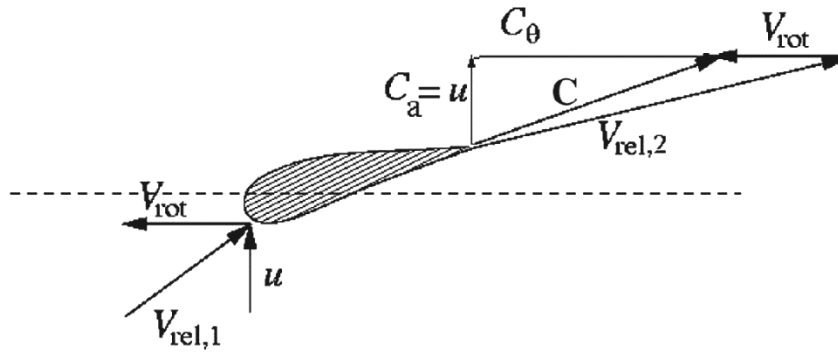


Figure 2.6. The Induced Velocities for Glauert Optimum Rotor [29]

Similar to axial velocity relation given in equation 2.2.12, tangential velocity relation can be defined as follows;

$$C_\theta = 2\alpha'\omega r \quad (2.2.18)$$

By applying Euler's turbine equation to an infinitesimally small control volume having thickness  $dr$ ,  $dP$  can be formulated as;

$$dP = \dot{m}\omega r C_\theta = 2\pi r^2 \rho u C_\theta dr \quad (2.2.19)$$

By combining equation 2.2.19 with equation 2.2.18,  $dP$  can be rewritten as;

$$dP = 4\pi\rho\omega^2 V_0 \alpha' (1 - \alpha) r^3 dr \quad (2.2.20)$$

### 2.2.2. Blade Element Theory

In this section, Blade Element Theory is presented in detail. It is assumed that the rotor blade is formed of two dimensional independent blade elements. By calculating the force balance on blade element, power and torque can be obtained. The basic assumptions of the theory is given as;

- Blade elements are isolated from each other, there is no aerodynamic interaction between each other.
- Only induced forces on blade elements are originated from airfoil aerodynamic forces; lift and drag.

The angle of attack,  $\alpha$ , of blade is given as;

$$\alpha = \varphi - \theta \quad (2.2.21)$$

The twist angle,  $\theta$ , is given as;

$$\theta = \theta_p + \beta \quad (2.2.22)$$

The velocity triangle of the blade element is given in Figure 2.7. From the velocity triangle, a relation between these angles and velocities can be derived as;

$$\tan \varphi = \frac{(1 - \alpha)V_0}{(1 + \alpha')\omega r} \quad (2.2.23)$$

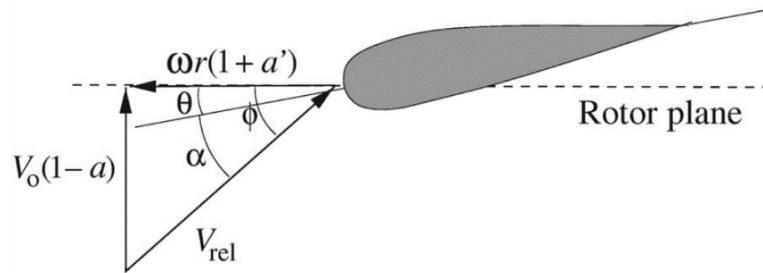


Figure 2.7. The Velocity Triangle of Blade Element [29]

From two dimensional aerodynamics, the reaction force,  $F$ , on the airfoil is decomposed to two components. The component perpendicular to the freestream velocity direction is the lift force,  $L$ , whereas the component parallel to the freestream velocity direction is the drag,  $D$ . These forces are illustrated in Figure 2.8.

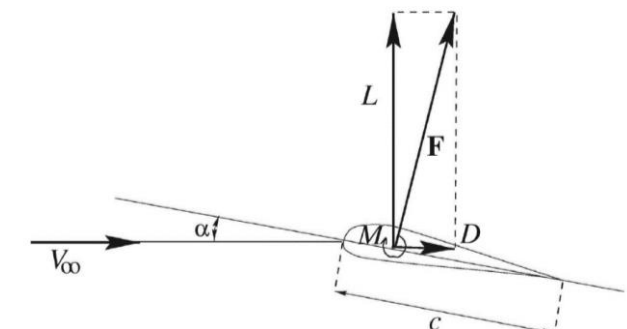


Figure 2.8. Lift and Drag Forces Acting on an Airfoil [29]

Lift and drag can be computed as respectively;

$$L = \frac{1}{2} \rho c V_{rel}^2 C_l \quad (2.2.24)$$

$$D = \frac{1}{2} \rho c V_{rel}^2 C_d \quad (2.2.25)$$

Similar to the airfoil, the forces induced on the blade element on the rotor plane are demonstrated in Figure 2.9.  $R$  is the total resulting force, where  $P_N$  is the normal force component and  $P_T$  is the tangential force component.

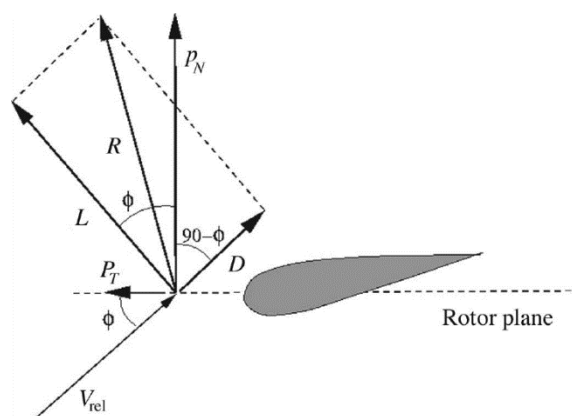


Figure 2.9. The Forces on Blade Element [29]

$$P_N = L \cos \varphi + D \sin \varphi \quad (2.2.26)$$

$$P_T = L \sin \varphi - D \cos \varphi \quad (2.2.27)$$

By using lift and drag forces and normalizing the forces acting on the rotor plane with respect to  $\frac{1}{2}\rho V_{rel}^2 c$ , the equations are deduced as;

$$C_n = C_l \cos \varphi + C_d \sin \varphi \quad (2.2.28)$$

$$C_t = C_l \sin \varphi - C_d \cos \varphi \quad (2.2.29)$$

By turning back to Figure 2.7, it can be deduced that the linkage between  $V_{rel}$  and induction factors as such;

$$V_{rel} \sin \varphi = V_0(1 - \alpha) \quad (2.2.30)$$

$$V_{rel} \cos \varphi = \omega r(1 + \alpha') \quad (2.2.31)$$

At this point, solidity,  $\sigma$ , is introduced as the ratio of blade area to the disk area swept out by the blades. It is presented in equation 2.2.32 where  $B$  is the number of blades and  $c(r)$  is the local chord length.

$$\sigma(r) = \frac{c(r)B}{2\pi r} \quad (2.2.32)$$

The total normal force which is the thrust force on the blade element section and the total tangential force which is the torque on the blade element section can be written as;

$$dT = BP_N dr \quad (2.2.33)$$

$$dM = rBP_T dr \quad (2.2.34)$$

Recalling the  $C_n$  and  $C_t$  definitions as follows;

$$C_n = \frac{P_N}{\frac{1}{2}\rho V_{rel}^2 c} \quad (2.2.35)$$

$$C_t = \frac{P_T}{\frac{1}{2}\rho V_{rel}^2 c} \quad (2.2.36)$$

Combining the equations 2.2.30, 2.2.31, 2.2.35, 2.2.36; the equations 2.2.33 and 2.2.34 can be reorganized as;

$$dT = \frac{1}{2}\rho B \frac{V_0^2(1-\alpha)^2}{\sin^2 \varphi} c C_n dr \quad (2.2.37)$$

$$dM = \frac{1}{2}\rho B \frac{V_0(1-\alpha)\omega r(1+\alpha')}{\sin \varphi \cos \varphi} c C_t r dr \quad (2.2.38)$$

Thus, from the aerodynamic force balance of the blade element; elemental thrust and torque are formulized in equations 2.2.37 and 2.2.38.

### 2.2.3. Blade Element Momentum (BEM) Theory

The Blade-Element Momentum (BEM) theory is formed by equating the force and torque values obtained separately from the Blade Element Theory and Momentum Theory. Blade Element Theory calculates the forces generated by aerodynamic loads, lift and drag forces created by blade sections along the span of the blade. Momentum Theory establishes the momentum balance for a rotating annular streamtube passing through the control volume of the turbine. The forces on finite number of blade elements creates the momentum change in the swept annulus. BEM basically finds the induced velocities by calculating the corresponding axial and tangential induction factors,  $a$  and  $a'$ . Thus, the thrust and torque calculations can be done by using them.

$$T_{blade\ element} = T_{momentum} \quad (2.2.39)$$

$$Q_{blade\ element} = Q_{momentum} \quad (2.2.40)$$

$$a = \frac{1}{\frac{4 \sin^2 \varphi}{\sigma C_n} + 1} \quad (2.2.41)$$

$$a' = \frac{1}{\frac{4 \sin \varphi \cos \varphi}{\sigma C_t} - 1} \quad (2.2.42)$$

#### 2.2.4. Modifications to BEM

BEM theory is a powerful tool to estimate wind turbine performance fast and easily. However, due to the rough assumptions of the theory, it has some limitations. In order to improve the performance of BEM theory, some corrections are proposed. In this section, the crucial modifications have given in the following sections.

##### 2.2.4.1. Hub and Tip Loses

As it is already stated in Momentum Theory assumptions, the rotor is idealized as an actuator disc having infinite number of blades. However, the actual rotor wake is different from than this ideal rotor's. When three dimensional aerodynamics is examined, it has been revealed that because of the pressure difference between suction and the pressure side of not only turbine blades but also any lifting surfaces, an interaction occurs between these sides at the boundaries of the geometry. This interaction creates a spanwise pressure gradient on the wind turbine blade resulting a flow from pressure side to suction side. Consequently, the tip and hub vortices are formed as illustrated in Figure 2.10.

For the tip vortex shedding, Prandtl deduced a tip correction factor,  $F_{tip}$ , as follows;

$$F_{tip} = \frac{2}{\pi} \cos^{-1}(e^{-f_{tip}}) \quad (2.2.43)$$

$$f_{tip} = \frac{B(R-r)}{2r \sin \varphi} \quad (2.2.44)$$

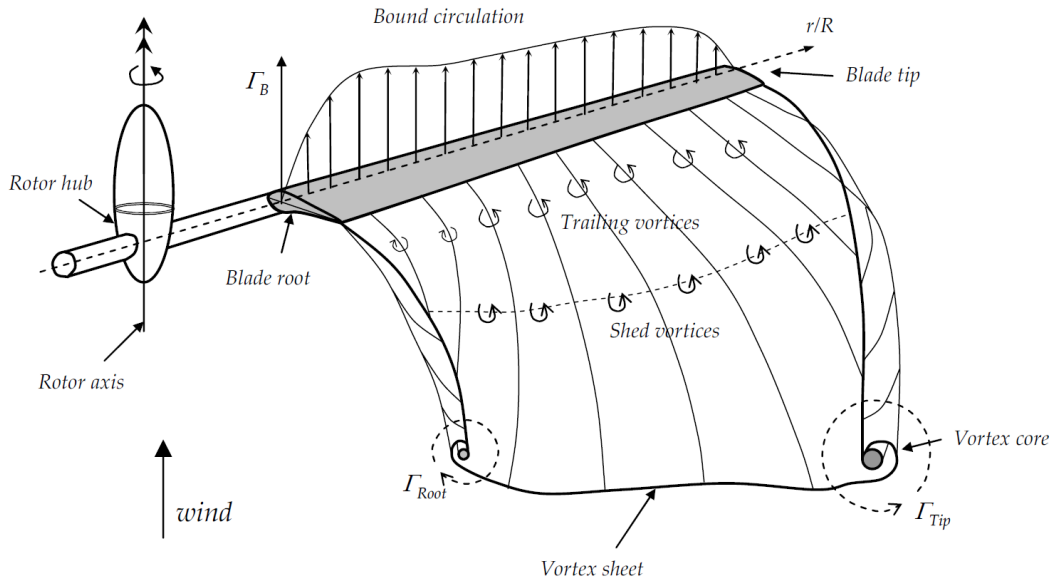


Figure 2.10. The Vortex Sheet Formation behind the Wind Turbine Blade [51]

Similarly, in order to correct the shedding vortex near the rotor hub, a hub correction factor,  $F_{hub}$ , is described as follows;

$$F_{hub} = \frac{2}{\pi} \cos^{-1}(e^{-f_{hub}}) \quad (2.2.45)$$

$$f_{hub} = \frac{B}{2} \frac{(r - R_{hub})}{r \sin \varphi} \quad (2.2.46)$$

To be able to determine total influence caused by tip and hub vortices on the blade element, a total correction factor,  $F$ , is exposed as;

$$F = F_{hub} \cdot F_{tip} \quad (2.2.47)$$

Consequently, the thrust and torque formulas coming from Momentum Theory are needed to be corrected. The axial and tangential induction factors previously introduced in equations 2.2.41 and 2.2.42 are corrected by this total correction factor  $F$  in equation 2.2.47, yielding;

$$a = \frac{1}{\frac{4 F \sin^2 \varphi}{\sigma C_n} + 1} \quad (2.2.48)$$

$$a' = \frac{1}{\frac{4 F \sin \varphi \cos \varphi}{\sigma C_t} - 1} \quad (2.2.49)$$

### 2.2.4.2. Highly Loaded Rotor Correction

The thrust coefficient,  $C_T$ , can be introduced as follows;

$$C_T = \frac{dT}{\frac{1}{2} \rho V_0^2 2\pi r dr} \quad (2.2.50)$$

When wind turbine operates at high tip to speed ratio values, the axial induction factor reaches to high values. After  $a$  exceeds nearly 0.3-0.5, the turbine becomes highly loaded and the rotor enters the turbulent wake state. Due to the high turbulence in the wake, flow behind the rotor slows while the thrust continues to increase. Glauert obtained an empirical relation by correlating the experimental helicopter data. The comparison of empirical data, Glauert correction results and BEM theory without highly loaded rotor correction results are shown in Figure 2.11.

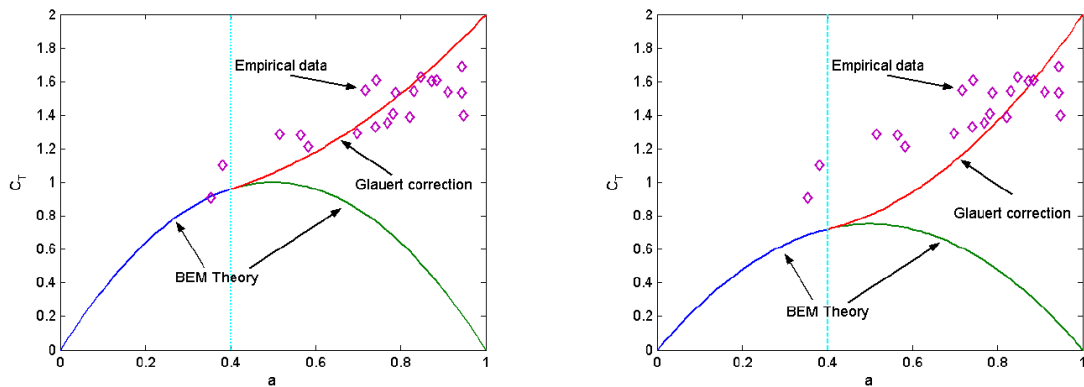


Figure 2.11. Comparison of Different  $C_T$  Values – Empirical, Glauert Correction and BEM Calculation without Any Correction Results [33]

By adding the total loss correction factor,  $F$ , and setting the critical transition value,  $a$ , as 0.4, Buhl [52], 2005, derived a modification to the Glauert empirical relation that as follows:

$$C_T = \left(\frac{50}{9} - 4F\right)a^2 - \left(\frac{40}{9} - 4F\right)a + \frac{8}{9} \quad (2.2.51)$$

In this study for highly loaded rotor correction, Buhl's relation is used.

### 2.2.5. Convergence Issues

There are a lot of methods to calculate axial and tangential induction factors. However, almost all of them are neither able to converge at all solution domain nor easy to compute efficiently. Ning [22], 2013, suggested a simple and robust algorithm to solve as previously mentioned in Literature Review section. In this study, to prevent convergence problems, Ning's solution method is used to compute induction factors.

In Ning's method, instead of solving two nonlinear equations, the equations 2.2.48 and 2.2.49 simultaneously, solution of same BEM governing equations are reduced to finding roots of one dimensional nonlinear residual equation, the local inflow angle,  $\varphi$ . It is much easier to solve residual equation, because there are simple, fast and forceful methods to solve one dimensional root finding algorithms such as Brent's method.

The solution algorithm assigns an initial value for  $\varphi$ , calculates corresponding local AoA, and computes  $C_l$  and  $C_d$  then  $C_n$  and  $C_t$  values, after that estimates induction factors, checks prespecified error value until finding the root of the residual function. In order to implement this procedure, solution domain is divided into two as the momentum/empirical region and propeller brake region.

First of all, momentum/empirical region is examined. The axial induction factor is parameterized as a function of local flow angle,  $\varphi$ , as follows;

$$a(\varphi) = \frac{\kappa(\varphi)}{1 - \kappa(\varphi)} \quad (2.2.52)$$

where 
$$\kappa(\varphi) = \frac{\sigma' C_n(\varphi)}{4F(\varphi)\sin^2(\varphi)} \quad (2.2.53)$$

It should be noted that the equation 2.2.52 is valid only in the region where the momentum theory assumptions are valid. For this momentum valid region, the bounds of the convenience parameter,  $\kappa$ , can be assigned as;

$$-1 < \kappa \leq \frac{\beta}{1 - \beta} \quad (2.2.54)$$

where 
$$\beta = 0.4 \quad (2.2.55)$$

For highly loaded rotor conditions explained in section 2.2.4.2 beforehand, the Buhl's empirical relation, equation 2.2.51, is used to calculate axial induction factor. For this empirical region, equation 2.2.52 is not applicable anymore and the axial induction factor formula should be rearranged based on equation 2.2.51 as follows;

$$a(\varphi) = \frac{\gamma_1 - \sqrt{\gamma_2}}{\gamma_3} \quad (2.2.56)$$

where 
$$\gamma_1 \equiv 2F\kappa - \left(\frac{10}{9} - F\right) \quad (2.2.57)$$

and 
$$\gamma_2 \equiv 2F\kappa - F\left(\frac{4}{3} - F\right) \quad (2.2.58)$$

and 
$$\gamma_3 \equiv 2F\kappa - \left(\frac{25}{9} - 2F\right) \quad (2.2.59)$$

To eliminate singularity when  $\gamma_3$  becomes zero, a very small value,  $\varepsilon$ , is introduced to add to or subtract from  $\kappa$  to be able to keep  $a(\varphi)$  determined with a small error. The error value of  $\varepsilon$  can be in the order of  $10^{-5}$  or so. For this empirical equation valid region, the bounds of the axial induction factor,  $a$ , can be assigned as;

$$0.4 < a \leq 1.0 \quad (2.2.60)$$

where 
$$\kappa \geq \frac{2}{3} \quad (2.2.61)$$

Secondly, propeller brake region is investigated. In this region, axial induction factor is larger than 1.0 and governing momentum equations are used by a sign change resulting;

$$a(\varphi) = \frac{\kappa(\varphi)}{\kappa(\varphi) - 1} \quad (2.2.62)$$

where  $\kappa > 1$  (2.2.63)

Calculation of the tangential induction factor for all regions,  $a'$ , is defined as;

$$a'(\varphi) = \frac{\kappa'(\varphi)}{1 - \kappa'(\varphi)} \quad (2.2.64)$$

where  $\kappa'(\varphi) = \frac{\sigma' C_t(\varphi)}{4F(\varphi)\sin(\varphi)\cos(\varphi)}$  (2.2.65)

Consequently, the induction factors for all cases are parameterized as a function of  $\varphi$ . Brent's method have been used as root finding algorithm. Therefore, the solution domain is divided into regions having no singularity points, in which a root is bracketed properly. In order to define residual function, it is worthwhile to turn back to section 2.2.2 and remember the geometric relation between flow angle and induction factors defined in equation 2.2.23. When defining residual function, it is preferred to have  $(1 - a)$  and  $(1 + a')$  in the denominator. Singularities can be simply found as;

$$\varphi = 0, \mp\pi \quad (2.2.66)$$

These singularities at the boundaries between two solution regions demonstrated in Figure 2.12. The momentum/empirical region is defined for the interval  $(0, \pi)$  and the propeller brake region is defined for the interval  $(-\pi, 0)$ . This interval selection is also coherent with the physics of the problem where flow angles smaller than zero corresponds to propeller brake region and flow angles larger than zero corresponds to momentum/empirical region.

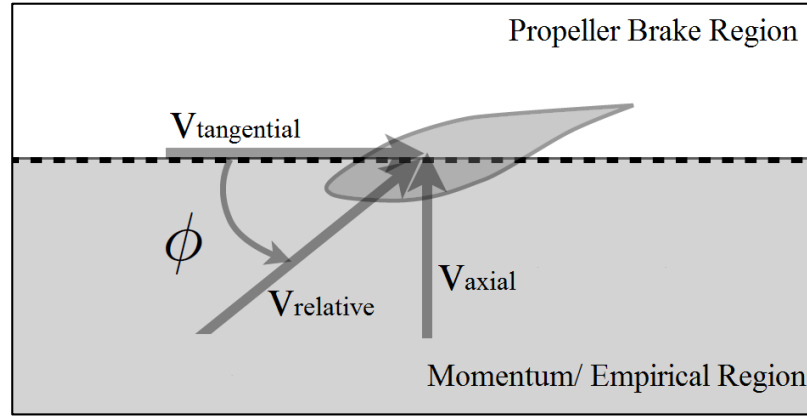


Figure 2.12. Solution Regions for Ning's Method [22]

Most of the wind turbine flow solutions lies at the momentum/empirical region in the specific interval  $(0, \pi/2]$ . The remaining part of the interval,  $(\pi/2, \pi]$ , corresponds to locally reversed tangential flow leading tangential induction factors smaller than -1 which is not physically possible for wind turbine flows. The residual function for this region is defined as follows;

$$f(\varphi) = \frac{\sin \varphi}{1 - a(\varphi)} - \frac{1}{\lambda_r} \cos \varphi (1 - \kappa'(\varphi)) \quad (2.2.67)$$

For propeller brake region, the solution interval is narrowed down to  $[-\pi/4, 0)$ , since the physically meaningful solutions lay in this limited part. The residual function for propeller brake region is defined as follows;

$$f_{pb}(\varphi) = \sin \varphi (1 - \kappa(\varphi)) - \frac{1}{\lambda_r} \cos \varphi (1 - \kappa'(\varphi)) \quad (2.2.68)$$

The general solution algorithm is outlined in Figure 2.13. The procedure is started by seeking the solution in the most probable region, momentum/empirical region. If the solution is not found in this region, propeller brake region is searched. If the solution is still not found, as the last option the root of momentum/empirical residual function is looked for in  $(\pi/2, \pi)$  bracket. After finding root of residual function, namely  $\varphi^*$ , corresponding  $a$  and  $a'$  values are calculated according to proper  $\kappa$  intervals.

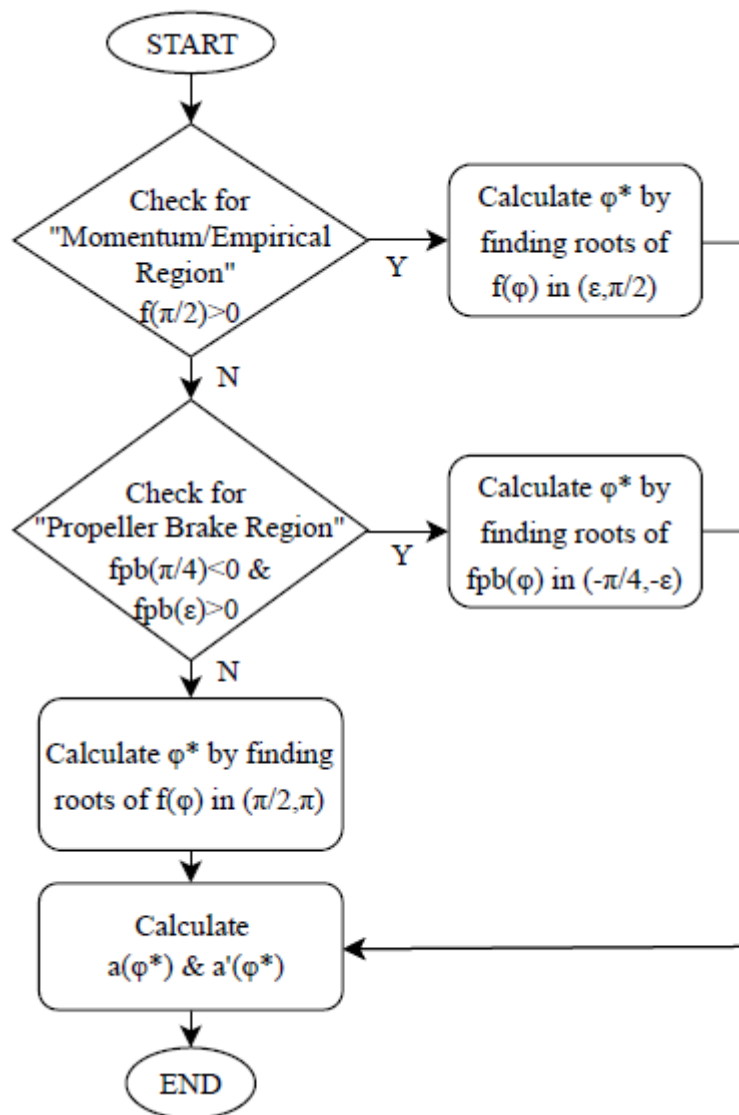


Figure 2.13. BEM Algorithm with Ning's Guaranteed Convergence Method

### 2.3. Potential Flow Solver, XFOIL

In this part, the panel method has shortly mentioned and XFOIL has explained briefly.

For an inviscid, incompressible and irrotational flow, it can be defined a potential function, satisfying the conservation of mass and conservation of momentum laws. Potential functions can be defined for various elementary potential flows such as uniform flow, sink, source, irrotational vortex, flow in the vicinity of inclined wall, etc. Moreover, by superposition of these basic flow potential functions, more complicated flows can be interpreted such as a source and a sink, doublet, a source and a vortex, flow past a half body, flow past a closed body, flow over a cylinder, flow over a rotating cylinder, etc.

The panel method uses potential flow to solve the flow over the airfoil. First of all, the airfoil boundary is divided into straight segments called panels. At the center of the each panel, a vortex and/or a source sheets are placed. As a boundary condition, no flow through the surface is imposed. For the second boundary condition, at the trailing edge Kutta Condition is applied. By solving the resulting system of linear equations, the flow over the airfoil is characterized.

XFOIL, developed by Drela, is an open source panel code combined with fully-coupled viscous/inviscid (VI) interaction method to calculate drag, boundary layer transition and separation [34]. It models the flow over any airfoil, and also perform corrections for viscous and compressible flows. Moreover, it has a new airfoil geometries development feature.

In this study, for the specific flow conditions related blade element, i.e. when the blade elemental  $Re$  and  $AoA$  is given, corresponding  $C_l$  and  $C_d$  values are calculated by XFOIL. For airfoil optimization studies, XFOIL has coupled with optimization code. In optimization routine, XFOIL is called for each new airfoil geometry and after execution XFOIL output file is read to make objective function calculations.

## 2.4. Genetic Algorithm (GA)

Genetic Algorithm (GA) is a multi-objective, semi-random global search and evolutionary optimization technique based on Darwinian Theory of natural selection [35]. GA has advantages for solving especially discrete, discontinuous, ill-behaved and non-differentiable problems having high number of design variables.

GA terminology can be shortly defined as follows:

- **Chromosomes:** It is the genotypic representation or encoding of individuals. The basic types can be arranged as binary encoding, real number encoding, integer or literal permutation encoding, general data structure encoding, etc. [36].
- **Initial population:** The first population is created randomly without exposing any boundary conditions.
- **Fitness and selection:** Fitness is the related to objective function that enables sorting of individuals whereas the selection is determining the fittest individual based on which the survival of the individuals and selection of parents are decided. Roulette wheel selection,  $(\mu+\lambda)$  selection, tournament selection, steady-state reproduction, ranking and scaling, sharing can be given as different types examples of selection methods [36].
- **Cross-over:** It is the exchange process between the parents' selected parts of the chromosomes to form two new individuals. There are a lot of methods to perform cross-over such as arithmetical cross-over, blend cross-over, unimodal normal distribution cross-over, direction based cross-over, etc. [36].
- **Mutation:** It is the random altering one individuals' selected part of the chromosomes.

The optimization algorithm used in this study is summarized step by step as follows:

1. An initial population generation is created with a genetic representation for individuals. In this first step, arbitrary airfoil geometries are created in the number of predefined population size.
2. The fitness function scores for each of these individuals are evaluated. The fitness function is determined as the  $C_l/C_d$  ratio. For each airfoil, this ratio is calculated by computing XFOIL for given flow conditions.
3. Some of the individuals are selected based on their fitness scores to become parents for creation of new generation. The airfoils having higher  $C_l/C_d$  ratio are chosen.
4. The parent individuals undergoes crossover and mutation transformations with a certain probability to create offspring population. For given mutation and crossover rates, selected airfoils chromosomes are modified.
5. A new generation individuals are formed as a combination of offspring population individuals and selected high scored individuals from previous population. The airfoils obtained in step 4 and airfoils having higher  $C_l/C_d$  ratio kept for the next objective function evaluation.
6. The fitness values are calculated for the individuals of new generation. Again for every airfoil obtained at the end of the step 5, the  $C_l/C_d$  ratio is computed.
7. Until the desired performance is achieved, this evolution of generations continues. Since the target is to reach maximum  $C_l/C_d$  ratio, the optimization is carried on till the predefined fitness function tolerance is achieved.

In this study, GA is performed by optimizing the parameters which are used to define a selected airfoil CST weighting coefficients, PARSEC geometric coefficients and selected wind turbine blade optimization parameters.



## CHAPTER 3

### AIRFOIL DESIGN

#### 3.1. Validation Studies

In this validation studies section, predefined airfoil geometry fitting validation studies are presented. The validation of CST and PARSEC fittings for a known airfoil geometry is investigated. The developed MATLAB code for CST fitting, AirfoilCST, and the developed MATLAB code for PARSEC fitting, AirfoilPARSEC, are validated for different airfoils.

##### 3.1.1. CST Method Fitting Validation

In the first instance, RAE 2822 airfoil is selected as first validation case. Figure 3.1 shows the 5<sup>th</sup> order CST fitting results of AirfoilCST, for the RAE 2822 airfoil. The geometry original coordinates of the RAE 2822 airfoil is given in red, the geometry obtained from AirfoilCST is given by the blue. It is clearly observed that both upper side and lower side of the airfoil can be followed very smoothly by AirfoilCST.

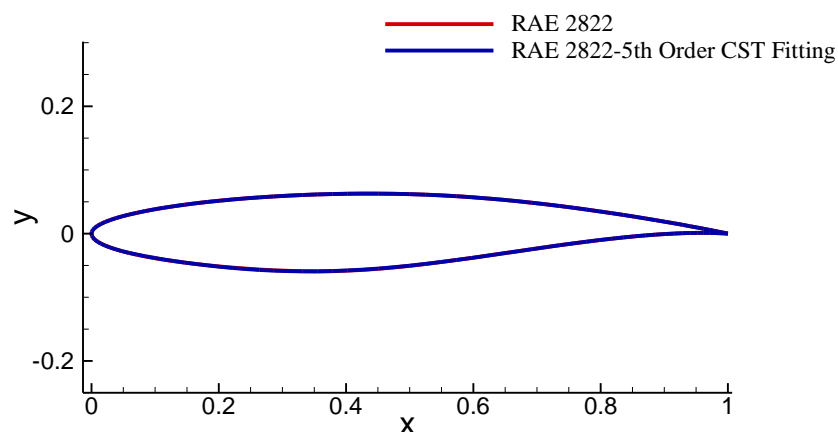


Figure 3.1. 5<sup>th</sup> Order CST Fitting with AirfoilCST for RAE 2822 Airfoil

### 3.1.1.1. Investigation of the CST Parameterization Order Effect

In airfoil design and optimization studies, it is desired to minimize the number of design parameters. Because, optimization efficiency is directly related the number of design parameters. On the other hand, the number of design parameters should be high enough to represent airfoil geometry at high resolution. In CST method, the number of design parameters is depend on the order of CST parameterization. In this section, the main intention is to investigate the effect of the CST fitting order on airfoil geometry. For this purpose, two different, 5<sup>th</sup> and 9<sup>th</sup> order, AirfoilCST fitting results have analyzed and compared. The validation case baseline airfoil geometry is selected as S809 airfoil which is 21% thick, laminar flow airfoil, designed for HAWT applications by NREL [57]. This airfoil is used in NREL Phase III and Phase VI reference wind turbine rotors which will be discussed in Section 4.2 BEM Analysis Validation in detail.

In Figure 3.2, 5<sup>th</sup> order CST fitting results performed with AirfoilCST for S809 airfoil is presented. The original coordinates of the S809 airfoil is given in red, the geometry obtained from AirfoilCST is given in blue. In Figure 3.3, upper and lower curve residuals for 5<sup>th</sup> order AirfoilCST S809 airfoil fitting results are shown. The location of maximum residuals for both lower and upper curves is observed between 0.4-0.6 x coordinate locations. The maximum residual value is found as 2.5% for upper curve and 2.1% for lower curve.

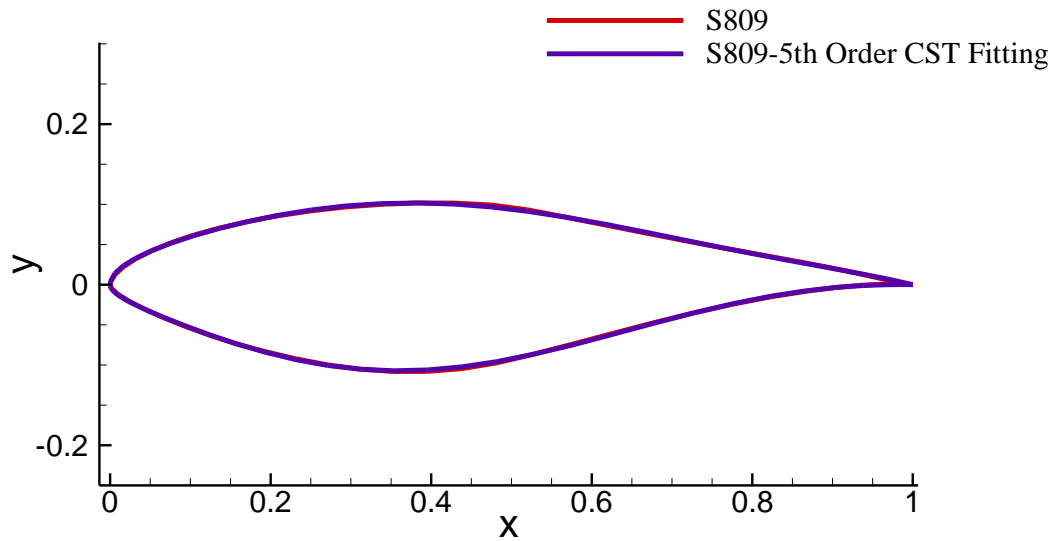


Figure 3.2. 5<sup>th</sup> Order CST Fitting with AirfoilCST for S809 Airfoil

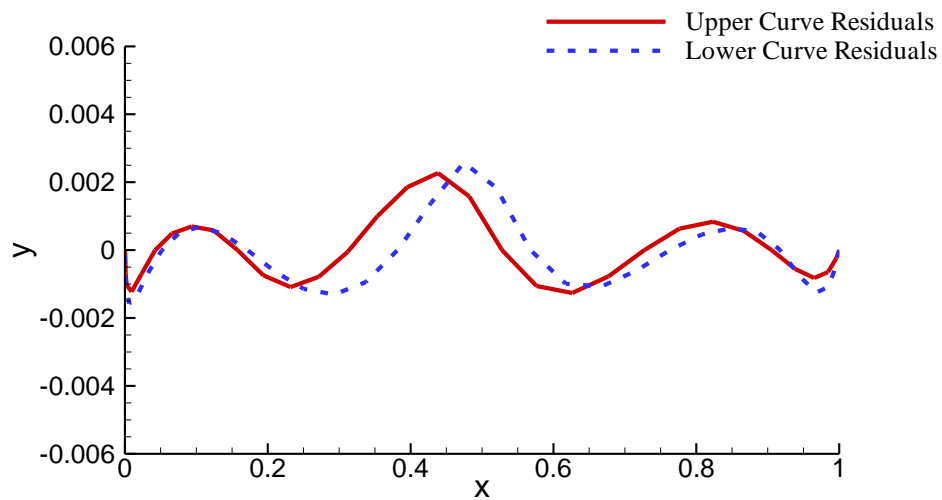


Figure 3.3. Upper and Lower Curve Residuals for 5<sup>th</sup> Order AirfoilCST S809 Airfoil Fitting Results

In Figure 3.4, 9<sup>th</sup> order CST fitting results performed with AirfoilCST for S809 airfoil is presented. The original coordinates of the S809 airfoil is given in red, the geometry obtained from AirfoilCST is given in blue. In Figure 3.5, upper and lower curve residuals for 9<sup>th</sup> order AirfoilCST S809 airfoil fitting results are shown. The location

of maximum residuals for both lower and upper curves is observed again between 0.4-0.6 x coordinate locations. The maximum residual value is found as 0.8% for upper curve and 0.6% for lower curve.

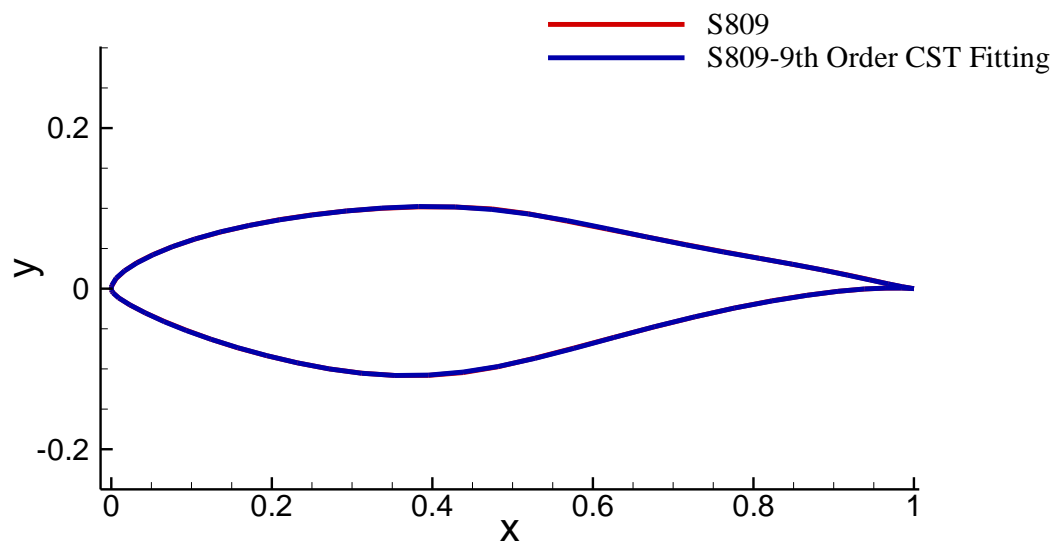


Figure 3.4. 9<sup>th</sup> Order CST Fitting with AirfoilCST for S809 Airfoil

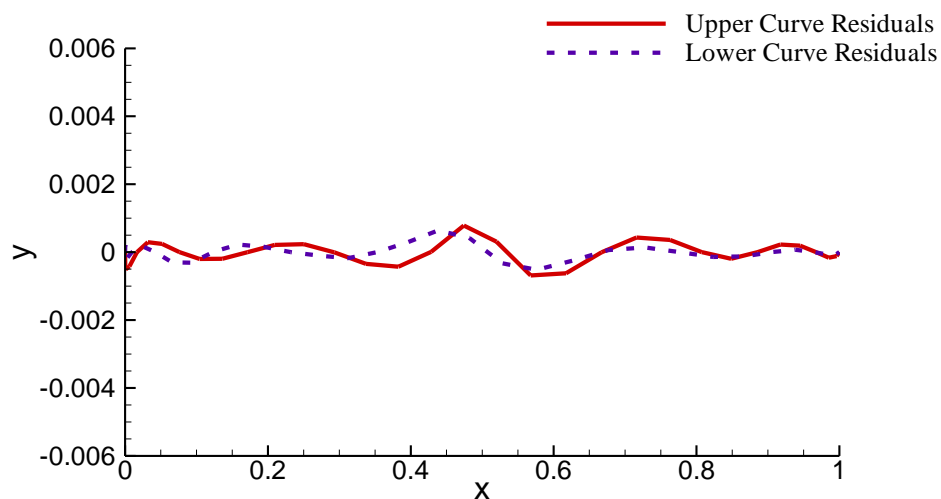


Figure 3.5. Upper and Lower Curve Residuals for 9<sup>th</sup> Order AirfoilCST S809 Airfoil Fitting Results

In conclusion, the residuals are decreased nearly by 30% for both upper and lower curves when CST fitting order is increased from 5 to 9. On the other hand, this rise in the CST fitting order caused a jump in the number of design variables more than 66%. Using the 5<sup>th</sup> degree CST fitting is found sufficient to represent airfoil geometry at high resolution. Moreover, in the scope of this study, it is desired to compare the performance of CST and PARSEC representation methods. To be able to reach this design environment, since the number of PARSEC geometric parameters are fixed to 12 by definition, total number of CST design coefficients are made equal to 12. Remembering that n<sup>th</sup> order CST parameterization is yielding n+1 coefficients. Consequently, 5<sup>th</sup> degree CST fitting parameterization is selected as optimization parameterization order.

#### **3.1.1.2. Investigation of CST Weighting Coefficients and Airfoil Geometry Relations**

It is previously mentioned that CST weighting coefficients are directly related to specific shape of the airfoil. In order to observe these relations, some test cases are performed.

First of all, the relation between leading edge nose radius and CST weighting coefficients is investigated. Remembering that the first CST weighting coefficient is directly related to leading edge nose radius, two airfoils are created to observe new airfoil geometries by increasing and decreasing this term arbitrarily. In Figure 3.6, on RAE 2822 airfoil, varying leading edge nose radius term effect is demonstrated. Corresponding CST weighting coefficients are tabulated in Table 3.1.

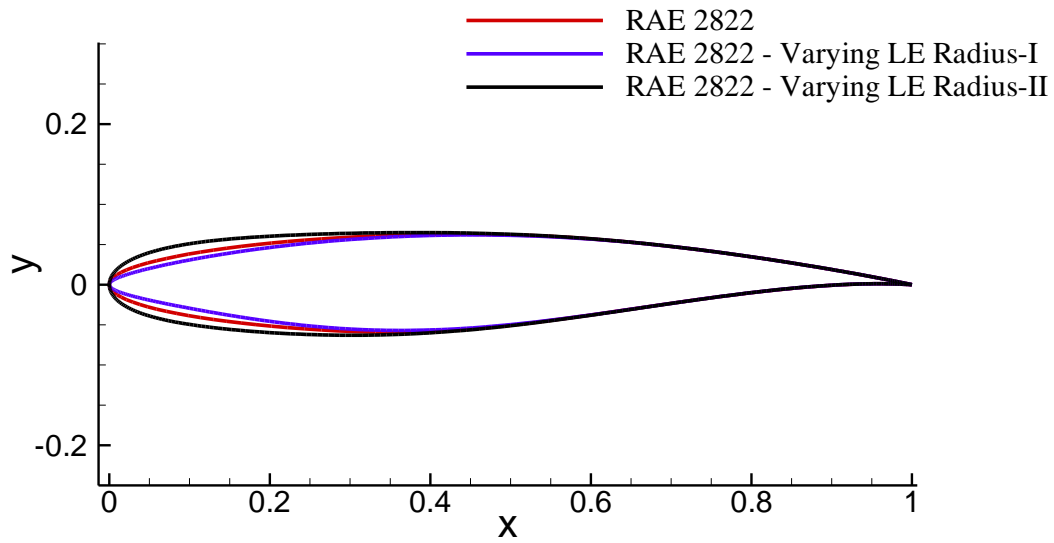


Figure 3.6. Leading Edge Nose Radius CST Term Effect on RAE 2822 Airfoil Geometry

Table 3.1. CST Weighting Coefficients of RAE 2822 Airfoil Varying Leading Edge Nose Radius

Airfoil	5 <sup>th</sup> Order Lower Surface CST Coefficients					
RAE 2822	-0,133	-0,116	-0,233	-0,109	-0,096	0,058
RAE 2822 - Varying LE Radius I	-0,080	-0,116	-0,233	-0,109	-0,096	0,058
RAE 2822 - Varying LE Radius II	-0,200	-0,116	-0,233	-0,109	-0,096	0,058

Airfoil	5 <sup>th</sup> Order Upper Surface CST Coefficients					
RAE 2822	0,125	0,147	0,150	0,215	0,178	0,209
RAE 2822 - Varying LE Radius I	0,080	0,147	0,150	0,215	0,178	0,209
RAE 2822 - Varying LE Radius II	0,200	0,147	0,150	0,215	0,178	0,209

Secondly, the relation between boattail angle and CST weighting coefficients is investigated. Remembering that the last CST weighting coefficient is directly related to boattail angle, two airfoils are created to observe new airfoil geometries by by changing this term arbitrarily. In Figure 3.7, on RAE 2822 airfoil, varying boattail angle term effect is demonstrated. Corresponding CST weighting coefficients are tabulated in Table 3.2.

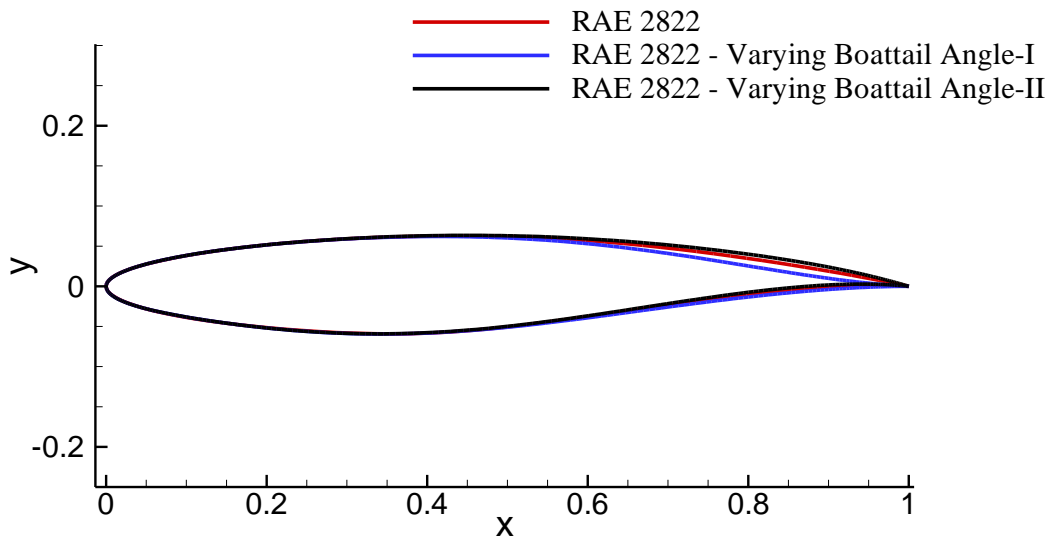


Figure 3.7. Boattail Angle CST Term Effect on RAE 2822 Airfoil Geometry

Table 3.2. CST Weighting Coefficients of RAE 2822 Airfoil Varying Boattail Angle

Airfoil	5 <sup>th</sup> Order Lower Surface CST Coefficients					
RAE 2822	-0,133	-0,116	-0,233	-0,109	-0,096	0,058
RAE 2822 - Varying Bottail Angle I	-0,133	-0,116	-0,233	-0,109	-0,096	0,000
RAE 2822 - Varying Bottail Angle II	-0,133	-0,116	-0,233	-0,109	-0,096	0,100

Airfoil	5 <sup>th</sup> Order Upper Surface CST Coefficients					
RAE 2822	0,125	0,147	0,150	0,215	0,178	0,209
RAE 2822 - Varying Bottail Angle I	0,125	0,147	0,150	0,215	0,178	0,050
RAE 2822 - Varying Bottail Angle II	0,125	0,147	0,150	0,215	0,178	0,300

Finally, the relation between thickness and CST weighting coefficients is investigated. Remembering that the middle CST weighting coefficients are directly related to thickness distribution, two airfoils are created to observe new airfoil geometries by modifying these terms arbitrarily. In Figure 3.8, varying thickness distribution effect is demonstrated on RAE 2822 airfoil geometry. Corresponding CST weighting coefficients are tabulated in Table 3.3.

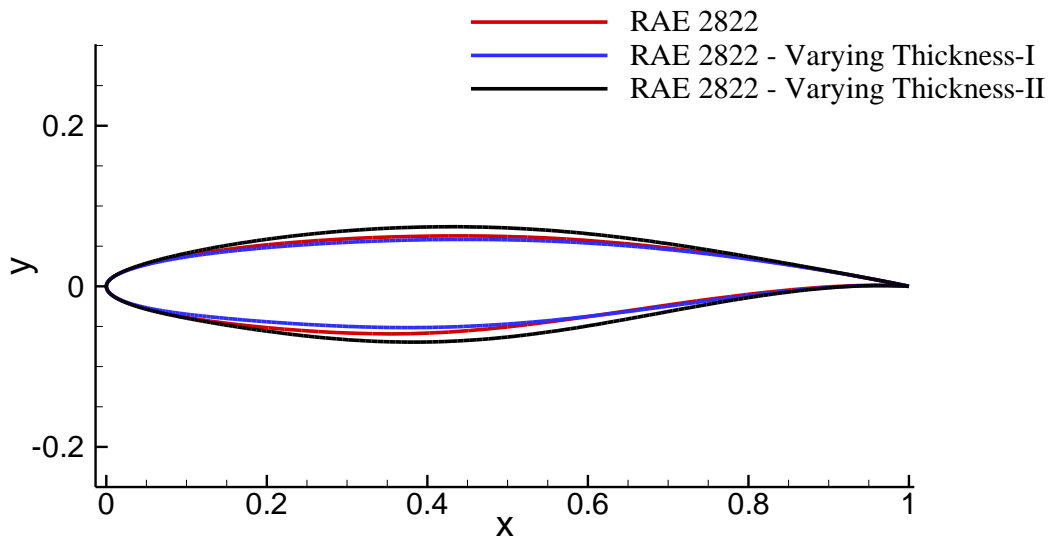


Figure 3.8. Thickness Distribution CST Term Effect on RAE 2822 Airfoil Geometry

Table 3.3. CST Weighting Coefficients of RAE 2822 Airfoil Varying Thickness Distribution

<b>Airfoil</b>	<b>5<sup>th</sup> Order Lower Surface CST Coefficients</b>					
RAE 2822	-0,133	-0,116	-0,233	-0,109	-0,096	0,058
RAE 2822 - Varying Thickness I	-0,133	-0,100	-0,130	-0,190	-0,100	0,058
RAE 2822 - Varying Thickness II	-0,133	-0,130	-0,190	-0,260	-0,130	0,058

<b>Airfoil</b>	<b>5<sup>th</sup> Order Upper Surface CST Coefficients</b>					
RAE 2822	0,125	0,147	0,150	0,215	0,178	0,209
RAE 2822 - Varying Thickness I	0,125	0,130	0,140	0,160	0,200	0,209
RAE 2822 - Varying Thickness II	0,125	0,160	0,190	0,210	0,250	0,209

### 3.1.2. PARSEC Method Fitting Validation

For PARSEC method validation purposes, S809 profile is selected as the reference airfoil. To begin with, PARSEC geometric coefficients are calculated from the airfoil coordinates. Calculated PARSEC geometric coefficients for S809 airfoil are listed in Table 3.4. Then, these coefficients are used to compute PARSEC weighting coefficient matrices for upper and lower surfaces. Figure 3.9 shows the S809 airfoil PARSEC fitting results of AirfoilPARSEC. The original coordinates of the S809 airfoil is given in red, the geometry obtained from AirfoilPARSEC is given in blue. In Figure 3.10, upper and lower curve residuals for AirfoilPARSEC S809 airfoil fitting results are shown. For both lower and upper curves, it is observed that the high residual regions are intensified at the transition regions, e.g. transition from leading edge radius region to maximum thickness location region. The maximum residual value is found as 3.8% for upper curve and 3.1% for lower curve. This results are relatively high compared to the 5<sup>th</sup> order AirfoilCST S809 airfoil fitting results.

Table 3.4 PARSEC Geometric Coefficients for S809 Airfoil

<b>p<sub>1</sub></b>	0,012
<b>p<sub>2</sub></b>	0,383
<b>p<sub>3</sub></b>	0,102
<b>p<sub>4</sub></b>	-0,923
<b>p<sub>5</sub></b>	0,353
<b>p<sub>6</sub></b>	-0,108
<b>p<sub>7</sub></b>	1,711
<b>p<sub>8</sub></b>	0
<b>p<sub>9</sub></b>	0
<b>p<sub>10</sub></b>	3,014
<b>p<sub>11</sub></b>	-0,075
<b>p<sub>12</sub></b>	0,007

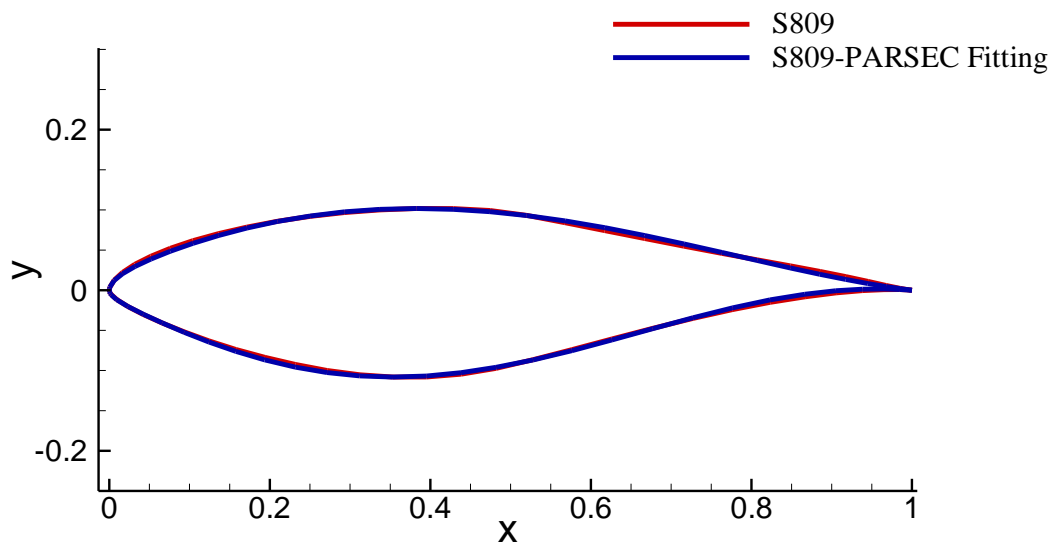


Figure 3.9. PARSEC Fitting with AirfoilPARSEC for S809 Airfoil

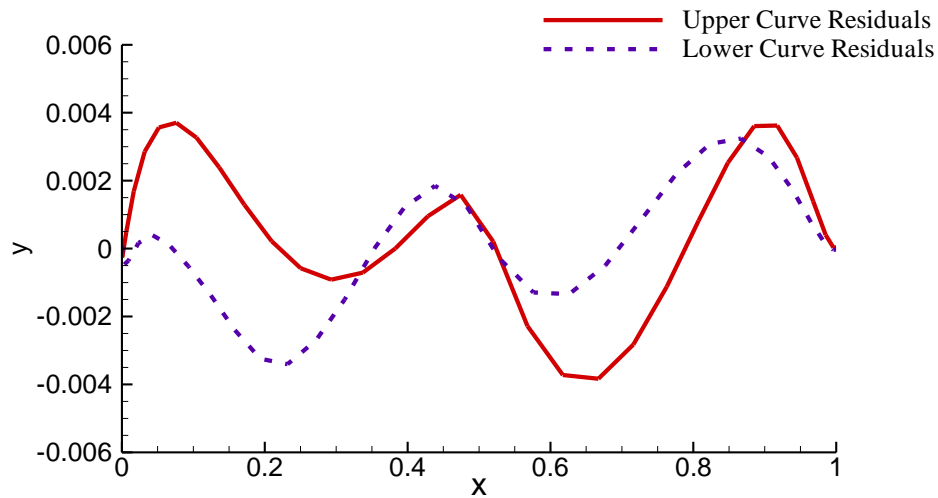


Figure 3.10. Upper and Lower Curve Residuals for Airfoil PARSEC S809 Airfoil Fitting Results

### 3.2. Airfoil Optimization Studies

Due to high bending forces acting on the blade root, structural requirements become crucial rather than aerodynamic concerns. Consequently, airfoil thickness at this region is high. On the other hand, relative wind speed increases drastically from hub to tip making blade tip region very significant from aerodynamic point of view. To be able to extract more energy from free steam, the design of the airfoil at the blade tip should be more aerodynamically efficient. This makes airfoil geometry at the tip more slender. Based on this significance of thickness in airfoil design, investigation of thickness distribution effect on airfoil performance is selected as airfoil optimization research objective in this thesis study.

The main purpose is to optimize new airfoils having different thickness by using CST and PARSEC airfoil representation methods. The optimization objective target is designated as the maximization of  $C_l/C_d$  ratio for a prespecified, fixed flow condition. In Figure 3.12, airfoil geometry optimization flowchart is shown. First of all, the CST or PARSEC weighing coefficients are assigned as design variables and the geometry of first population are generated. After that, XFOIL is called and the executed for input flow conditions. Then, the output files of XFOIL are read and  $C_l/C_d$  ratio are calculated

for each individual. MATLAB GA toolbox is used to perform optimization studies. It is only capable of making minimization so the objective function is introduced as  $-C_l/C_d$  ratio. Based on fitness function results, optimization termination criteria are checked. If the termination criteria are satisfied, the loop is ended. Otherwise, selection, crossover and mutation operations are performed and the CST or PARSEC weighing coefficients are modified and a new generation is formed. The same process is repeated until the termination criteria are satisfied.

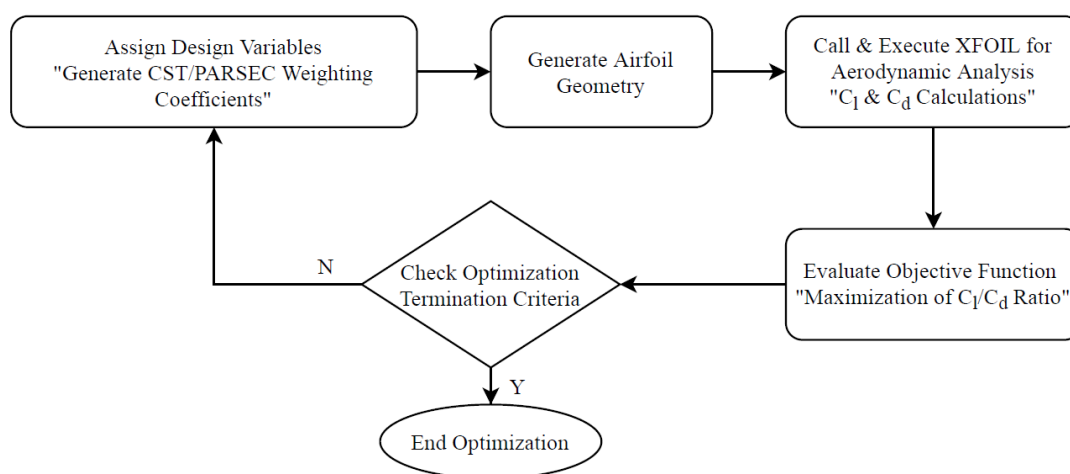


Figure 3.11. Airfoil Geometry Optimization Flowchart

In this study, S809 airfoil is selected as the baseline airfoil since it is used in NREL Phase III and NREL Phase VI wind turbine rotors which are chosen as the blade validation case rotors discussed in Chapter 5. Four case studies are performed having different thickness distributions by altering the thickness related CST or PARSEC weighing coefficients.

### 3.2.1. CST Optimization Results

Optimization results of airfoil profiles defined by CST method are presented and discussed in this part. For selected baseline airfoils, 5<sup>th</sup> order CST coefficients are determined. Out of total 12 CST variables, 6 CST weighing coefficients, 3 of them for upper curve and 3 of them for lower curve, affecting the airfoil thickness are selected as optimization parameters.

### 3.2.1.1. S809 Airfoil Geometry Optimizations with CST Parameterization

In this section, two case studies are performed and analyzed. For each case study a new baseline is formed from S809 primary airfoil. In order to create new baseline airfoils, airfoil thickness related CST weighing coefficients of S809 airfoil are modified by %20. In Case I, a thinner baseline airfoil is designated by decreasing these coefficients by %20. Then the optimization is done by manipulating the CST weighing coefficients of this thinner baseline airfoil. In Case II, a thicker baseline airfoil is designated by increasing these coefficients by %20. Then the optimization is done by manipulating the CST weighing coefficients of this thicker baseline airfoil. The geometries of thicker and thinner baseline profiles to S809 airfoil is given in Figure 3.12. Corresponding CST weighing coefficients for baseline airfoil geometries are given in Table 3.5.

Table 3.5 CST Weighing Coefficients for S809 Airfoil Baselines

<b>Airfoil</b>	<b>5<sup>th</sup> Order Lower Surface CST Coefficients</b>					
Thinner Baseline	-0,127	-0,200	-0,322	-0,203	-0,087	0,017
S809	-0,127	-0,250	-0,403	-0,254	-0,087	0,017
Thicker Baseline	-0,127	-0,300	-0,484	-0,304	-0,087	0,017

<b>Airfoil</b>	<b>5<sup>th</sup> Order Upper Surface CST Coefficients</b>					
Thinner Baseline	0,182	0,186	0,253	0,244	0,139	0,242
S809	0,182	0,233	0,317	0,305	0,139	0,242
Thicker Baseline	0,182	0,280	0,380	0,367	0,139	0,242

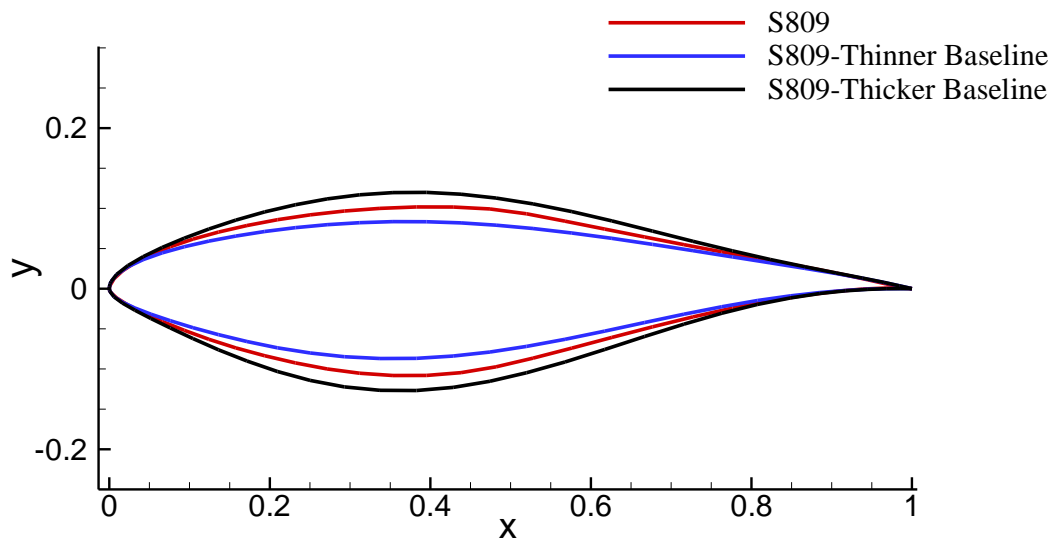
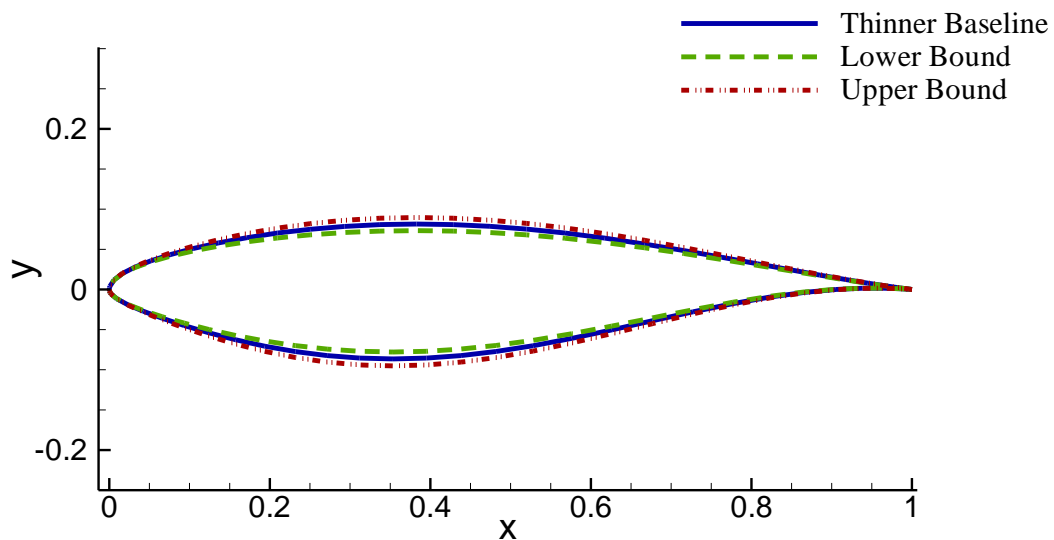


Figure 3.12. The Comparison of Thinner and Thicker Baseline Airfoil Geometries  
Generated with CST Parameterization to S809 Profile

The airfoil geometry optimization bounds are defined by increasing and decreasing CST coefficients of the baseline airfoils by 10%. In Figure 3.13, the upper and lower bounds of thinner and thicker optimization baselines are given.



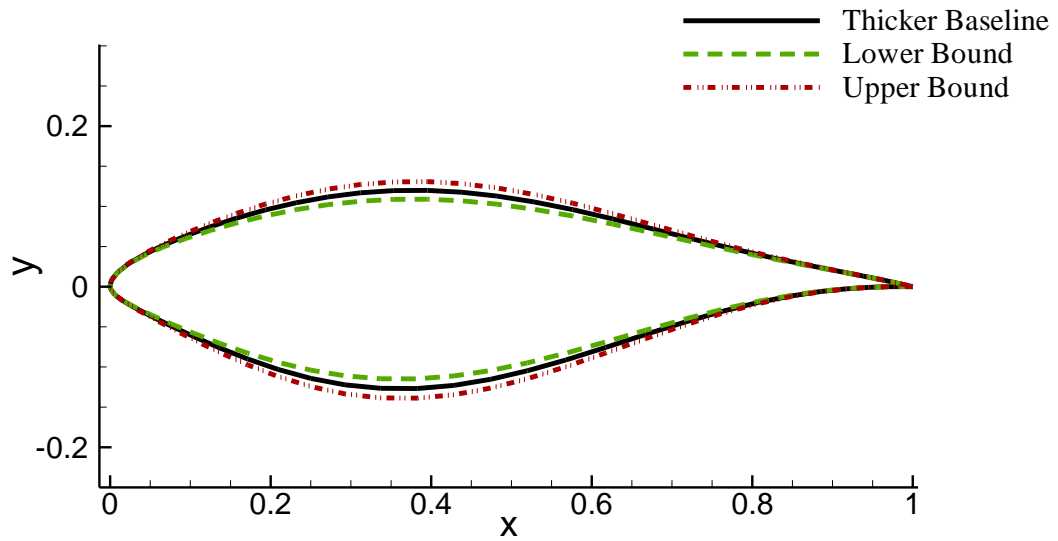


Figure 3.13. The Upper and Lower Bounds of Thinner (upper) and Thicker (lower) Optimization Baseline Geometries

### 3.2.1.2. Case I - Optimization of Thinner Baseline Airfoil with CST

In Case I - optimization of thinner baseline airfoil with CST, the optimization flow conditions is set to fixed values as  $5^\circ$  AoA and  $5 \times 10^6$  *Re*. Compressibility effects are not into taken into account. The genetic algorithm optimization parameters are summarized in Table 3.6. Best and mean fitness values versus generation number graph is provided in Figure 3.14. It can be concluded that optimization quickly converges to the best value nearly after 20<sup>th</sup> generations.

Table 3.6. The Initial Genetic Algorithm Optimization Parameters for Case I

Optimization Variables	
Population Size	100
Minimum Number of Generations	201
Function Tolerance	1e-1

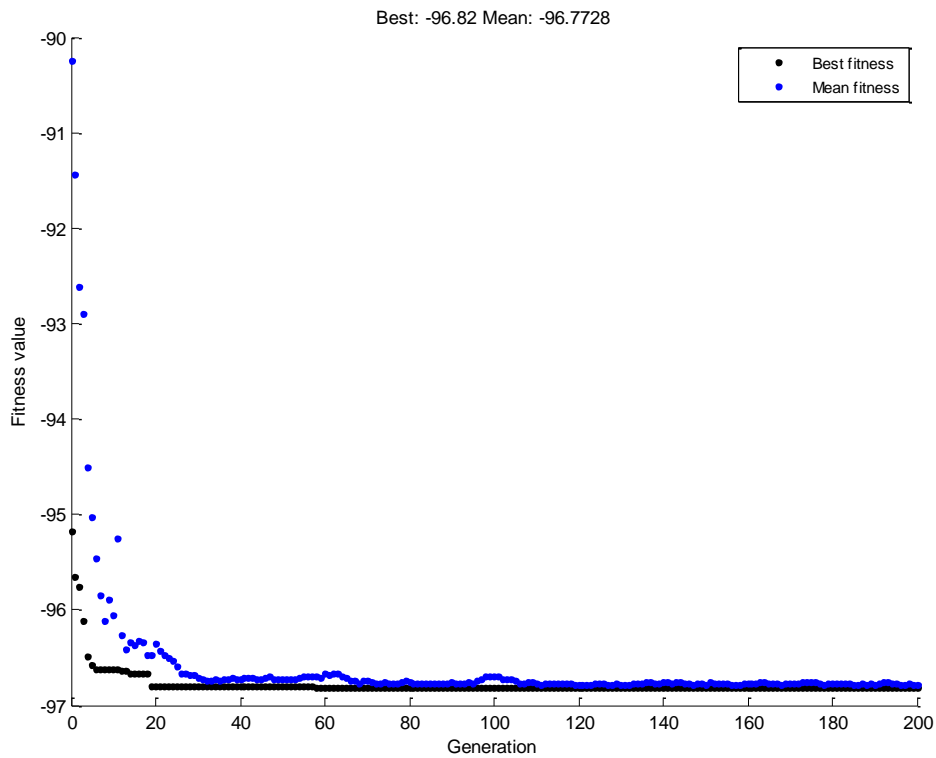


Figure 3.14. The Fitness Value vs Generation Number Graph for Case I with Initial GA Optimization Parameters

Based on this convergence trend, minimum number of generations set to 51 and population size is dropped to 75, for forthcoming optimization cases. Revised optimization parameters are shown in Table 3.7 and the best and mean fitness values versus generation number graph is provided in Figure 3.15. The average distance between individuals versus generation number graph for Case I is given in Figure 3.16.

Table 3.7. The Revised Genetic Algorithm Optimization Parameters for Case I

<b>Optimization Variables</b>	
Population Size	75
Minimum Number of Generations	51
Function Tolerance	1e-1

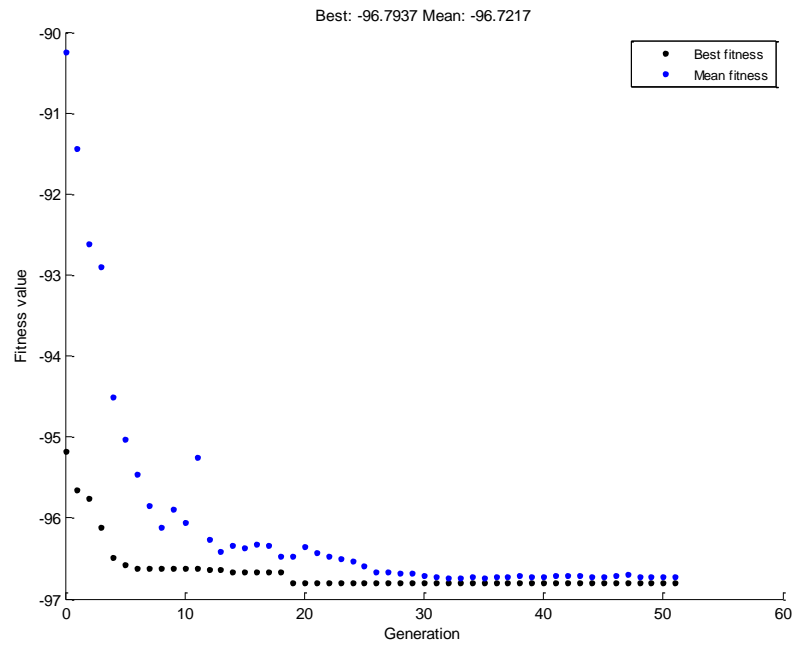


Figure 3.15. The Best and Mean Fitness Values vs Generation Graph for Case I

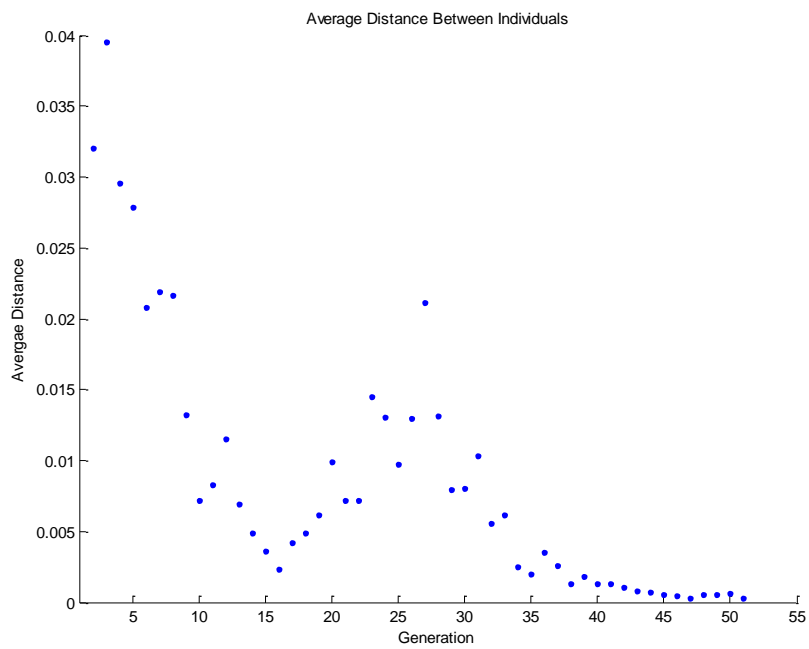


Figure 3.16. The Average Distance between Individuals vs Generation Number Graph for Case I

The objective function values for this case is presented in Table 3.8. There difference is lower than 0,03% between initial and revised optimization results. Therefore, it is deduced that the revised optimization parameters are good enough for perform optimization of airfoil problem represented with thickness related 6 CST parameters. Moreover, compared to the thinner baseline airfoil, revised optimized airfoil  $C_l/C_d$  performance is improved approximately 7.7%. The  $C_l/C_d$  ratio comparison of the optimized airfoil geometry at Case I and the thinner baseline geometry is given in Figure 3.18. For all AoA values, the  $C_l/C_d$  curve of optimized airfoil shows better performance than the thinner baseline geometry.

Table 3.8. The Objective Function Results for Case I

<b>Thinner Baseline <math>C_l/C_d</math> Optimization Results</b>	
Thinner Baseline	89,8
Lower Bound	91,5
Upper Bound	88,6
Initial Optimization Results	96,8
Revised Optimization Results	96,8

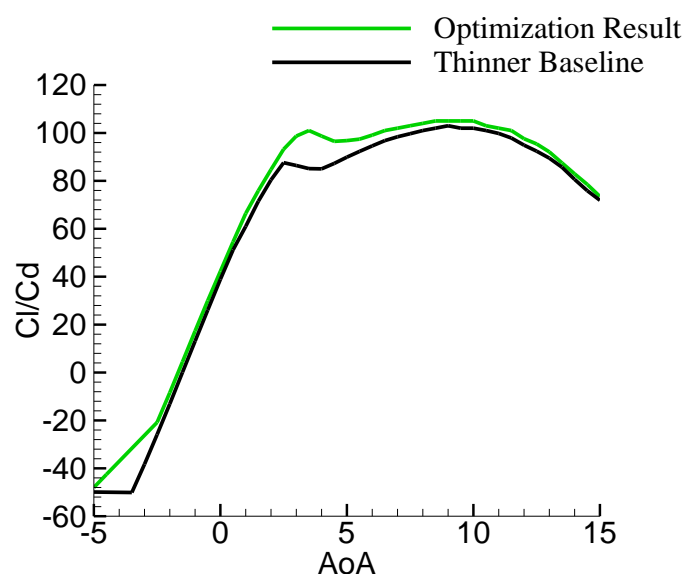


Figure 3.17. The  $C_l/C_d$  Ratio Comparisons for Case I

The initial and revised optimized airfoil, the thinner baseline and S809 airfoil geometries are drawn comparatively in Figure 3.18. In this graph, symbol shapes for optimization results are used only for illustration purposes. It can be observed that the initial and revised optimized airfoil geometries are nearly overlapped. In Table 3.9, CST weighing coefficients for optimized airfoil geometry for thinner baseline are given.

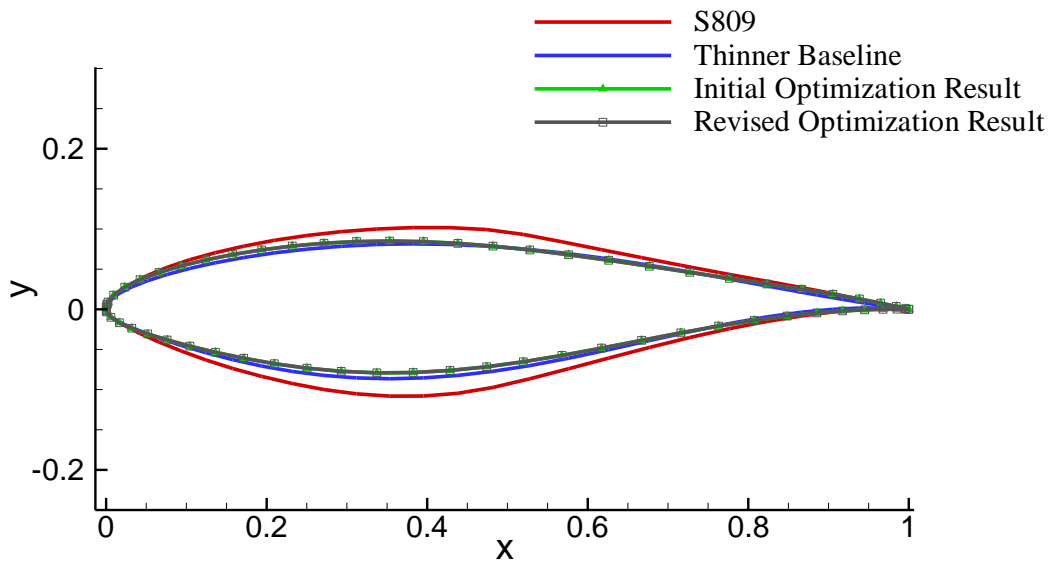


Figure 3.18. The Airfoil Geometry Comparisons for Case I

Table 3.9. CST Weighing Coefficients for Thinner Optimized Baseline Airfoil

Thinner Optimized Results	5 <sup>th</sup> Order Lower Surface CST Coefficients		
Initial Optimization Result	-0,1801351	-0,2906584	-0,1826216
Revised Optimization Result	-0,1801351	-0,2906583	-0,1826216

Thinner Optimized Results	5 <sup>th</sup> Order Upper Surface CST Coefficients		
Initial Optimization Result	0,2049913	0,2613371	0,2210565
Revised Optimization Result	0,2048166	0,2612324	0,2209211

### 3.2.1.3. Case II - Optimization of Thicker Baseline Airfoil with CST

In Case II - optimization of thicker baseline airfoil with CST, the optimization flow conditions is set to fixed values as  $5^0$  AoA and  $1 \times 10^6$  *Re*. Compressibility effects are not into taken into account. The optimization parameters are shown in Table 3.10. Best and mean fitness values versus generation number graph is provided in Figure 3.19. The average distance between individuals versus generation number graph for Case II is given in Figure 3.20.

Table 3.10. The Genetic Algorithm Optimization Parameters for Case II

Optimization Variables	
Population Size	100
Minimum Number of Generations	101
Function Tolerance	1e-1

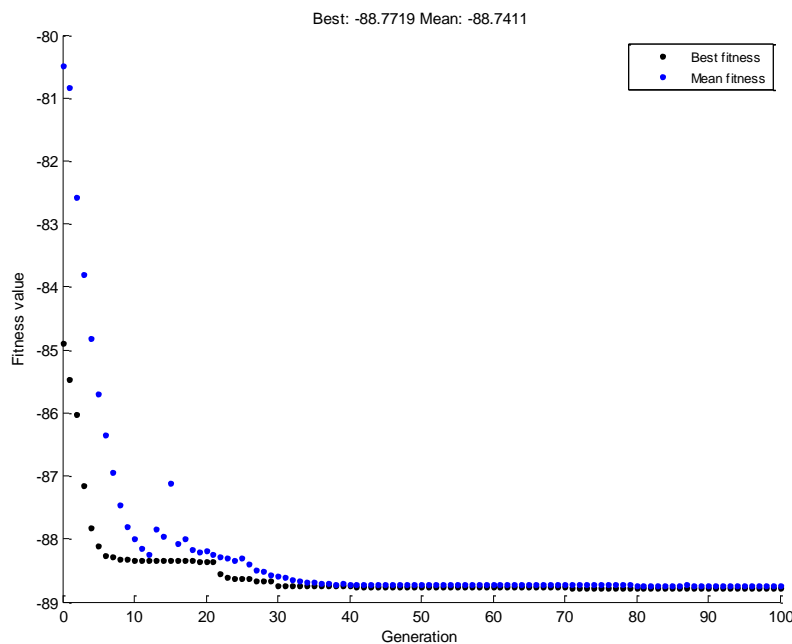


Figure 3.19. The Best and Mean Fitness Values vs Generation Graph for Case II

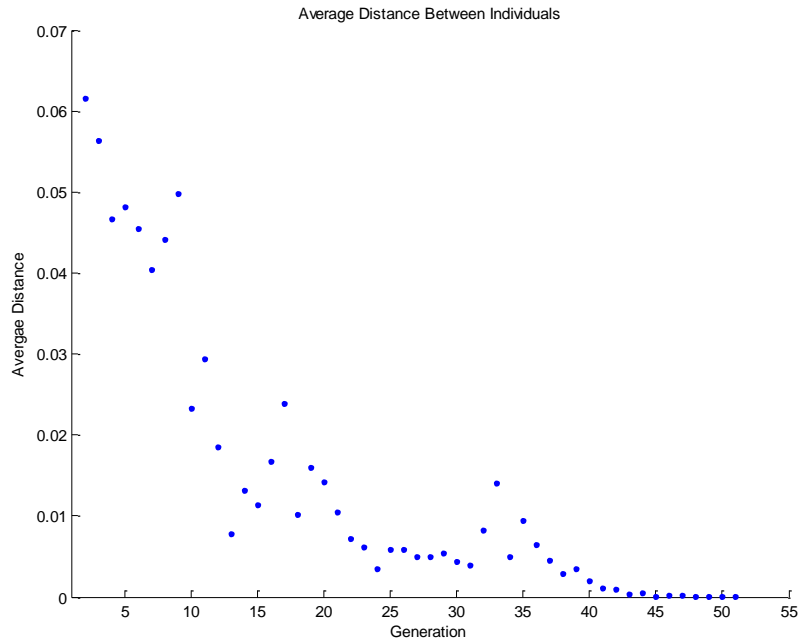


Figure 3.20. The Average Distance between Individuals vs Generation Number Graph for Case II

The objective function values for this case is presented in Table 3.11. The performance of optimized airfoil in Case II, is higher nearly 10.2% than thicker baseline airfoil. The  $C_l/C_d$  ratio comparison of the optimized airfoil geometry at Case II and the thicker baseline geometry is given in Figure 3.21. Between  $-3^\circ$  and  $6^\circ$  of AoA, a shift in  $C_l/C_d$  curve is observed with optimized airfoil geometry. Then between  $6^\circ$  and  $8^\circ$  of AoA, thicker baseline performance is seems better than optimized airfoil. For the AoA values higher than  $8^\circ$ , the optimized airfoil geometry has higher  $C_l/C_d$  ratios.

Table 3.11. The Objective Function Results for Case II

<b>Thicker Baseline <math>C_l/C_d</math> Optimization Results</b>	
Thicker Baseline	80,6
Lower Bound	85,5
Upper Bound	75,4
Optimization Results	88,8

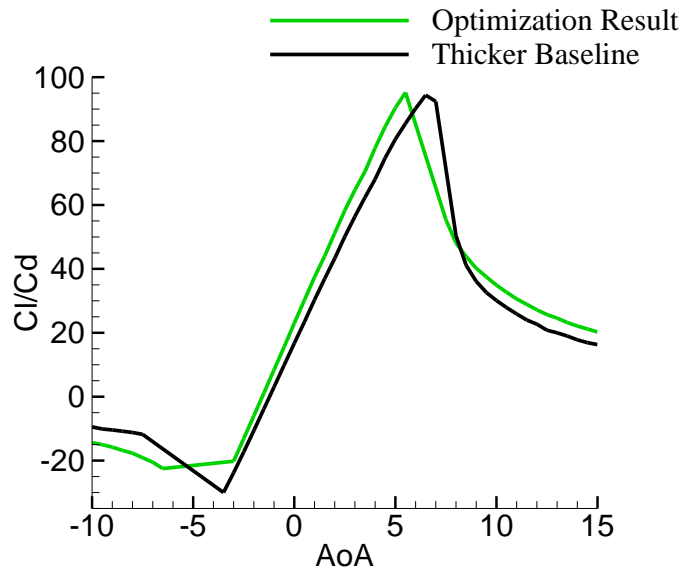


Figure 3.21. The  $C_l/C_d$  Ratio Comparisons for Case II

The optimized airfoil geometry, the thicker baseline geometry and S809 airfoil geometry are illustrated comparatively in Figure 3.22. In Table 3.12, CST weighing coefficients for optimized airfoil geometry for root section are given.

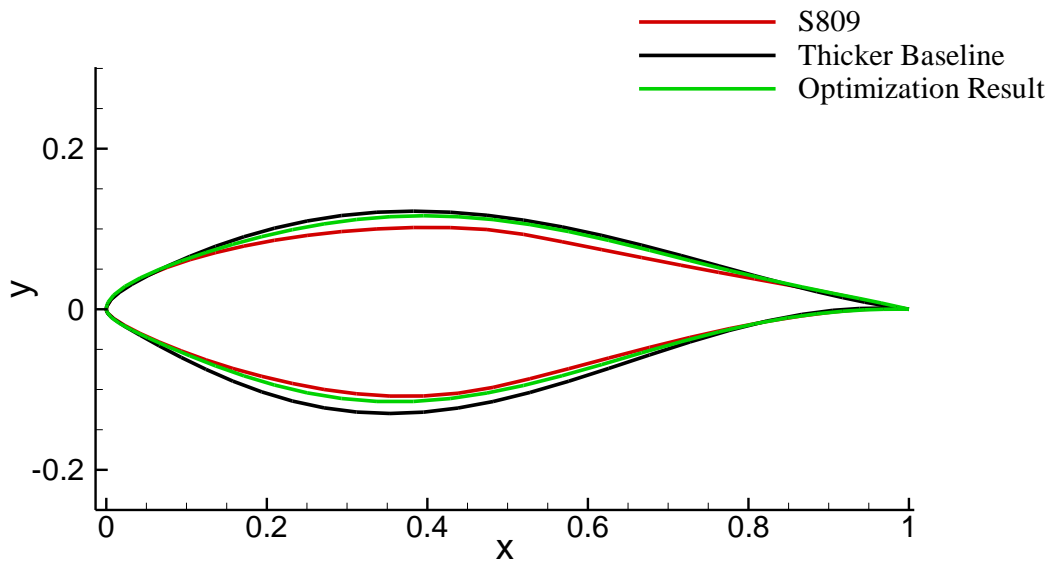


Figure 3.22. The Airfoil Geometry Comparisons for Case II

Table 3.12. CST Weighing Coefficients for Thicker Optimized Baseline Airfoil

<b>Thicker Optimized</b>	<b>5<sup>th</sup> Order Lower Surface CST Coefficients</b>		
Optimization Result	-0,271	-0,435	-0,274

<b>Thicker Optimized</b>	<b>5<sup>th</sup> Order Upper Surface CST Coefficients</b>		
Optimization Result	0,254	0,350	0,402

### **3.2.2. PARSEC Optimization Results**

Optimization results of airfoil profiles defined by PARSEC method are presented and discussed in this part. For selected baseline airfoils, airfoil thickness related parameters are selected as 4 PARSEC optimization parameters, 2 of them for upper curve and 2 of them for lower curve. These parameters are the maximum thickness y location for upper curve, the upper crest curvature, the maximum thickness y location for lower curve and the lower crest curvature.

#### **3.2.2.1. S809 Airfoil Geometry Optimizations with PARSEC Parameterization**

In this section, two case studies are performed and analyzed. For each case study a new baseline is formed from S809 primary airfoil. In order to create new baseline airfoils, airfoil thickness related PARSEC parameters of S809 airfoil are modified by %20. In Case III, a thinner baseline airfoil is designated by decreasing these coefficients by %20. Then the optimization is done by manipulating the PARSEC parameters of this thinner baseline airfoil. In Case IV, a thicker baseline airfoil is designated by increasing these coefficients by %20. Then the optimization is done by manipulating the PARSEC parameters of this thicker baseline airfoil. The thicker and thinner baseline profiles generated by PARSEC method are drawn in Figure 3.23. Corresponding PARSEC parameters are provided in Table 3.13.

Table 3.13 PARSEC Geometric Parameters for S809 Airfoil Baselines

Airfoil	$y_{upper}$	$y_{xx,upper}$	$y_{lower}$	$y_{xx,lower}$
S809 - Thinner Baseline %20	0,081	-0,739	-0,087	1,369
S809 - Baseline	0,102	-0,923	-0,108	1,711
S809 - Thicker Baseline %20	0,122	-1,108	-0,130	2,053

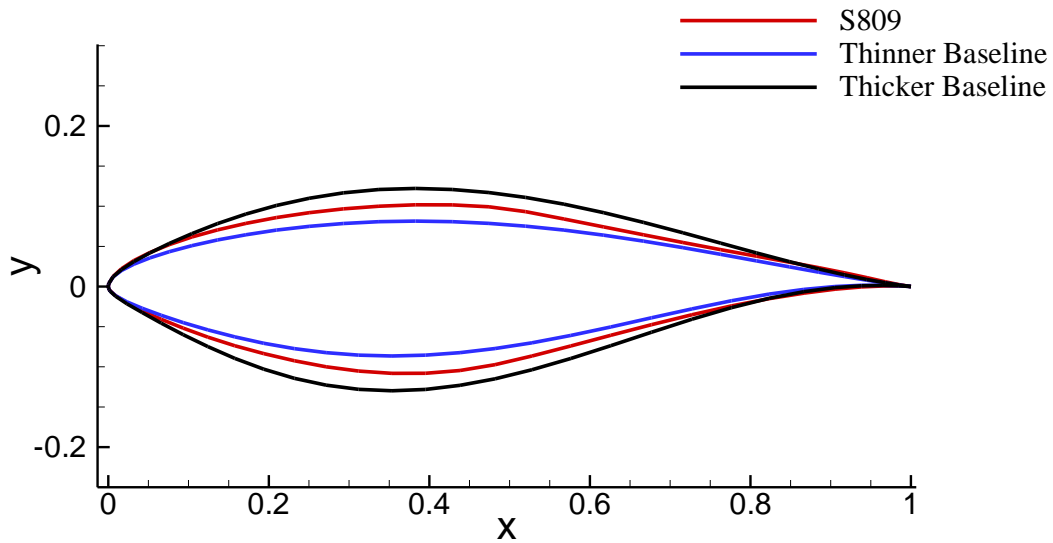


Figure 3.23. The Comparison of Thinner and Thicker Baseline Airfoil Geometries  
Generated with PARSEC Parameterization to S809 Profile

The airfoil geometry optimization bounds are defined by increasing and decreasing PARSEC parameters of the baseline airfoils by 10%. In Figure 3.24, the upper and lower bounds of thinner and thicker optimization baselines are given.

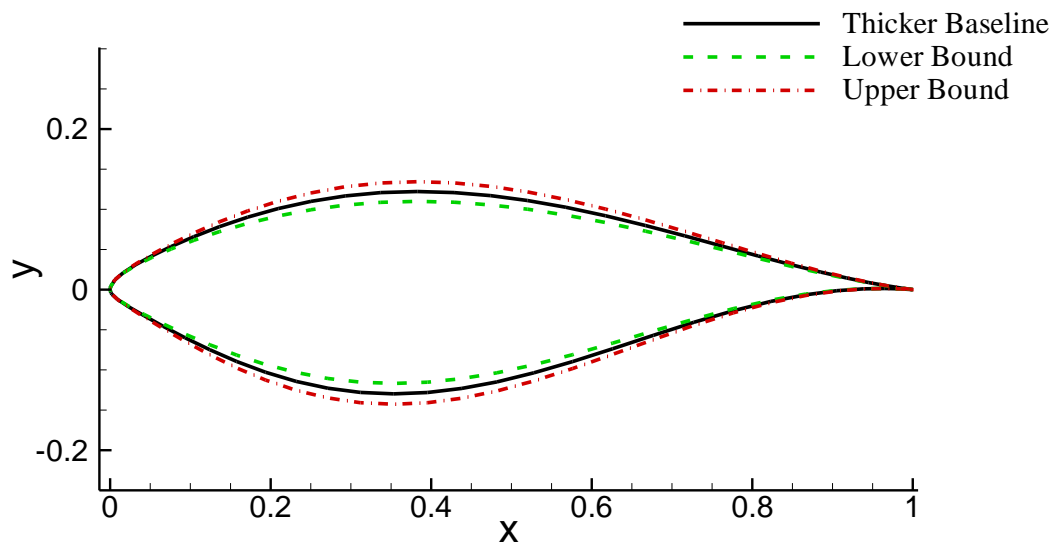
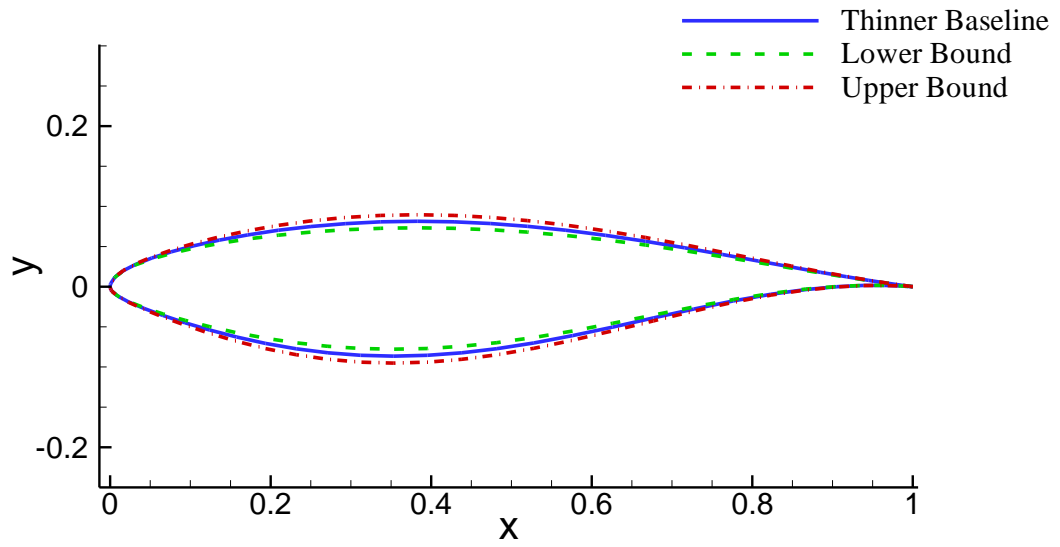


Figure 3.24. The Upper and Lower Bounds of Thinner (upper) and Thicker (lower) Optimization Baseline Geometries

### 3.2.2.2. Case III - Optimization of Thinner Baseline Airfoil with PARSEC

In Case III - optimization of thinner baseline airfoil with PARSEC, the optimization flow conditions is set to fixed values as  $5^\circ$  AoA and  $5 \times 10^6 Re$ . Compressibility effects

are not into taken into account. The genetic algorithm optimization parameters given in Table 3.7 are also used in this case. Best and mean fitness values versus generation number graph is provided in Figure 3.25. The average distance between individuals versus generation number graph for Case III is given in Figure 3.26.

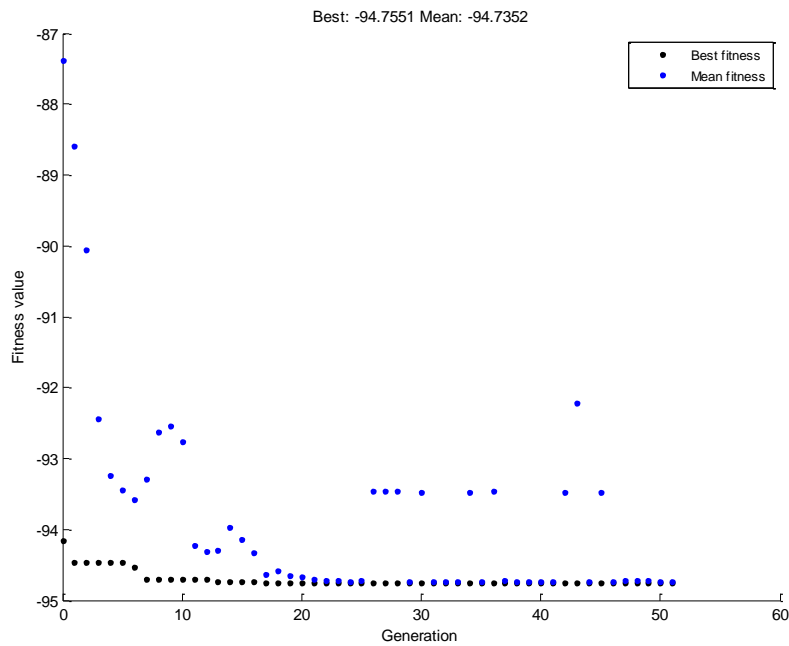


Figure 3.25. The Best and Mean Fitness Values vs Generation Graph for Case III

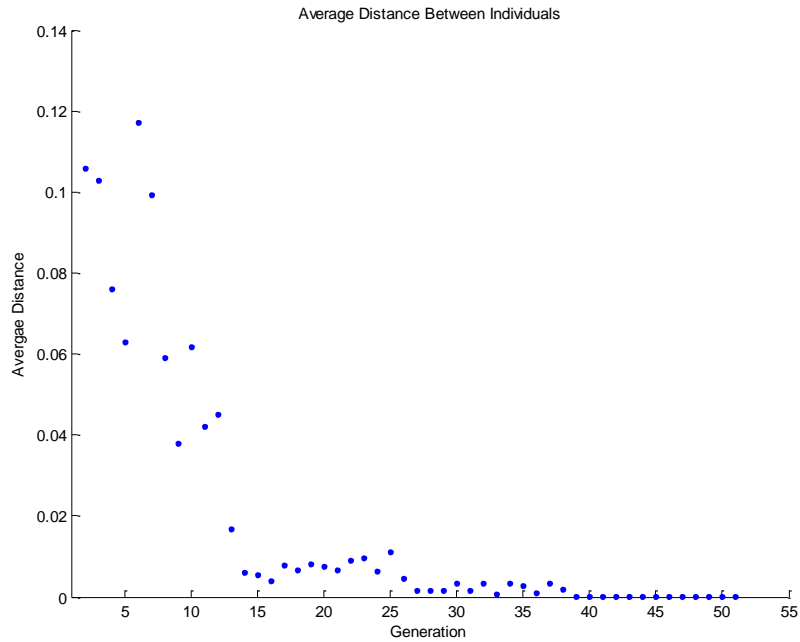


Figure 3.26. The Average Distance between Individuals vs Generation Number Graph for Case III

The results of objective function for Case III are presented in Table 3.14. The aerodynamic performance of the thinner baseline airfoil has improved by approximately 7.4% in this optimization. The  $C_l/C_d$  ratio comparison of the optimized airfoil geometry at Case III and the thinner baseline geometry is given in Figure 3.27. For all values of AoA till  $10^\circ$ , the  $C_l/C_d$  curve of optimized airfoil shows better performance than the thinner baseline geometry. After  $10^\circ$  AoA, the performance of optimized airfoil is decreasing gradually.

Table 3.14. The Objective Function Results for Case III

<b>Thinner Baseline <math>C_l/C_d</math> Optimization Results</b>	
Thinner Baseline	88,3
Lower Bound	81,4
Upper Bound	94,7
Optimization Results	94,8

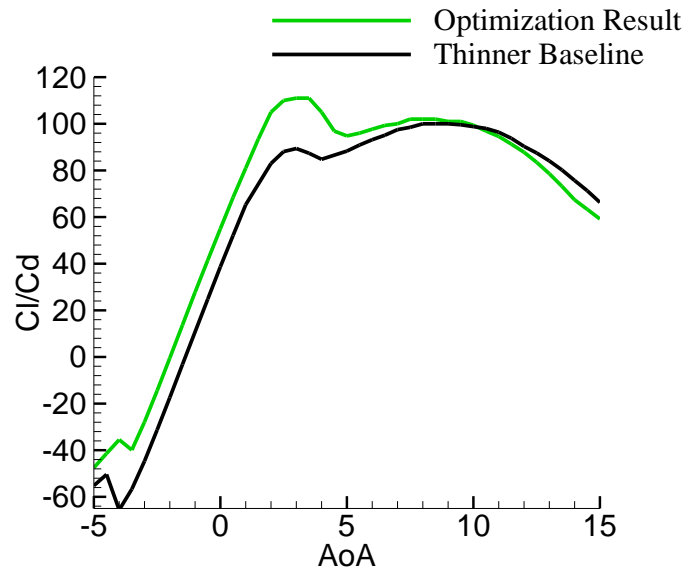


Figure 3.27. The  $C_l/C_d$  Ratio Comparisons for Case III

The optimized airfoil geometry, the thinner baseline geometry and S809 airfoil geometry is given comparatively in Figure 3.28. In PARSEC geometric coefficients for thinner optimized airfoil geometry are given.

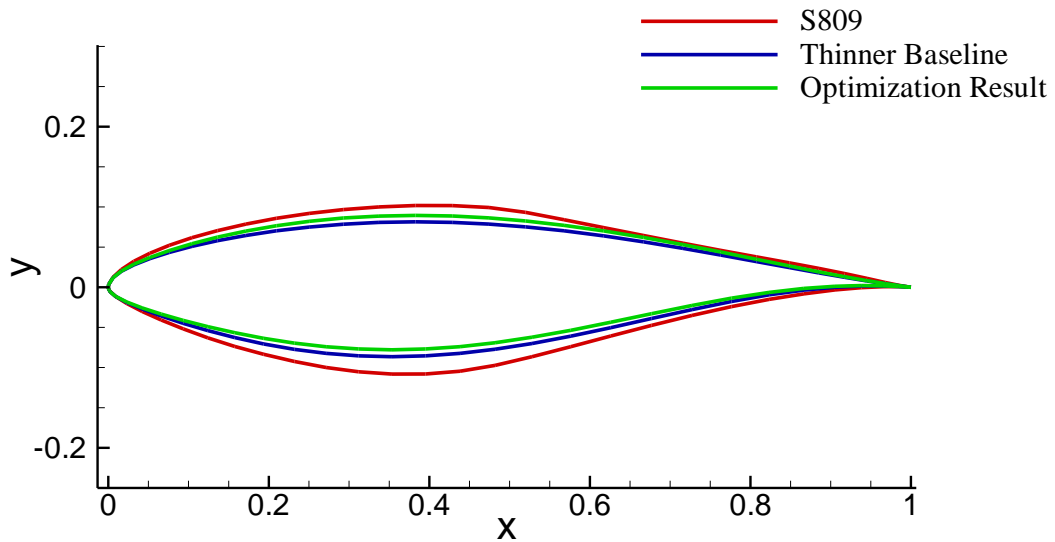


Figure 3.28. The Airfoil Geometry Comparisons for Case III

Table 3.15. PARSEC Geometric Coefficients for Thinner Optimized Baseline Airfoil

<b>Thinner Optimized</b>	<b>Y<sub>upper</sub></b>	<b>Y<sub>xx,upper</sub></b>	<b>Y<sub>lower</sub></b>	<b>Y<sub>xx,lower</sub></b>
Optimization Results	0,090	-0,792	-0,078	1,112

### 3.2.2.3. Case IV - Optimization of Thicker Baseline Airfoil with PARSEC

In Case IV - optimization of thicker baseline airfoil with PARSEC, the optimization flow conditions is set to fixed values as  $5^{\circ}$  AoA and  $1 \times 10^6 Re$ . Compressibility effects are not into taken into account. The genetic algorithm optimization parameters given in Table 3.7 are used also in this case. Best and mean fitness values versus generation number graph is provided in Figure 3.29. The average distance between individuals versus generation number graph for Case IV is given in Figure 3.30.

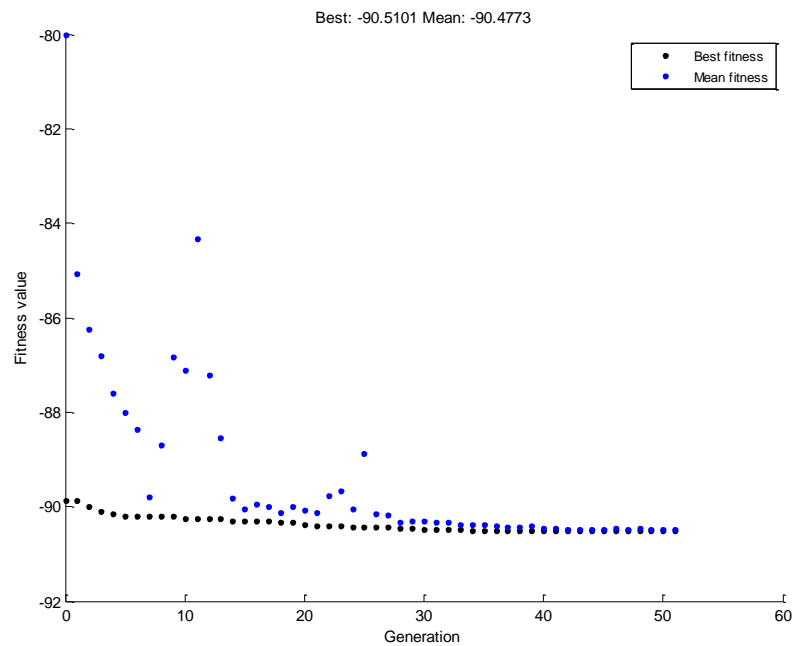


Figure 3.29. The Fitness Value vs Generation Number Graph for Case IV

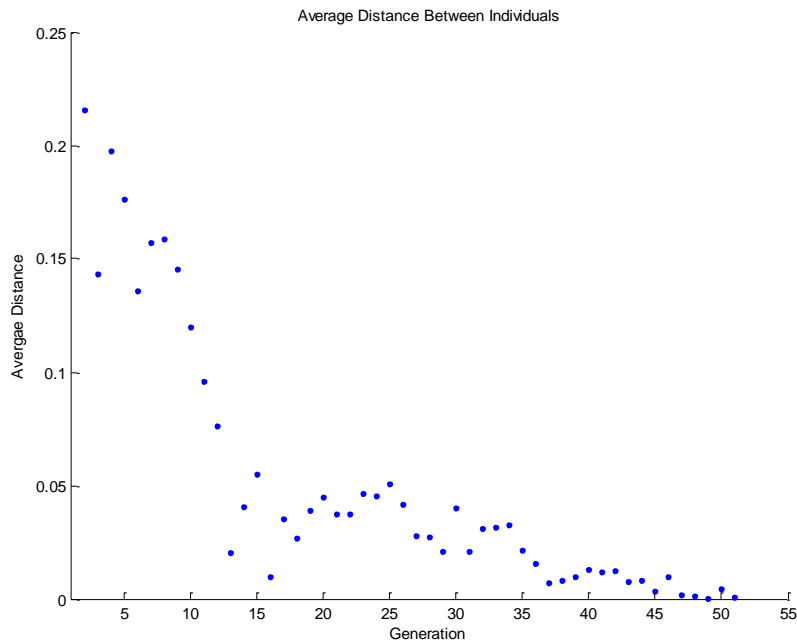


Figure 3.30. The Average Distance between Individuals vs Generation Number Graph for Case IV

The objective function values for Case IV are presented in Table 3.16. The aerodynamic performance of the thicker baseline airfoil has improved by approximately 10.3% in this optimization. The  $C_l/C_d$  ratio comparison of the optimized airfoil geometry at Case IV and the thicker baseline geometry is given in Figure 3.31. Till  $8^\circ$  of AoA,  $C_l/C_d$  curve of the optimized airfoil has higher performance than the thicker baseline airfoil. After that transition AoA value, the performance of optimized airfoil is decreased but two airfoils have nearly the same  $C_l/C_d$  curve.

Table 3.16. The Objective Function Results for Case IV

<b>Thicker Baseline <math>C_l/C_d</math> Optimization Results</b>	
S809 - Thicker Baseline	82,0
Lower Bound	70,7
Upper Bound	90,5
Optimization Results	90,5

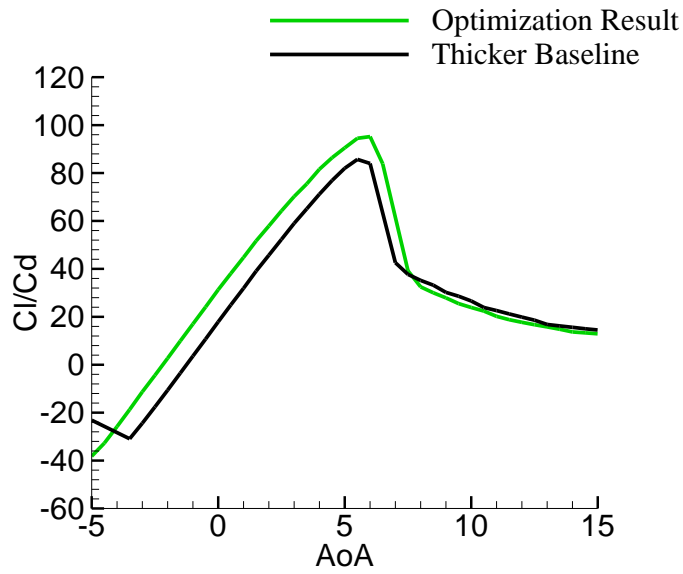


Figure 3.31. The  $C_l/C_d$  Ratio Comparisons for Case IV

The optimized airfoil geometry, the thicker baseline geometry and S809 airfoil geometry is given comparatively in Figure 3.32. In Table 3.17, PARSEC geometric coefficients for optimized airfoil geometry for tip section are given.

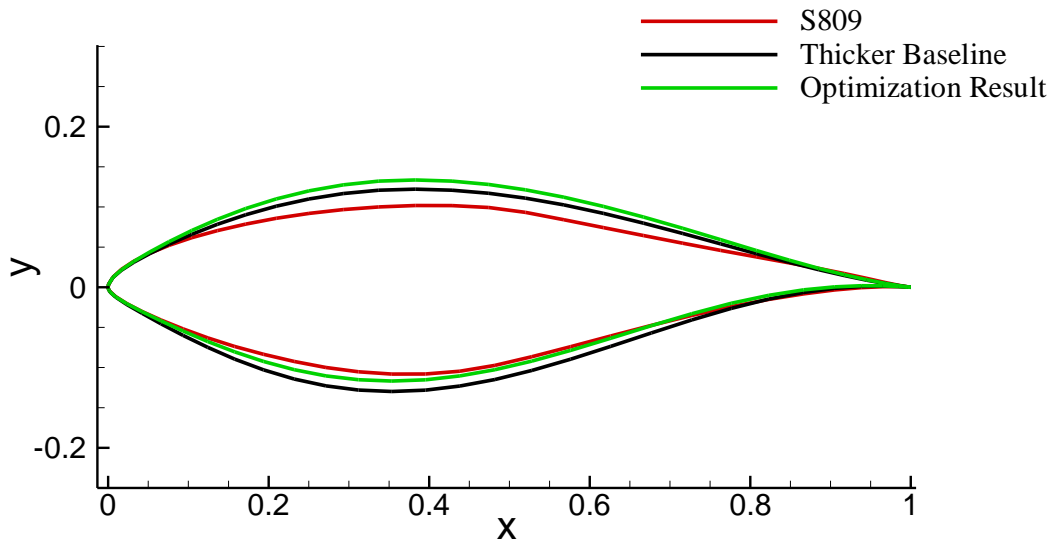


Figure 3.32. The Airfoil Geometry Comparisons for Case IV

Table 3.17. PARSEC Geometric Coefficients for Thicker Optimized Baseline Airfoil

<b>Thicker Optimized</b>	<b>y<sub>upper</sub></b>	<b>y<sub>xx,upper</sub></b>	<b>y<sub>lower</sub></b>	<b>y<sub>xx,lower</sub></b>
Optimization Results	0,13394	-1,43985	-0,11688	1,84316

### 3.3. Evaluations on Airfoil Optimization Results

In the previous sections of this chapter, several validation and optimization studies for airfoil geometry have been conducted for different cases. During these studies, it is experienced that both PARSEC and CST methods are favourable, robust and simple methods in airfoil geometry optimization studies. They allow sectional modifications to airfoil geometry in a controlled manner. They also have the ability to present airfoil geometry relatively low number of parameters. Consequently, the number of optimization variables is kept small leading to reduce optimization time efficiently. Moreover, these methods also show low sensitivity to parameter oscillations. On the other hand, these methods also have some limitations. For instance, CST method is inapplicable to cambered leading edge radius airfoils. In order to overcome this handicap, an additional term defining leading edge curvature is introduced to CST formulation. On the other hand, PARSEC method is not sufficient to represent trailing edge region in detail. A modification to this method called diverget tailing edge modification is provided to be able to define trailing edge much more elaborately [16].

It should be kept in mind that for both CST and PARSEC airfoil optimization cases, baseline airfoils and their corresponding bounds have designated by increasing and decreasing the related CST/PARSEC parameters. These kind of modifications done directly to parameters create different geometries in CST and PARSEC methods because they have different representation characterizations by definition. Therefore, for each case, baseline airfoils, their upper and lower bounds are different than each other meaning different design spaces and different solution sets.

The performance of optimized airfoils parameterized with CST method are compared the ones represented with PARSEC method in Table 3.18. Thinner baseline

optimization results have shown that CST parameterization method is able to form an airfoil geometry having higher performance approximately 2.1% than PARSEC method. On the other hand, PARSEC parameterization has improved the performance of CST representation by 1.9% in thicker baseline optimization studies.

Table 3.18. Aerodynamic Performance Comparison of CST vs PARSEC Parameterized Airfoils – Thinner Baseline Results (upper) and Thicker Baseline Results (lower)

<b>Thinner Baseline <math>C_l/C_d</math> Optimization Results</b>		
<b>Airfoil</b>	<b>CST Case I</b>	<b>PARSEC Case III</b>
Thinner Baseline	89,8	88,3
Lower Bound	91,5	81,4
Upper Bound	88,6	94,7
Optimization Results	96,8	94,8

<b>Thicker Baseline <math>C_l/C_d</math> Optimization Results</b>		
<b>Airfoil</b>	<b>CST Case II</b>	<b>PARSEC Case IV</b>
Thicker Baseline	80,6	82,0
Lower Bound	85,5	70,7
Upper Bound	75,4	90,5
Optimization Results	88,8	90,5

In this study, the performance enhancements are found comparatively close to each other according to CST and PARSEC representation optimization results. However, it should be noticed that CST representation method is superior to PARSEC method. First of all, CST parameterization method provides richer design space than PARSEC method. Since CST method allows to change the order of the fitting, it is much more flexible. Moreover, CST method also covers the most prominent property of PARSEC method which is the physically meaningful parameters. As discussed in section 3.1.1.2, leading edge radius, boattail angle, trailing edge thickness and airfoil thickness distribution are directly related the CST coefficients in a legitimate way.

This property makes possible specific purpose airfoil designs ensuring locally controlled design environments. Additionally, the performance of PARSEC representation method is highly susceptible to the quality of input airfoil coordinates. The PARSEC airfoil geometric parameters are calculated directly from a few regional coordinates. If the quality of input airfoil coordinates is inadequate, a relatively large error is induced on PARSEC geometric parameters promoting large residuals on fitting results.

To conclude, although both CST and PARSEC representation methods are powerful tools to design and optimize airfoil geometries, CST method is predominant to PARSEC method. As an outcome of this study, it is suggested to use CST method in design and optimization of airfoil geometries.

## CHAPTER 4

### BLADE DESIGN

#### 4.1. Airfoil Aerodynamic Coefficients Calculation

To be able to analyze the airfoil geometry effect on turbine performance, it is needed to know  $C_l$  and  $C_d$  values at corresponding flow conditions. It is needed to find aerodynamic data for different AoA and  $Re$  values. As previously mentioned, the panel solver, XFOIL is utilized for these calculations. However, after stall region XFOIL cannot provide this data. To be able to get aerodynamic data after stall at high AoA values,  $C_l$  and  $C_d$  values obtained from panel solver are extrapolated. For this purpose, a MATLAB code is written using Viterna-Corrigan Method [48]. Consequently, the airfoil 360° polar values are obtained. For validation purposes, S809 airfoil at  $0.75 \times 10^6 Re$ , the comparison between wind tunnel data, the results of an open source code “AirfoilPrep v2.02.03” [47] and the results of this study is given in Figure 4.1 and Figure 4.2.

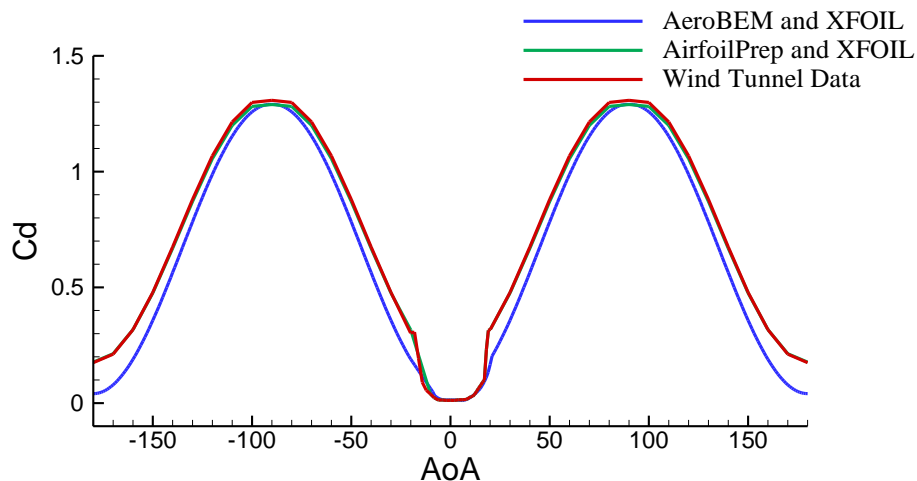


Figure 4.1.  $C_d$  vs AoA Graph for S809 Airfoil ( $Re=0.75 \times 10^6$ )

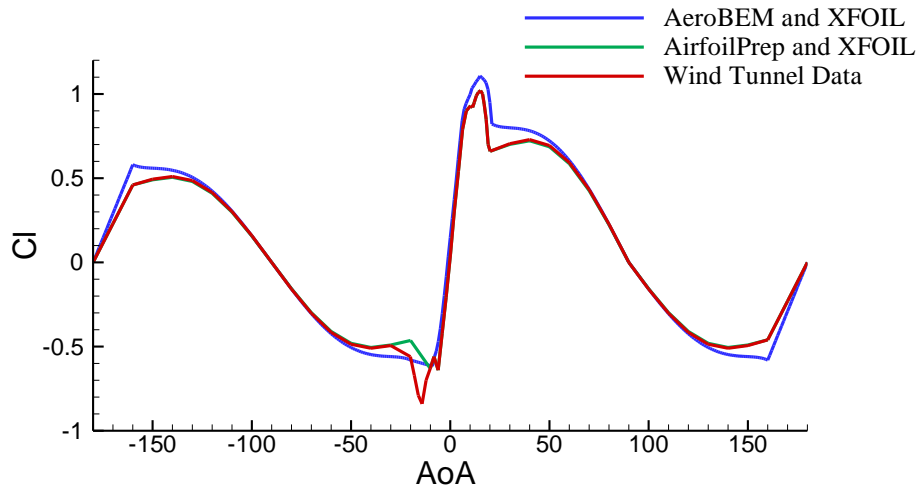


Figure 4.2.  $C_l$  vs AoA Graph for S809 Airfoil ( $Re=0.75 \times 10^6$ )

#### 4.2. BEM Analysis Validation

In this study, NREL Phase III and NREL Phase VI wind turbine rotors are selected as validation test cases. AeroBEM results are compared with the results of an open source BEM code “WT\_Perf” [53] developed by NREL and also experiment results [58]. The rotor geometric parameters of the reference turbines are given in Table 4.1.

Table 4.1. The Rotor Geometric Parameters of the NREL Phase III and VI Rotors

<b>Rotor Parameters</b>	<b>NREL Phase III</b>	<b>NREL Phase VI</b>
Blade Number	3	2
Rotor Radius	5.03 m	5.03 m
Rotational Speed	71.63 rpm	71.63 rpm
Cut-in Wind Speed	6 m/s	6 m/s
Rated Power	19.8 kW	19.8 kW
Hub Radius	0.723 m	1.275 m
Blade Pitch Angle	3°	0°
Twist Angle	Nonlinear: 44° (hub) — 0° (tip)	Nonlinear: 20° (hub) — -1.775° (tip)
Blade Chord Distribution	Constant	Linear
Hub Chord Length	0.4572 m	0.737 m
Tip Chord Length	0.4572 m	0.358 m
Airfoil Profile	S809	S809

The chord length distribution is given in Figure 4.3, and twist angle distribution is illustrated in Figure 4.4.

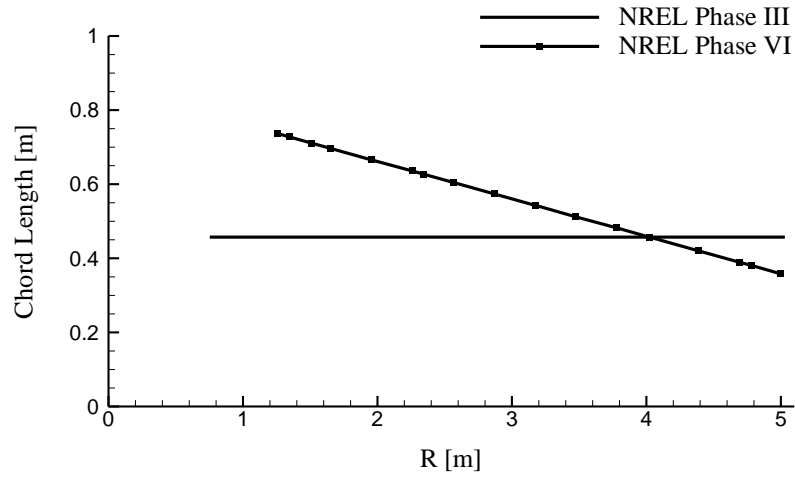


Figure 4.3. Chord Length Distribution of NREL Phase III and NREL Phase VI Turbines

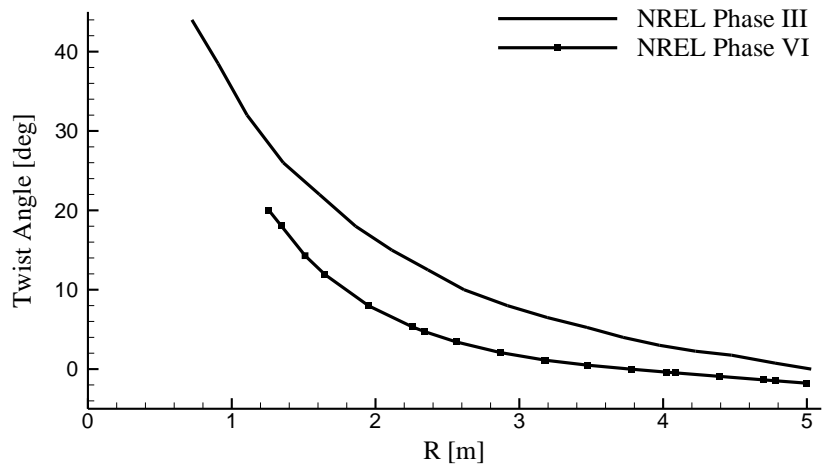


Figure 4.4. Twist Angle Distribution of NREL Phase III and NREL Phase VI Turbines

In order to avoid panel solver prediction, interpolation, extrapolation errors in  $C_l$  and  $C_d$  values, the wind tunnel measurements for S809 at 750.000  $Re$  is used to calculate power and thrust in validation studies.

#### 4.2.1. NREL Phase III Wind Turbine Validation

In this part, AeroBEM validations are done by using NREL Phase III wind turbine rotor. Power curve results are given in Figure 4.5 whereas thrust calculation results are given in Figure 4.6. It is notable that AeroBEM and WT\_Perf results are nearly the same for both power and thrust calculations. However, the experimental results seems quite different than BEM calculations. In NREL Phase III wind turbine experiments, the power measurements are taken from the output of the generator. Taking measurements from that location introduces mechanical and electrical loses to the experimental data. NREL reference test turbine is declared to have nearly 78% efficiency [58]. Since BEM calculates directly aerodynamic power without any system loss, this clarifies the discrepancy between BEM predictions and experimental data.

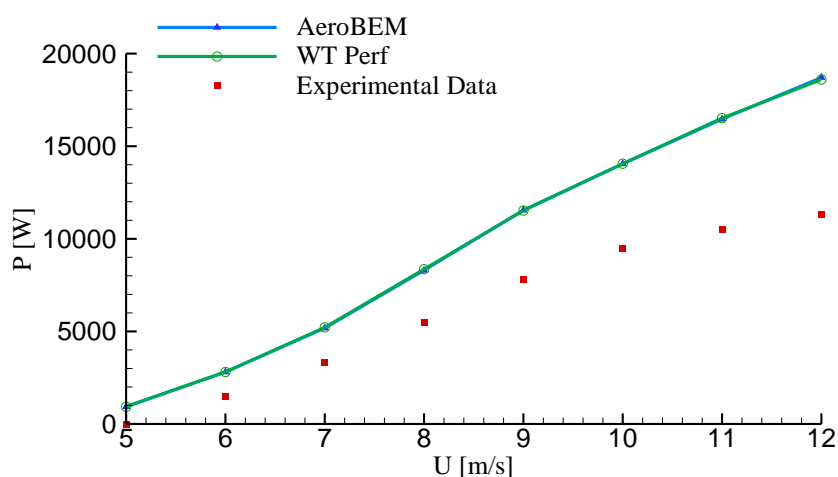


Figure 4.5. NREL Phase III Rotor Validation Case - Power Curve Results

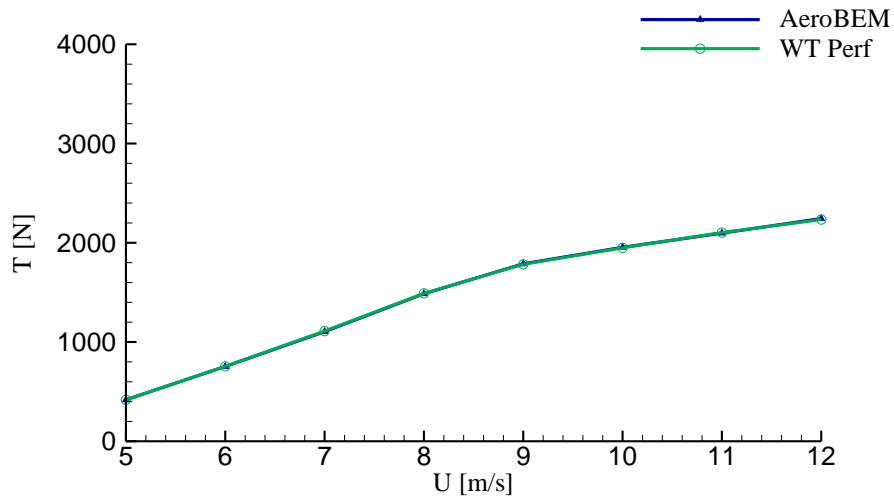


Figure 4.6. NREL Phase III Rotor Validation Case - Thrust Curve Results

For 5 m/s wind speed, AeroBEM results of some selected important parameters for NREL Phase VI rotor are given.  $F_{hub}$ ,  $F_{tip}$  and  $F$  vs dimensionless rotor radius graphs are illustrated in Figure 4.7, Figure 4.8 and Figure 4.9 respectively.

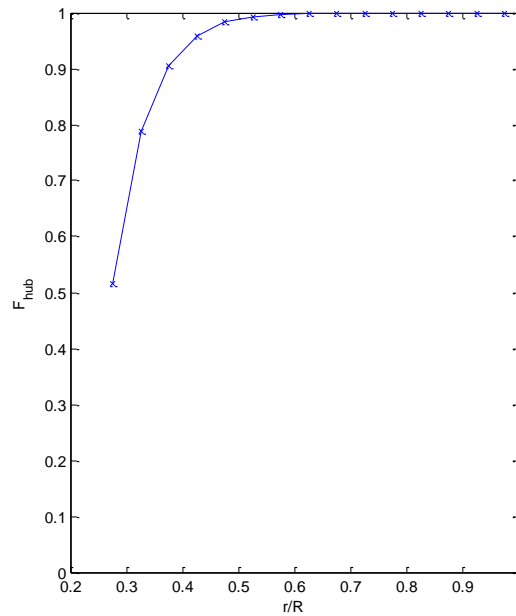


Figure 4.7.  $F_{hub}$  vs Dimensionless Rotor Radius Graph

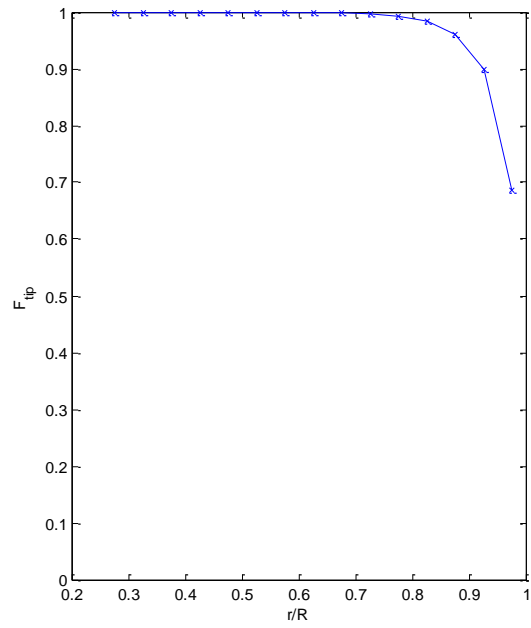


Figure 4.8.  $F_{tip}$  vs Dimensionless Rotor Radius Graph

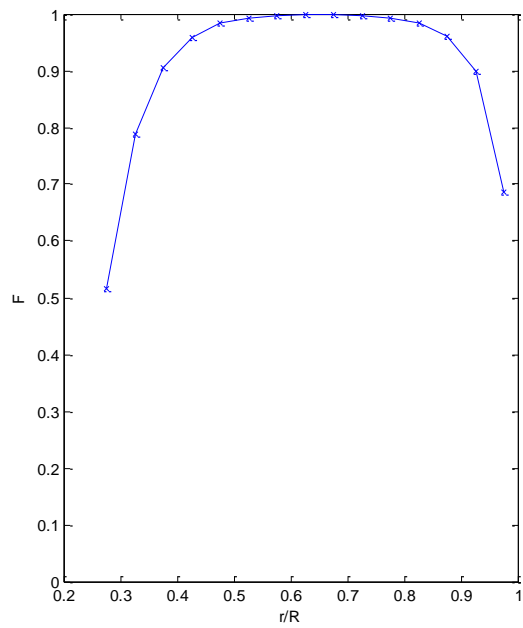


Figure 4.9.  $F$  vs Dimensionless Rotor Radius Graph

#### 4.2.2. NREL Phase VI Wind Turbine Validation

In this part, NREL Phase VI wind turbine performance is calculated and analyzed by using AeroBEM for validation purposes. Power curve results are given in Figure 4.10 whereas thrust calculation results are given in Figure 4.11. The predicted power curves by BEM codes begin with good agreement with experimental data at 5 m/s and 6 m/s wind speeds. Then BEM codes start to underestimate power at 7 m/s. At 8 m/s, rotor enters stall state, a serious breakdown in power curve is encountered and the power curve trend starts to descend abruptly. This unexpected result is directly related to the airfoil aerodynamic data. Remembering that only one aerodynamic dataset at 750.000  $Re$  is used in validation calculations. In actual condition,  $Re$  is increasing along the span and this change directly modifies the aerodynamic data of each blade element. That artificial effect coming from input aerodynamic dataset shows BEM power and thrust results poor. At the same time, it is observed that AeroBEM and WT\_Perf calculation results are highly similar once again. However, a small variation starting after 8 m/s wind speed is observed between BEM calculations. It is due to the usage of different interpolation methods to obtain aerodynamic data between two codes.

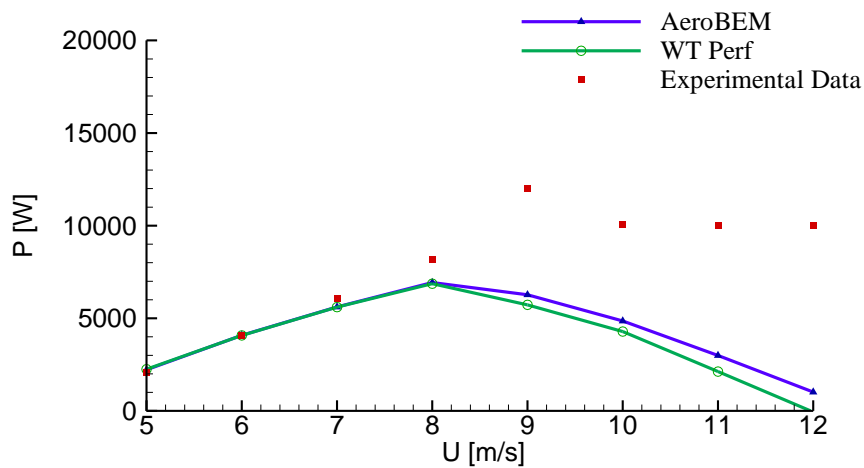


Figure 4.10. NREL Phase VI Rotor Validation Case - Power Curve Results

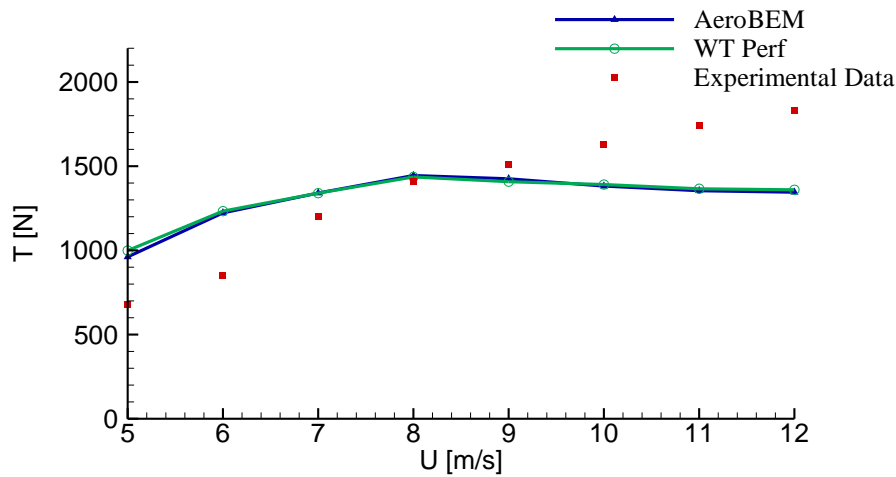


Figure 4.11. NREL Phase VI Rotor Validation Case - Thrust Curve Results

In this validation case, the influence of applied BEM modifications to thrust coefficient-axial induction factor curve is examined at different wind speeds. The results at 5 m/s and 12 m/s wind speeds are shown in Figure 4.12. For 5 m/s, the  $C_T$ - $\alpha$  curve without highly loaded rotor correction, the red one, is found very close to the uncorrected BEM predictions, the black one. Since 5 m/s is the cut-in wind speed, 3D effects are not very dominant and hub and tip losses are not too high. Also, the maximum  $C_T$  value is noted as nearly 1. When Buhl's empirical correlation is added after the transition  $\alpha$  value, i.e. 0.4, AeroBEM estimates increasing  $C_T$  behavior reaching the maximum as 2 for the highest axial induction factor value. For 12 m/s wind speed, the severity of the 3D effects is remarked by the suppression of the  $C_T$ - $\alpha$  curve. Besides, it is observed that Buhl correlation has tuned the  $C_T$ - $\alpha$  curve such a way that from transition to maximum values of  $\alpha$ , empirical correlation has a steeper inclination reaching the maximum  $C_T$  as 2 again. AeroBEM results are in a good agreement with the Figure 2.11 stated in [33].

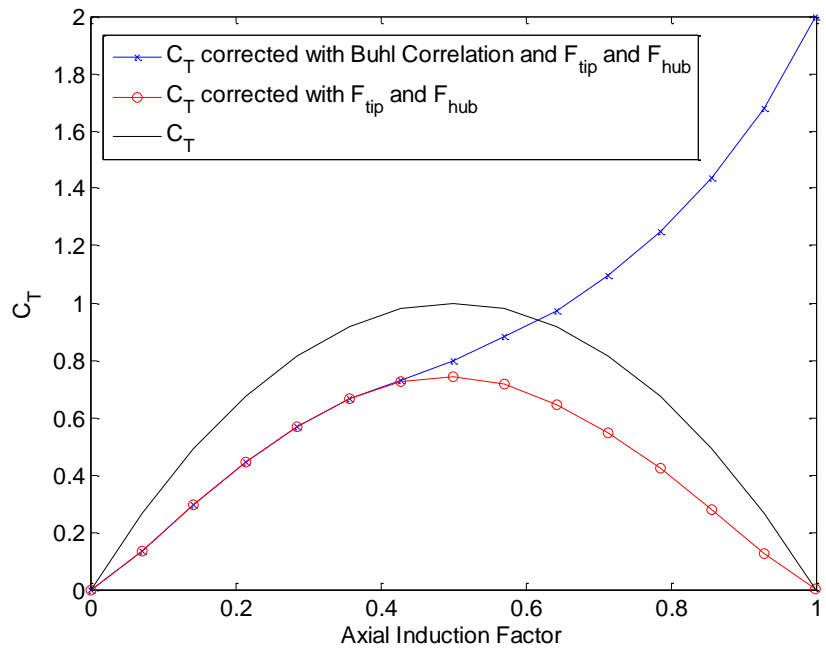
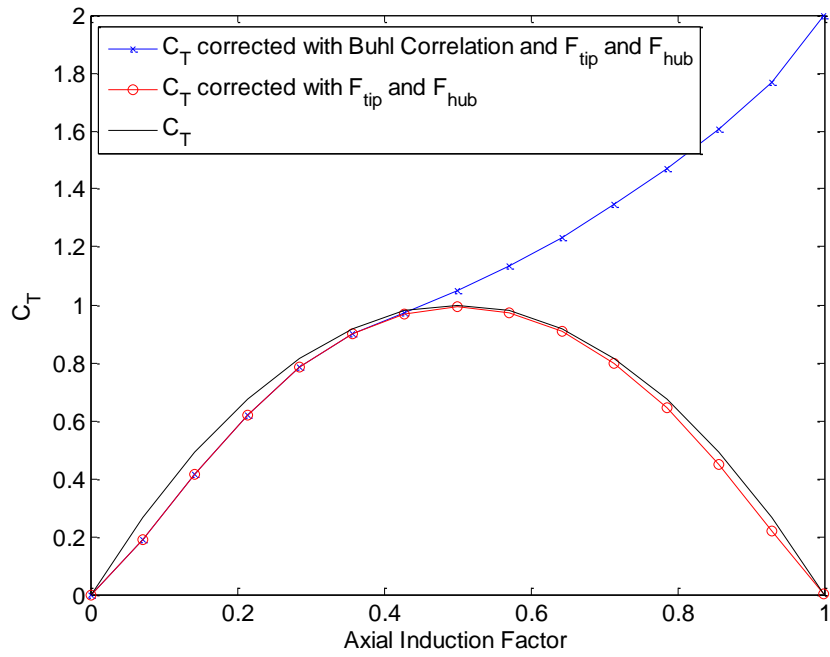


Figure 4.12.  $C_T$  vs Axial Induction Factor Curves at Different Wind Speeds –  
5 m/s (upper) and 12 m/s (lower)

### 4.3. Blade Optimization Studies

In this section, based on NREL Phase VI turbine rotor, a blade design study is performed by using optimized airfoils in Chapter 3.2 Airfoil Optimization Studies and investigating the correlation between rotor power performance and two decisive rotor geometric parameters, chord length and twist angle distribution.

At the first step, reference and optimized blade airfoil distributions are determined on the basis of NREL Phase VI turbine blade. Remembering that the NREL Phase VI turbine blade having constant airfoil distribution along the span, to be able to make more rational performance comparison, it is preferred to define the reference blade geometry having varying airfoil profile distribution. The NREL Phase VI turbine blade is divided into 4 sections. First section is root extension for both reference and optimized blades. The power production of this part is ignored for power calculations. The airfoil geometry distribution of reference blade for different sections is designated as the baseline airfoil geometries of Case I and Case II CST parameterized airfoil optimization studies and also S809. The reference blade airfoil geometry distribution is defined as;

- CST thicker baseline airfoil for blade root section (25-50% R)
- S809 for blade middle section (50-75% R)
- CST thinner baseline airfoil for blade tip section (75-100% R).

For optimized blade studies, the CST optimized airfoils in Case I and Case II are used investigating CST parameterized airfoil performance effects on blade power production characteristics. The airfoil geometry distribution is not modified during optimization. Similar to the reference blade, the optimized blade airfoil geometry distribution is defined as;

- CST optimized thick airfoil for blade root section (25-50% R)
- S809 for blade middle section (50-75% R)
- CST optimized thin airfoil for blade tip section (75-100% R).

Airfoil distributions of reference and optimized rotors are tabulated in Table 4.2 and the airfoil distribution of optimized rotor is illustrated in Figure 4.13.

Table 4.2. Airfoil Distribution of Reference and Optimized Rotors

Airfoil	0-25%R	25-50%R	50-75%R	75-100%R
<b>Reference Blade</b>	Root Extension	CST Thicker Baseline Airfoil	S809	CST Thinner Baseline Airfoil
<b>CST Optimized Blade</b>	Root Extension	CASE II Thicker Opt. Airfoil with CST	S809	CASE I Thinner Opt. Airfoil with CST

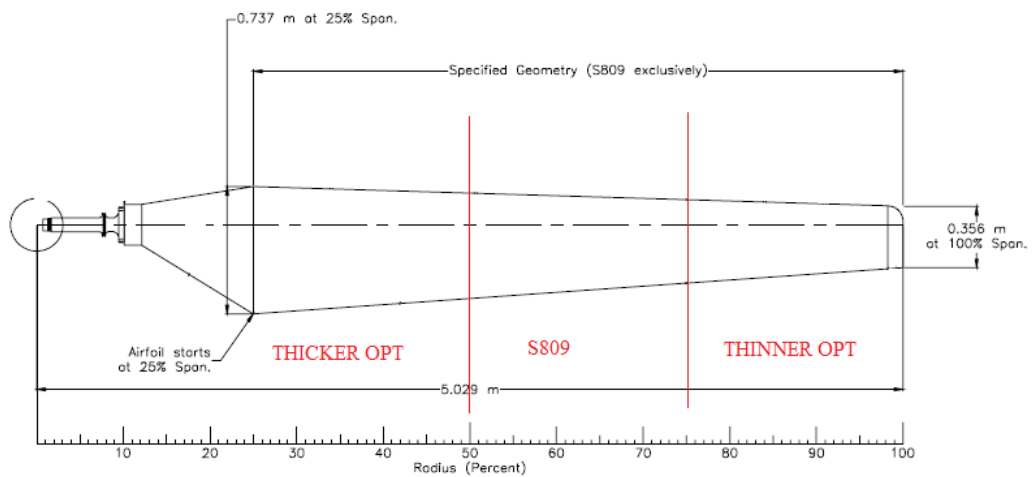


Figure 4.13. Airfoil Distribution Illustration for Optimized Rotor

After determining the airfoil distributions, the rotor geometric parameters are defined. The baseline chord length and twist angle distributions are obtained from NREL Phase VI rotor. Their bounds are provided in Table 4.3. Design wind speed is selected as 12 m/s. Blade is divided into 21 blade elements leading total number of optimization variables as 42. The optimization objective is introduced as the maximum power production for a given wind speed. The genetic algorithm optimization parameters for blade optimization are summarized in Table 4.4.

Table 4.3. Chord Length and Twist Angle Optimization Bounds

<b>Reference Rotor - NREL Phase VI</b>	<b>Chord Length</b>	<b>Twist Angle</b>
<b>Upper Bound</b>	+10% by value	+2 <sup>0</sup>
<b>Lower Bound</b>	-10% by value	-2 <sup>0</sup>

Table 4.4. The Genetic Algorithm Optimization Parameters for Blade Optimization

<b>Optimization Variables</b>	
Population Size	50
Minimum Number of Generations	51
Function Tolerance	1e+1

Best and mean fitness values versus generation number graph is provided in Figure 4.14. The power curve comparison for airfoil, chord and twist optimized rotor and reference rotor is presented in Figure 4.15 and power data is tabulated in Table 4.5. It is seen that until the 10 m/s wind speed, there is no spectacular increase in power production of optimized rotor. However, the power increase approaches to 11% at 11 m/s wind speed. When the wind velocity attains to 12 m/s, the power increase achieves to 18.8%.

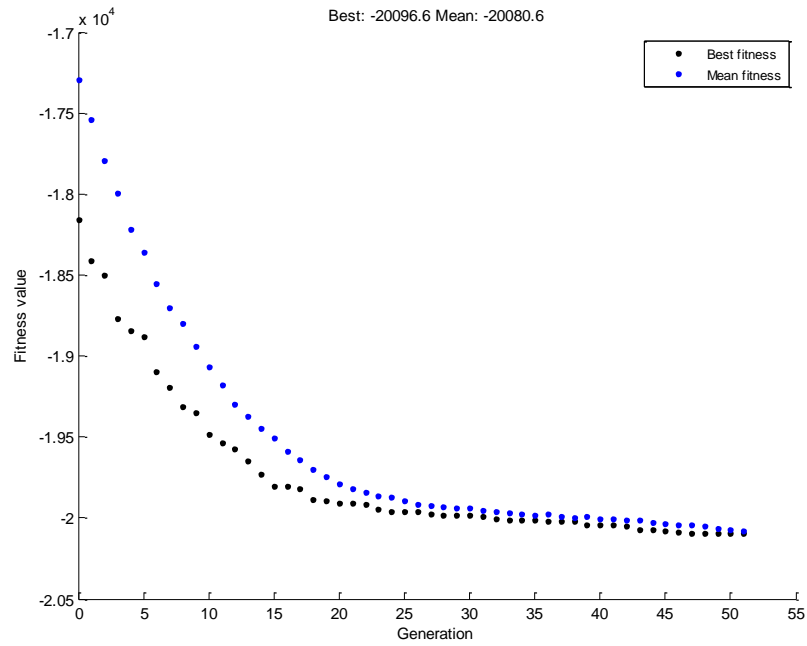


Figure 4.14. The Best and Mean Fitness Values vs Generation Graph for Blade Optimization Study

Table 4.5. Power Comparison for Airfoil, Chord and Twist Optimized Rotor

<b>U</b> <b>[m/s]</b>	<b>P<sub>opt</sub></b> <b>[W]</b>	<b>P<sub>ref</sub></b> <b>[W]</b>	<b>Increase</b> <b>[%]</b>
5	2516	2442	3,0
6	4310	4278	0,7
7	6544	6498	0,7
8	9087	8922	1,9
9	11871	11520	3,0
10	14834	14215	4,4
11	17836	16076	11,0
12	20097	16911	18,8

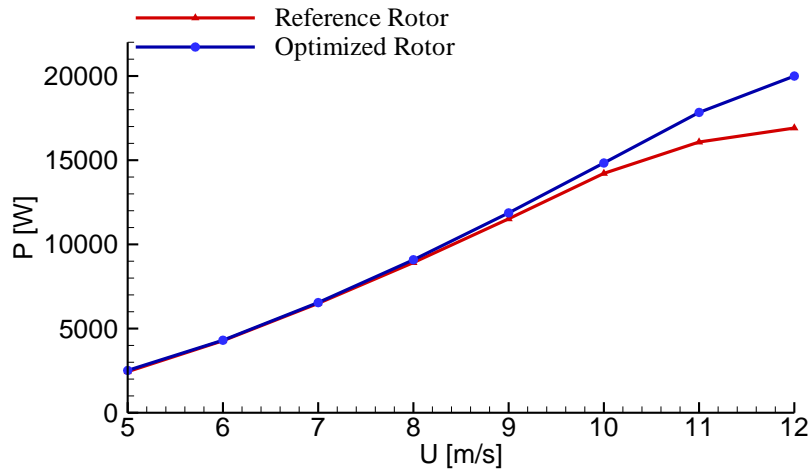


Figure 4.15. Power Curve Comparison for Airfoil, Chord and Twist Optimized Rotor

The optimized chord length and twist angle graphs are given in Figure 4.16 and Figure 4.17 respectively. It is observed that blade planform area is increased from 2.1 m<sup>2</sup> to 2.2 m<sup>2</sup>. For further optimization case studies, blade planform area can be bounded as in Ceyhan's study [1] or kept constant as well.

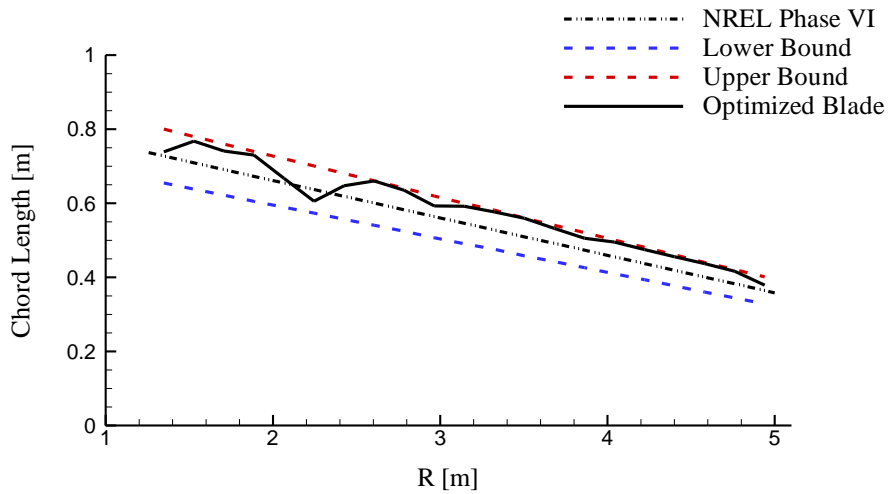


Figure 4.16. Chord Distribution of Airfoil, Chord and Twist Optimized Rotor

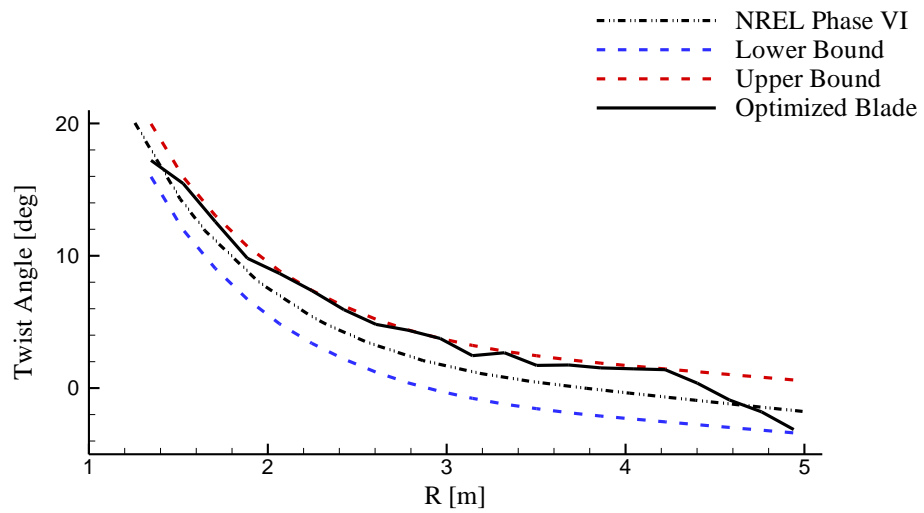


Figure 4.17. Twist Distribution of Airfoil, Chord and Twist Optimized Rotor

To sum up, in this chapter, blade geometry optimizations concerning airfoil profile, chord length and twist angle distributions are performed. Based on NREL Phase VI reference rotor, new blades are designed. The final optimized rotor blade has superior aerodynamic performance to reference blade and it can produce 18.8% more power than reference turbine at 12 m/s wind speed.



## CHAPTER 5

### CONCLUSION

#### 5.1. Concluding Remarks

In this master thesis study, optimization of HAWT's rotor airfoil geometries and blades are performed by using two airfoil geometry parameterization methods CST and PARSEC with GA. For power performance calculations BEM method is used and airfoil aerodynamic data is obtained from XFOIL.

In airfoil optimization studies, firstly, the validation studies for AirfoilCST and AirfoilPARSEC are done for different airfoils, RAE 2822 and S809 with different order of transformations. When these codes are verified, optimization studies for different sections of blade are investigated. For two selected baseline airfoil profiles, called thinner and thicker baselines, airfoil optimizations with CST and PARSEC representation methods are performed subject to maximization of  $C_l/C_d$  ratio objective. It is observed that the aerodynamic performance of new airfoil geometries parameterized by using CST method is improved 7.7% for thinner optimization case whereas 10.2% for thicker optimization case. Similarly, it is seen that the aerodynamic performance of new airfoil geometries parameterized by using PARSEC method is improved 7.4% for thinner optimization case and 10.3% for thicker optimization case.

In blade design and optimization studies, firstly the validations for AeroBEM is performed for NREL Phase III and NREL Phase VI reference wind turbines. After that, for maximum power production objective, by using the optimized airfoils with CST methods, new blades having different airfoil, chord length and twist angle distributions are designed based on NREL Phase VI turbine blade. In this case, the power production of reference turbine is improved 3% at 5 m/s and 18.8% at 12 m/s wind speed.

In conclusion, it can be stated that CST parameterization method is more powerful than PARSEC method to optimize airfoil profiles. Power performance predictions of wind turbine rotor can be performed by using BEM theory in a trustworthy manner.

## 5.2. Future Work

The future works and recommendations can be summarized as;

- An integrated design tool can be developed to optimize both airfoil and blade parameters simultaneously.
- In order to get aerodynamic data instead of using panel method solver, XFOIL, the code could be coupled with a CFD code.
- Airfoil aerodynamic coefficients can be corrected by using dynamic stall correlations.
- The AeroBEM code can be corrected for rotor yaw angle to account for the skewed wake effect.
- The optimization variables can be expanded for rotor geometric variables such as rotor radius, rotational speed, blade set pitch angle, etc.
- The optimization variables can be diversified for blade planform variables such as thickness to chord ratio distribution, etc.
- The code can be paralleled to be able to solve different optimization parameters all together faster.
- Airfoil optimization objective function can be modified to design specific purpose airfoils, such as blunt trailing edge airfoil families, leading edge roughness resistant airfoil families, etc.
- CST method can be hybridized with other airfoil representation techniques such as Bezier curves, B-Splines, etc. based on design demands.
- Blade optimization problem can be described by using directly a 3D CST parameterization formulation.
- Blade optimization objective function can be modified to optimize blades not only aerodynamically but also structurally efficient.

- The performance of different optimization techniques such as particle swarm algorithms can be investigated.
- Wind tunnel tests of optimized airfoils and blades can be performed and compared the results of this study.



## REFERENCES

- [1] Ceyhan, O., "Aerodynamic Design and Optimization of Horizontal Axis Wind Turbines by Using BEM Theory and Genetic Algorithm," MS Thesis, METU Dept. of Aerospace Engineering, September 2008.
- [2] Ceyhan, O., Ortakaya, Y., Korkem, B., Sezer-Uzol, N. and Tuncer, I.H., "Optimization of Horizontal Axis Wind Turbines by using BEM Theory and Genetic Algorithm," 5th Ankara International Aerospace Conference, METU Ankara, Turkey, 17-19 August 2009.
- [3] Sağol, E., Sezer-Uzol, N., and Uzol, O., "Site Specific Cost-Effective Design Optimization of A Horizontal Axis Wind Turbine," NUYEK 2009, Nuclear & Renewable Energy Sources with International Participation, Ankara, 28-29 September 2009.
- [4] Sağol, E., "Site Specific Design Optimization of A Horizontal Axis Wind Turbine Based On Minimum Cost of Energy," MS Thesis, METU Dept. of Aerospace Engineering, January 2010.
- [5] Polat, O., Sezer-Uzol, N., and Tuncer, I.H., "Aerodynamic Optimization Of Horizontal Axis Wind Turbines Based On Potential Flow Solutions With BEM Theory And Genetic Algorithm," ECCOMAS CFD & OPTIMIZATION 2011 - 064, An ECCOMAS Thematic Conference, Antalya, Turkey, 23-25 May 2011.
- [6] Polat, O., "Genetic Algorithm Based Aerodynamic Shape Optimization of Wind Turbine Rotor Blades Using A 2-D Panel Method with a Boundary Layer Solver," MS Thesis, METU Dept. of Aerospace Engineering, December 2011.
- [7] Polat, O., Sezer-Uzol, N., and Tuncer, I.H., "Aerodynamic Shape Optimization of Wind Turbine Blades Using A 2-D Panel Method With A Boundary Layer Solver And A Genetic Algorithm," European Congress on Computational Methods in Applied Sciences and Engineering (ECCOMAS 2012), Vienna, Austria, September 10-14, 2012.
- [8] Polat, O., Sezer-Uzol, N., and Tuncer, I.H., "Aerodynamic Shape Optimization of Wind Turbine Blades Using a Parallel Genetic Algorithm," AIAC-2013-154, 7. Ankara International Aerospace Conference, METU, Ankara, Turkey, 11-13 September 2013.
- [9] Polat, O., Sezer-Uzol, N., and Tuncer, I.H., "Genetic Algorithm Based Aerodynamic Shape Optimization Tool for Wind Turbine Blades and its Implementation to Helicopters," AHS 70th Forum and Technology Display, Montreal, Canada, May 19-22, 2014.

- [10] Elfarra, M.A., Sezer-Uzol, N., and Akmandor, I.S., "Investigations on Tangential Tip Tilting for HAWT Rotor Blades," 10th International Conference on Clean Energy, ICCE-2010, Famagusta, North Cyprus, 15-17 September 2010.
- [11] Elfarra, M.A., Akmandor, I.S., and Sezer-Uzol, N., "Pitch Angle Design of NREL VI Wind Turbine Blade," ECCOMAS CFD & OPTIMIZATION 2011-1080, An ECCOMAS Thematic Conference, Antalya, Turkey, 23-25 May 2011.
- [12] Elfarra, M.A., Akmandor, I.S., and Sezer-Uzol, N., "Investigation and Optimization of Winglets for HAWT Rotor Blades," ETC 2011, 9th European Conference on TURBOMACHINERY Fluid Dynamics and Thermodynamics, Istanbul, Turkey, 21-25 March 2011.
- [13] Elfarra, M., "Horizontal Axis Wind Turbine Rotor Blade: Winglet and Twist Aerodynamic Design and Optimization Using CFD," PhD Thesis, METU Dept. of Aerospace Engineering, January 2011.
- [14] Elfarra, M.A., Sezer-Uzol, N., and Akmandor, I.S., "NREL VI Rotor Blade: Numerical Investigation and Winglet Design and Optimization Using CFD," Wind Energy, (Online Early View, 6 February 2013) Vol 17. Issue 4. pp 605-626, April 2014.
- [15] Elfarra, M.A., Sezer-Uzol, N., and Akmandor, I.S., "Investigations on Blade Tip Tilting for HAWT Rotor Blades Using CFD," International Journal of Green Energy, (Published Online: 08 Oct 2014) Vol. 12, Issue 2, pp. 125-138, 2015.
- [16] Sobieczky, H., "Aerodynamic Design and Optimization Tools Accelerated by Parametric Geometry Preprocessing," European Congress on Computational Methods in Applied Sciences and Engineering ECCOMAS 2000, Barcelona, 11-14 September 2000.
- [17] Kulfan B.M., "Universal Parametric Geometry Representation Method," 45. Journal of Aircraft, Vol. 45, No.1, January-February 2008.
- [18] Kulfan B.M. and J.E. Bussoletti., "'Fundamental" Parametric Geometry Representations for Aircraft Component Shapes," 11th AIAA/ISSMO Multidisciplinary Analysis and Optimization Conference: The Modeling and Simulation Frontier for Multidisciplinary Design Optimization, Virginia, USA, 6 - 8 September 2006.
- [19] Javed F., Javed S., Bilal T., Rastogi V., "Design of Multiple Airfoil HAWT Blade using MATLAB Programming," 5th International Conference on Renewable Energy Research and Applications - ICRERA 2016, November 2016.
- [20] Barret R.T., "Investigation into Integrated Free-Form and Precomputational Approaches for Aerostructural Optimization of Wind Turbine Blades", MS Thesis, Brigham Young University Dept. of Mechanical Engineering, January 2018.

- [21] Liang C, Li H., “Aerofoil Optimization for Improving The Power Performance of a Vertical Axis Wind Turbine Using Multiple Streamtube Model and Genetic Algorithm,” *R Soc Open Sci.* 2018;5(7):180540. Published 2018 Jul 25. doi:10.1098/rsos.180540
- [22] Ning, S.A., “A Simple Solution Method For The Blade Element Momentum Equations With Guaranteed Convergence,” *Wind Energy* 17(9), July 2013. DOI:10.1002/we.1636.
- [23] Engfer, C., Canal, M., and Nualart, P. “Optimization Methods Applied to Wind Turbine Blade Design”. Brazil Windpower 2015 Conference and Exhibition, Brazil. September 2015.
- [24] Eke, B.G., and Onyewudiala I., J., “Optimization of Wind Turbine Blades Using Genetic Algorithm”. *Global Journal of Researches in Engineering.* Vol 10. Issue 7 (ver 1.0), page 22 . December 2010.
- [25] Méndez, J., and Greiner, D. “Wind blade chord and twist angle optimization using genetic algorithms”. *Proceedings of the Fifth International Conference on Engineering Computational Technology*, B. Topping, G. Montero, and R. Montenegro, eds., Civil-Comp Press, Las Palmas de Gran Canaria, Spain, Volume 6, pages 12-15. September 2006.
- [26] Declaration of Responsibilities and Human Duties - Valencia Declaration, 1998, last visited 31.07.2019 <http://globalization.icaap.org/content/v2.2/declare.html>
- [27] Kyoto Protocol to the United Nations Framework Convention on Climate Change, 1998. last visited 31.07.2019 <https://unfccc.int/resource/docs/convkp/kpeng.pdf>
- [28] Paris Agreement, 2015, last visited 31.07.2019 [https://unfccc.int/sites/default/files/english\\_paris\\_agreement.pdf](https://unfccc.int/sites/default/files/english_paris_agreement.pdf)
- [29] Hansen, M.O.L. “Aerodynamics of Wind Turbines”, Routledge, 2015.
- [30] Sørensen, J.N. “General Momentum Theory for Horizontal Axis Wind Turbines”, Springer, 2016.
- [31] Branlard, E. “Wind turbine tip-loss corrections - Review, implementation and investigation of new models”, MS Thesis, DTU Risø National Laboratory, September 2013.
- [32] Burton, T., Jenkins, N., Sharpe, D. and Bossanyi, E. “Wind Energy Handbook”, John Wiley & Sons, ISBN: 978-0-470-69975-1, 2011.
- [33] Moriarty, P.J. and Hansen, A.C. “AeroDyn Theory Manual”. National Renewable Energy Laboratory Golden, Colorado, USA, 2005.
- [34] Drela, M. “XFOIL: An Analysis and Design System for Low Reynolds Number Airfoils”, MIT, Dept. of Aeronautics and Astronautics, Cambridge, 1989.

- [35] Venkataraman, V. “Applied Optimization with MATLAB Programming”, John Wiley & Sons, 2002.
- [36] Gen, M., Cheng, R. “Genetic Algorithms and Engineering Optimization”, John Wiley & Sons, 2000.
- [37] Van Kuik, G. A. M., Peinke, J., Nijssen, R., Lekou, R., Mann, J., Sørensen, J. N., Ferreira, C., vanWingerden, J. W., Schlipf, D., Gebraad, P., Polinder, H., Abrahamsen, A., van Bussel, G. J. W., Sørensen, J. D., Tavner, P., Bottasso, C. L., Muskulus, M., Matha, D., Lindeboom, H. J., Degraer, S., Kramer, O., Lehnhoff, S., Sonnenschein, M., Sørensen, P. E., Künneke, R. W., Morthorst, P. E. and Skytte, K. “Long-Term Research Challenges in Wind Energy – a Research Agenda by the European Academy of Wind Energy”, *Wind Energ. Sci.*, 1, 1–39, 2016, doi:10.5194/wes-1-1-2016, published on 9 February 2016.
- [38] Dykes, K., Veers, P., Lantz, E., Holttinen, H., Carlson, O., Tuohy, A., Sempreviva, A. M., Clifton, A., Rodrigo, J.S., Berry, D., Laird, D., Carron, S., Moriarty, P., Marquis, M., Meneveau, C., Peinke, J., Paquette, J., Johnson, N., Pao, L., Fleming, P., Bottasso, C., Lehtomaki, V., Robertson, A., Muskulus, M., Manwell, J., Tande, J. O., Sethuraman, L., Roberts, O., Fields, J. “Results of IEA Wind TCP Workshop on a Grand Vision for Wind Energy Technology”, IEA Wind TCP Task 11 Technical Report, published on April 2019.
- [39] GWEC - Global Wind Report 2018, published on April 2019.
- [40] BloombergNEF H2 2018 LCOE Update – Wind Report
- [41] TWEA, “Turkish Wind Energy Statistics Report”, published on January 2019.
- [42] Okrent, J., “An Integrated Method for Airfoil Optimization”, MS Thesis, Lehigh University Dept. of Mechanical Engineering, May 2017.
- [43] Mauclere, X., “Automatic 2D Airfoil Generation, Evaluation and Optimisation using MATLAB and XFOIL”, MS Thesis, Technical University of Denmark Dept. of Mechanical Engineering, August 2009.
- [44] Grasso, F., “Hybrid Optimization for Wind Turbine Thick Airfoils”, AIAA 2012-1354, Presented at the 8th AIAA Multidisciplinary Design Optimization Specialist Conference, 23 - 26 April 2012.
- [45] Bortolotti, P., Tarres, H. C., Dykes, K., Merz, K., Sethuraman, L., Verelst, D., Zahle, F., “IEA Wind Task 37 on Systems Engineering in Wind Energy WP2.1 Reference Wind Turbines”, May 2019.
- [46] Gudmundsson, S., “General Aviation Aircraft Design Applied Methods and Procedures”, Butterworth-Heinemann, ISBN: 978-0-12-397308-5, 2014.

- [47] Hansen C., “NWTC Design Codes AirfoilPrep v2.02.03”, <https://nwtc.nrel.gov/AirFoilPrep> last modified 19 December 2014; accessed August 2019.
- [48] Viterna, L.A., Corrigan R.D., “Fixed Pitch Rotor Performance of Large Horizontal Axis Wind Turbines”, Proceedings from the Workshop on Large Horizontal Axis Wind Turbines, NASA CP-2230, DOE Publication CONF-810752, Cleveland, OH, NASA Lewis Research Centre, 1981.
- [49] Van Bussel, G., “Wakes, Blades and Airfoils an Entangles Triology” Torque from Wind 2012, presented on 10 October 2012.
- [50] Jonkman, J. M., Butterfield, S., Musial, W., Scott., G., “Definition of a 5-MW Reference Wind Turbine For Offshore System Development” National Renewable Energy Laboratory Golden, CO, 2009. Airfoil coordinates retrieved from [https://github.com/old-NWTC/FAST/tree/master/CertTest/5MW\\_Baseline/Airfoils](https://github.com/old-NWTC/FAST/tree/master/CertTest/5MW_Baseline/Airfoils), accessed August 2019.
- [51] Sant, T., “Improving BEM-based Aerodynamic Models in Wind Turbine Design Codes”, PhD Thesis, University of Malta Dept. of Mechanical Engineering, January 2007.
- [52] Buhl, M. L., “A New Empirical Relationship between Thrust Coefficient and Induction Factor for The Turbulent Windmill State.” Technical Report NREL/TP-500-36834, NREL, August 2005.
- [53] Buhl, M. L., “NWTC Design Codes - WT\_Perf”, version v3.05.00a-adp, last modified 8 November 2012.
- [54] Vecchiaa, P.D., Daniele, E., D’Amato, E., “An Airfoil Shape Optimization Technique Coupling PARSEC Parameterization and Evolutionary Algorithm”, Elsevier Aerospace Science and Technology, Volume 32, Issue 1, January 2014, Pages 103-110.
- [55] Liu, X., He, W., “Airfoil Optimization Design Based on the Pivot Element Weighting Iterative Method” MDPI Journal, Algorithms, 2018, 11, 163; DOI:10.3390/a11100163, Accepted on 16 October 2018; Published on 22 October 2018.
- [56] Masters, D. A., Taylor, N. J., Rendall, T. C. S., Allen, C. B., Poole, D. J., “Review of Aerofoil Parameterisation Methods for Aerodynamic Shape Optimisation”, AIAA paper 2015-0761, DOI: 10.2514/6.2015-0761, 2015.
- [57] Somers, D. M., “Design and Experimental Results for the S809Airfoil”, NREL/SR-440-6918, UC Category: 1213, DE97000206, January 1997.
- [58] Schepers, J. G., Brand, A. J., Bruining, A., Graham, J. M. R., Hand, M. M., Infield, D. G., Madsen, H. A., Maeda, T., Paynter, J. H., van Rooij, R., Shimizu, Y.,

Simms, D.A., Stefanatos, N., “Final report of IEA AnnexXVIII: Enhanced Field Rotor Aerodynamics Database”, Technical Report, ECN-C--02-016, 2002.

[59] Şahin, M., “Dynamic Modelling, Control and Adaptive Envelope Protection System for Horizontal Axis Wind Turbines”, PhD Thesis, METU Dept. of Aerospace Engineering, December 2018.